UNIVERSIDADE
BEIRA INTERIOR

Design of a Solar UAV for Persistent Wildlife Monitoring

(Versão final após defesa)

Rúben David Almeida Santos

Dissertação para obtenção do Grau de Mestre em

Engenharia Aeronáutica

(Mestrado integrado)

Orientador: Prof. Doutor Pedro Vieira Gamboa

Design of a solar UAV for persistent wildlife monitoring

Novembro de 2021

Acknowledgments

First, I would like to thank to everyone who supported me throughout the years of the course and during the thesis.

Starting with professor Pedro Gamboa for the guidance, patience and knowledge that has been transmitted over the years.

To my parents, sister, and other family members, for the support they gave me throughout the course.

To my friends and colleagues Pedro Neto, Mariana Ribeiro, Bárbara Penouço e Francisco Castello Branco for being part of the development of the methodology presented in this thesis that started as a group project for Aircraft Design class at Universidade da Beira Interior for the Aeronautic Engineering course; and for their support over the years.

Finally, thanks to Jorge Rodrigues, Kateryna Shvydyuk and other non-mentioned friends for the support and patience.

Resumo

Desde o início da aviação, um dos objetivos mais difíceis de alcançar tem sido aumentar o tempo de voo significativamente. Uma solução para este problema é captar energia solar para aumentar o tempo de voo, e idealmente atingir o voo perpétuo. Uma aeronave solar não precisa de ser reabastecida ou recarregada sempre que comece uma missão, em vez disso, a aeronave capta a energia solar durante o dia para fornecer energia durante o voo e para recarregar a bateria, e depois utiliza a energia armazenada para o voo noturno. Este processo reduz a necessidade de operações diárias.

Esta tese apresenta uma metodologia para projetar uma aeronave solar capaz de voar por longos períodos de tempo e dedicada à monitorização de vida selvagem. A metodologia desenvolvida baseia-se em trabalhos anteriores de Noth, adicionando a possibilidade de analisar vários perfis alares para a asa e cauda da aeronave, bem como calcular as respetivas características aerodinâmicas para obter resultados mais confiáveis. Também inclui uma segunda fase onde uma análise mais detalhada é realizada para fornecer resultados mais confiáveis para um determinado perfil de missão definido por um segmento diurno de alta altitude e um voo noturno de baixa altitude. No fim, uma terceira fase para análise de detalhes como conexões entre partes da aeronave é feita.

Para fazer uso desta metodologia é apresentado o projeto de um protótipo. Este protótipo serve para testar o conceito por trás de uma missão de uma aeronave de asa fixa que voa a uma latitude de 30°N para monitorizar animais selvagens por longos períodos de tempo. A aeronave também deve ser capaz de voar em qualquer dia do ano nesta latitude. Este protótipo é modular para que a envergadura da asa possa ser alterada, dependendo das necessidades energéticas ao longo do ano. Nesta latitude, o solstício de inverno tem 10.2 horas de luz durante o dia e 13.8 horas de noite. Apesar do protótipo voar apenas entre 1 hora antes de o nascer do Sol até 3 horas após o por do Sol, estes dados são importantes para a versão final da aeronave.

O projeto de uma aeronave solar capaz de voar vários dias é um problema complexo e multidisciplinar. Este trabalho mostra que mesmo para uma massa de carga útil muito reduzida, uma aeronave de asa relativamente grande é necessária devido a carga alar baixa requerida pela alta eficiência. Alem disso, parâmetros como densidade energética das baterias, área dos painéis solares, massa da estrutura, perfil da missão, localização da missão e época do ano tem efeitos importantes no tamanho e massa do projeto final.

Palavras-chave

Metodologia, Projeto conceptual, Projeto preliminar, Projeto detalhado, Estudos paramétricos, Protótipo, Voo perpétuo, Metodologia de projeto de um UAV solar.

Abstract

Since the beginning of human flight, one of the most difficult goals has been to make an aircraft to stay aloft for very long periods of time. One of the solutions to this problem is to harvest solar energy during flight to increase the flight time and ideally achieve perpetual flight. Generally a solar aircraft does not need to be refuelled or recharged every time it has to start a mission, instead it collects solar energy during the daytime for flight and to recharge the battery for night flight. This process reduces the need for daily operations.

This thesis presents a methodology to design a solar aircraft capable of flying for long periods of time which may be dedicated to monitoring wildlife. The developed methodology builds on previous works by Noth by adding the possibility of analysing several wing and tail airfoils as well as computing the corresponding aerodynamic characteristics to have more reliable results. It also includes a second phase where a more detailed analysis is performed to provide more reliable results for a given mission profile defined by a high-altitude day-time segment and a low altitude night flight.

To make use of this methodology, the design process of a prototype is presented. This prototype serves to test the concept behind a mission of a fixed wing aircraft that flies at a latitude of 30°N to monitor wild animals for very long periods of time. The aircraft should also be able to fly any day of the year at this latitude. This prototype is made modular, so the wingspan can be increased or decreased depending on the energy needs along the year. At this latitude, the winter solstice has 10.2 hours of daylight and 13.8 hours of nighttime. Despite the prototype only flying from 1 hour before sunrise to 3 hours after sunset, this data is important for the full-scaled version.

The design of a solar aircraft capable of flying several days is a challenging, complex and multidisciplinary problem. This work shows that even for a very light payload, a relatively large wing aircraft is needed due to the very low wing loading required for high efficiency. Also, parameters such as battery energy density, solar panel area ratio, structural mass, mission profile, and mission location and time of the year have important effects on the final design size and mass.

Keywords

Methodology, Conceptual design, Preliminary design, Detail design, Parametric study, Prototype, Perpetual flight, Solar UAV design methodology.

Contents

1 Introduction **1**

1.1 Motivation and objectives 1

1.2 State of the art 2

1.3 Structure of the work 6

2 Methodology **9**

2.1 General concept 10

2.2 Conceptual design 12

2.2.1 Airframe mass model 14

2.2.2 Solar module 14

2.2.3 Aerodynamic module 15

2.2.4 Performance module 17

2.3 Preliminary design 18

2.3.1 Aerodynamic module 23

2.3.2 Propulsive module 24

2.3.3 Climb module 25

2.3.4 Descent module 26

2.3.5 Take-off module 27

2.3.6 Other performance metrics 28

2.4 Detailed design 28

3 Conceptual design **31**

3.1 Mission requirements 31

3.2 Payload 32

3.3 Data and airfoils 33

3.4 Conceptual analysis 35

4 Preliminary and detailed design **39**

4.1 Parametric studies 39

4.2 Prototype aircraft 43

4.2.1 Components selection 43

4.2.1.1 Propulsion group 43

4.2.1.2 Electronics group 44

4.2.1.3 Avionics and control group 44

4.2.2 Winter aircraft analysis 45

4.2.3 Summer aircraft analysis 49

4.2.4 Components inside the fuselage 51

4.2.5 Wing structure 52

4.2.5.1 Spar 52

4.2.5.2 Rib 56

4.2.5.3 Leading edge 60

4.2.5.4 Solar cell encapsulation 61

4.2.5.5 Aileron structure and assembly 62

4.2.5.6 Servo mount 66

4.2.5.7 Wing tip 67

4.2.5.8 Wing connection 68

4.2.5.9 Validation of the structure 70

4.3 Perpetual flight aircraft 73

4.3.1 Components 74

4.3.2 Aircraft analysis 75

5 Conclusions **79**

Bibliography **81**

A Appendix **87**

A.1 Aircraft list 87

A.2 Detailed mass and position of all components for the prototype aircraft . . 90

A.3 Components correlations 91

A.4 Drag polar for the winter and summer prototype aircraft 93

A.5 Dynamic stability 94

A.5.1 Winter aircraft 94

A.5.2 Summer aircraft 95

A.6 Detailed drawings of the prototype aircraft 97

List of Figures

1.1 Sunrise I. 3

1.2 Solar Excel. 3

1.3 Solar Impulse 2. 4

1.4 Pathfinder (left) and Helios (right). 5

1.5 Zephyr S (left) and ApusDuo prototype (right). 5

2.1 Design process. 10

2.2 Conceptual design flowchart. 12

2.3 Mission profile. 12

2.4 Initial wing structure example to calculate correlations between mass and size of each component. 19

2.5 The Ragone Plot - Peak power and specific energy density of various energy storage methods 20

2.6 Preliminary design flowchart. 22

3.1 Payload components. A - Raspberry Pi HQ camera; B - Arducam 35 mm lens; C - FLIR Boson; D - Raspberry Pi 4. 33

3.2 Aircraft used to compute the correlation between airframe mass, wingspan and aspect ratio, and respective correlation plane. 34

3.3 Peak specific Sun power for one complete year and different latitudes. . . . 35

3.4 Average specific Sun energy for one complete year and different latitudes. 36

3.5 Total mass of the aircraft for several wingspan and aspect ratio values. . . 38

3.6 Wing airfoil, WE3.55-9.3. 38

3.7 Tail airfoil, E193 inverted. 38

4.1 Wingspan and total aircraft mass as functions of solar panel area ratio and battery specific energy. 40

4.2 Percent change in wingspan (left), and in total aircraft mass (right), with day, latitude, airframe mass and altitude at night during cruise. 40

4.3 Propulsion components for the prototype aircraft. A - 20 in x 10 in propeller; B - Hacker A50-16 L V4 motor; C - Mezon Pro 85 ESC. 44

4.4 Energy components for the prototype aircraft. A - MaxAmp battery with 11 Ah capacity; B - Genasun GVB-8 MPPT; C - Stack of Sunpower C60 solar cells. 44

4.5 Avionics and control components. A - Dragonlink setup components; B - Pixhawk 4; C - Corona CS-939MG servo. 45

4.6 General representation of the winter aircraft. 46

4.7 Energy and power graphs for the winter aircraft mission. 47

4.8 V-n diagram for the winter aircraft, with $\hat{u}$ as the mean gust velocity. . . . 48

4.9 Energy and power graphs for the summer aircraft mission. 50

4.10 V-n diagram for the summer aircraft, with $\hat{u}$ as the mean gust velocity. . . 50

4.11 Components layout inside the fuselage. 51

4.12 Complete wing structure without solar cells. 52

4.13 Wing panels layout. 53

4.14 Pressure coefficient graph for the wing airfoil with a Reynolds number of 300,000 and 4 degrees of angle of attack. 57

4.15 Ratio between the force from the leading edge to the spar (front load) with relation to the total load. 57

4.16 Safety factor of the carbon fiber sandwich wing rib from the software structural analysis. 58

4.17 Carbon fiber sandwich rib, with a bidirectional sandwich marked by the red areas. 58

4.18 Balsa rib with airfoil outline in black. 59

4.19 Balsa rib used on the aileron panel with airfoil outline in black. 59

4.20 Setup for testing the balsa ribs. 59

4.21 Plywood rib with airfoil outline in black. 60

4.22 Plywood rib used on the aileron panel with airfoil outline in black. 60

4.23 Leading edge structure. 61

4.24 Solar cell layout. Purple - grid 3 by 14; Green - grid 3 by 14; Blue - grid 4 by 6; Red - grid 1 by 7. 61

4.25 Solar cell encapsulation layers. 62

4.26 Pressure coefficient as a function of the relative position of the chord, $\bar{x}$, where the red boundary represents the aileron position. 63

4.27 Aileron spar tip with cable guide. 64

4.28 Aileron tip ribs (left) and middle (right). 64

4.29 Aileron control horn. 65

4.30 Complete aileron. 65

4.31 Aileron mounting. 66

4.32 Servo mount, outter part. 66

4.33 Servo mount, inner part, for the inner control surface (left) and outer control surface (right). 67

4.34 Servo integration with the aileron. 67

4.35 Final wing tip. 68

4.36 Wing spar, torsion and axial connectors. 69

4.37 Wing connector for the fuselage and applied loads. 70

4.38 Maximum principal stress (left) and maximum shear stress (right), in MPa, for the connector between the wing and the fuselage. 70

4.39 Jig used to help build the structure. 71

4.40 Panel torsion and axial connectors on the built wing section. 71

4.41 Leading edge of the built section. 72

4.42 New servo mount and reworked trailing edge of the wing panel with the small ribs. 72

4.43 Reworked aileron mounting with flushed hinges and increased leading edge balsa sheet thickness. 73

4.44 Built wing section. A - Without skin and solar cells; B - With skin on the bottom and without solar cells; C - With skin on the bottom and solar cells on top of the section. 74

4.45 Full size aircraft components. A - Hacker Q100 - 7L motor; B - Jeti SPIN Pro 300 opto ESC; C - MaxAmp battery with 23 Ah capacity; D - MG Energy Systems WSC-Si MPPT. 75

4.46 Total aircraft mass of several perpetual flight capable aircraft in function of wingspan. 76

4.47 Energy and power graphs for the perpetual aircraft at winter solstice. . . . 77

A.1 Correlation between the power and mass of the motors. 91

A.2 Correlation between the power and mass of the ESC. 91

A.3 Correlation between the power and mass of the MPPT. 91

A.4 Correlation between the energy capacity and mass of the batteries. 92

A.5 Drag polar for the winter (blue) and summer (red) aircraft. 93

A.6 Pitching response graph for the winter aircraft. 94

A.7 Phugoid response graph for the winter aircraft. 94

A.8 Roll response graph for the winter aircraft. 94

A.9 Dutch-roll response graph for the winter aircraft. 94

A.10 Spiral response graph for the winter aircraft. 95

A.11 Pitching response graph for the summer aircraft. 95

A.12 Phugoid response graph for the summer aircraft. 95

A.13 Roll response graph for the summer aircraft. 95

A.14 Dutch-roll response graph for the summer aircraft. 95

A.15 Spiral response graph for the summer aircraft. 96

List of Tables

3.1 Conceptual analysis results. 37

4.1 Avionics and control components mass and power. 45

4.2 Winter prototype aircraft characteristics. 46

4.3 Mission metrics for the winter prototype aircraft 48

4.4 Summer prototype aircraft characteristics. 49

4.5 Mission metrics for the summer prototype aircraft 51

4.6 Torayca T700 mechanical properties. 54

4.7 Wing loading for the wing spar sizing. 54

4.8 Spar properties for each section. 55

4.9 Aileron spar properties. 63

4.10 Hinge position marked by the percent increase to the final load in the intermediate panel ribs. 65

4.11 Spar connector layers and dimensions. 68

4.12 Perpetual flight aircraft characteristics. 76

A.1 Database of solar aircraft. 87

A.2 Mass and position of all components of the prototype aircraft. 90

Nomenclature

α	Angle of attack
Δh	Altitude step
$\delta C_{L_H/\delta\delta_H}$	Variation of the lift coefficient of the equivalent horizontal tail with the movement of the control surface
$\delta C_l/\delta\alpha$	Variation of the lift coefficient of the airfoil with the angle of attack
δ_{cr}	Throttle level in cruise
δ_{Sun}	Declination of the Sun
$\delta C_{M/\delta\alpha}$	Ratio between the pitching moment coefficient and angle of attack of the aircraft
δ_H	Deflection of the control surface of the tail
$\eta_{eff_{prop}}$	Effective efficiency of the propeller
η_f	Correction of the propeller efficiency due to friction forces of the airflow
$\eta_{overall}$	Overall efficiency of the motor and propeller
γ	Flare angle during landing
μ_{TO}	Rolling drag coefficient during takeoff
μ	Air viscosity
ρ_{LD}	Air density at landing altitude
ρ_{TO}	Air density at takeoff altitude
ρ	Air density
σ_{bottom}	Tensile stress of the bottom point for a specific station
σ_{left}	Tensile stress of the left point for a specific station
σ_{max}	Maximum tensile stress of a station
σ_{right}	Tensile stress of the right point for a specific station
σ_{top}	Tensile stress of the top point for a specific station
τ_{bottom}	Shear stress of the bottom point for a specific station
τ_{left}	Shear stress of the left point for a specific station
τ_{right}	Shear stress of the right point for a specific station
τ_{shear}	Maximum shear stress of a station due to shear force
τ_{top}	Shear stress of the top point for a specific station
$\tau_{torsion}$	Maximum shear stress of a station due to pitching moment
θ_{Sun}	Solar Zenith

$2D$	Bi-dimensional
$3D$	Tri-dimensional
A_1	Takeoff constant
A_2	Landing constant
$A_{LE_{tail}}$	Surface area of the leading edge of the tail
$A_{LE_{wing}}$	Surface area of the leading edge of the wing
$A_{rib_{tail}}$	Surface area of one rib of the tail
$A_{rib_{wing}}$	Surface area of one rib of the wing
A_{SC}	Solar cell area
$A_{skin_{tail}}$	Surface area of the tail skin
$A_{skin_{wing}}$	Surface area of the wing skin
A_{solid}	Full cross-section area of the station
$A_{spar_{tail}}$	Surface area of the tail spar
$A_{spar_{wing}}$	Surface area of the wing spar
$A_{station}$	Cross-section area of the station
$A_{tailboom}$	Surface area of the tailboom
$a_{TO_{partial}}$	Acceleration during a takeoff speed step
a	Speed of sound
AR	Aspect ratio
$b_{aileron}$	Aileron span
b	Wingspan
C_{D_o}	Parasitic Drag of the lifting surface
$C_{D_{AC_{LD}}}$	Average drag coefficient of the aircraft during landing
$C_{D_{AC_{TO}}}$	Average drag coefficient of the aircraft during takeoff
$C_{D_{AC}}$	Drag coefficient of the aircraft
C_{D_i}	Induced drag of the lifting surface
$C_{D_{other}}$	Drag coefficient of other parts of the aircraft besides the wing and tail
$C_{D_{RC_{max}}}$	Drag coefficient for the maximum climb rate
$C_{D_{tail}}$	Drag coefficient of the tail
C_{D_W}	Drag coefficient of the wing
C_D	Total drag of the lifting surface
c_f	Friction coefficient
$C_{H_{mom}}$	Aileron hinge moment coefficient
c_H	Tail chord

$C_{l_{\alpha=0}}$	Lift coefficient of the airfoil for an angle of attack of 0 degrees
$C_{L_{AC_{LD}}}$	Average lift coefficient during landing
$C_{L_{AC_{max}}}$	Maximum aircraft lift coefficient
$C_{L_{AC_{TO}}}$	Average lift coefficient during takeoff
$C_{L_{AC}}$	Aircraft lift coefficient
$C_{L_{H_{equilibrium}}}$	Lift coefficient of the equivalent horizontal tail for the aircraft to be in equilibrium
$C_{L_{H_{no\ ctrl}}}$	Lift coefficient of the equivalent horizontal tail without movement of the control surface
C_{L_H}	Lift coefficient of the equivalent horizontal tail
$C_{l_{max}}$	Maximum lift coefficient of the airfoil
C_{L_W}	Lift coefficient of the wing
C_L	Lift coefficient of a finite wing
C_{M_H}	Pitching moment coefficient of the equivalent horizontal tail
C_{M_W}	Pitching moment coefficient of the wing
$C_{P_{mot}}$	Power coefficient of the motor
$C_{P_{prop}}$	Power coefficient of the propeller
c_W	Wing chord
D_{AC}	Drag of the aircraft
D_{prop}	Propeller diameter
$D_{station}$	Diameter of a station
E_{bat}	Energy of the battery
$E_{clb_{partial}}$	Energy used during climb for a given altitude step
$E_{D_{av}}$	Average sun energy for a given day and latitude
e	Oswald efficiency factor
f_{strut}	Safety factor for the airframe mass
F	Rolling drag during takeoff
f	Throttle level
g	Gravity
h_D	Angular hour
H_{mom}	Aileron hinge moment
h_{obs}	Obstacle height
I_O	Idle current of the motor
I_{eff}	Effective current of the motor

$I_{station}$	Inertia of the cross section of a station
$I_{Sun_{max}}$	Maximum Sun irradiance
I	Current
J_{factor}	Correction factor for the propeller advance ratio
J	Advance ratio of the propeller
k_{af}	Airframe mass constant
K_v	Speed constant of the motor
K	Induced drag constant
L/D	Ratio between the lift and drag of the aircraft
L_{AC}	Aircraft lift
l_{fus}	Length of the fuselage
l_{tail}	Distance between the leading edge of the wing and the leading edge of the tail
Lat	Latitude
m_{AC}	Aircraft mass
m_{af}	Airframe Mass
m_{bat}	Battery mass
m_{ESC}	Electronic speed controller mass
$m_{fuselage}$	Mass of the fuselage
$m_{LE_{tail}}$	Mass of the leading edge of the tail
$m_{LE_{wing}}$	Mass of the leading edge of the wing
m_{mot}	Motor mass
m_{MPPT}	Maximum power point tracker mass
$m_{rib_{tail}}$	Mass of the tail ribs
$m_{rib_{wing}}$	Mass of the wing ribs
m_{SC}	Solar cells mass
$m_{skin_{tail}}$	Mass of the tail skin
$m_{skin_{wing}}$	Mass of the wing skin
$m_{spar_{tail}}$	Mass of the tail spar
$m_{spar_{wing}}$	Mass of the wing spar
m_{tail}	Mass of the tail
$m_{tailboom}$	Mass of the tailboom
$m_{TE_{tail}}$	Mass of the trailing edge of the tail
$m_{TE_{wing}}$	Mass of the trailing edge of the wing

m_{TO}	Total takeoff mass
m_{wing}	Mass of the wing
n_D	Day of the year
$N_{h_{max}}$	Maximum number of sunlight hours for a given latitude
$N_{h_{min}}$	Minimum number of sunlight hours for a given latitude
N	Rotation speed of the motor
n	Load factor
P_{ele}	Total electric power
$P_{elec_{RC_{partial}}}$	Electrical power used for a given altitude step during climb
P_{ESC}	Electronic speed controller power
P_{mot}	Motor power
P_{MPPT}	Maximum power point tracker power
$P_{prop_{cr}}$	Propulsive power in cruise
P_{prop}	Propulsive power
P_{req}	Required power
R	Internal electric resistance of the motor
$RC_{partial}$	Climb rate for an altitude step
Re_f	Reynolds number of the fuselage
Re	Reynolds number
S_c	Cross-section area of the fuselage
S_H	Equivalent horizontal tail area
$s_{LD_{circ}}$	Landing distance
s_{LD}	Landing distance in contact with the ground
$s_{TO_{partial}}$	Distance of one takeoff speed step
s_{TO}	Total takeoff distance
S_W	Wing area
S_{wet}	Wet area
$t_{clb_{partial}}$	Partial time for an altitude step during climb
t_D	Sunlight time for a given day
$t_{station}$	Thickness of the cross-section of a station
$t_{TO_{partial}}$	Partial time of one takeoff speed step
T_W	Pitching moment of the wing
T	Trust force
U_i	Induced voltage

U_{max}	Maximum voltage
U	Voltage
$\hat{u}$	Mean gust velocity
V_{LO}	Lift off speed
$V_{RC_{partial}}$	Velocity for a given altitude step during climb
V	Velocity
x_1	First exponent constant of the airframe mass model
x_2	Second exponent constant of the airframe mass model
$x_{station}$	Position of the station from the center plane of the aircraft
$x\bar{_{CG}}$	Relative position of the center of gravity from the leading edge of the wing
$\bar{x}$	Relative position from the leading edge of the wing

Acronyms

BMS	Battery Management System
CG	Center of Gravity
CNC	Computer Numerical Control
ESC	Electronic Speed Controller
FEUP	Faculdade de Engenharia da Universidade do Porto
FoV	Field of View
GPS	Global Positioning System
MPPT	Maximum Power Point Tracker
UAV	Unmaned Aerial Vehicle
UBI	Universidade da Beira Interior

Chapter 1

Introduction

1.1 Motivation and objectives

Since the beginning of the aviation era, one of the most challenging objectives has been to increase the endurance. Currently, missions such as border surveillance, forest fire fighting, or power line inspection can be accomplished with an endurance of a couple of hours. Nevertheless, long endurance missions, namely communication platforms for mobile devices, weather forecast, and environmental monitoring require several days of airborne operation. To address this limitation, one solution is to use electric solar unmanned aerial vehicles (UAV). These vehicles use solar cells to harvest energy from the Sun during the day and power all systems, including the chargers for the batteries that enable night-time flight. With these systems, it is possible to achieve long endurance in comparison to normal electric or internal combustion engine aircraft since the need to land for recharging or refuelling is not present. Electric aircraft are limited by the energy storage solution, the battery, which has low energy density when compared with fossil fuels. The internal combustion engine, on the other hand, is significantly less efficient than the electric motor, produces more noise and pollution to the atmosphere while also needing constant refuelling between missions.

One of the applications that motivated this thesis was a project created in Faculdade de Engenharia da Universidade do Porto (FEUP), where a solar UAV should be developed to fly in Nepal, with a maximum latitude of 30° N, any time of the year. The objective of this aircraft is to monitor wildlife. There are already methods to monitor wildlife, namely the use of tags for wild animals; however, this method is not only invasive but can also be dangerous, since the capture of the animal for a short period of time is required, and constant tracking and maintenance by a ground crew to collect data and check the status of the tag is needed. With the help of a solar UAV, it is possible to monitor a specific animal or group of animals in real time, for very long periods of time without the need of constant maintenance or a crew on the terrain near the animal.

The process of designing a solar UAV is a very complex and multidisciplinary problem involving not only aerodynamics, propulsion, and structure, but also the implementation of a payload and energy systems that should be carefully designed. The combination of all aircraft systems creates an iterative loop where a small change in one system can drastically change some other system.

The methodology shown in this thesis was first developed as a tool for a group project, for the Aircraft Design class at Universidade da Beira Interior (UBI), where it was necessary to develop a solar UAV to monitor livestock. This methodology was adapted for designing a solar UAV while having into account the mission requirements of FEUP project. For the mission success, it is required that the aircraft flies any time of the year at the given latitude, while cruising at different altitudes during day and night time, to monitor wildlife. To validate the concept and design methodology a solar UAV capable of performing such mission should be designed. For simplicity and for budgetary reasons, a prototype will be designed instead of a full-scale aircraft. This prototype will have an endurance of less than 24 hours.

To achieve this objective, a design process composed by three main phases is presented [1]: the conceptual phase, where the configuration, size, requirements, etc. are tested in low detail but a good understanding of the relationship between the components of the aircraft is essential; preliminary design, where the systems are analysed together for a better understanding of the aircraft and parametric studies are conducted in order to acknowledge the influence of some design variables; lastly, the detailed design, where fabrication, connections and other characteristics not included on the other phases are taken into account. This thesis mainly focuses on the conceptual and preliminary design phases; nonetheless, the development of the detailed design of the wing section is also presented.

1.2 State of the art

The use of electric motors is not a novelty. The first electric powered flight occurred in France, in 1884, where a hydrogen-filled dirigible with electric motors won a 10 km race around Villacoulbay and Medon [2], where the only opponent was the steam engine. Later, with the emergence of the internal combustion engine, the work on electric aircraft was nearly forgotten [2].

In 1954, the first silicon solar cell technology appeared at Bell Telephone Laboratories with 4 % efficiency, which rapidly increased to 11 % [3]. Only 20 years later was the solar cell technology used to gather energy to fly. In 1957, Colonel H. J. Taplin made the first recorded electric powered radio-controlled flight with his model, *Radio Queen*.

The first solar-powered model aircraft, *Sunrise I*, created in 1974, by R.J. Boucher from Astro Flight Inc, with a wingspan of 9.76 m, mass of 12.25 kg and an output of 450 W from 4096 solar cells, flew for 20 minutes in the dry lake of Camp Irwin at an altitude of 100 m above ground [2]. Later, in 1975, *Sunrise II* was built with the same wingspan as *Sunrise I*, but with a mass of 10.21 kg. With 4480 solar cells, it was then capable of producing 600 W of power (mainly due to the increase in efficiency to 14 %).

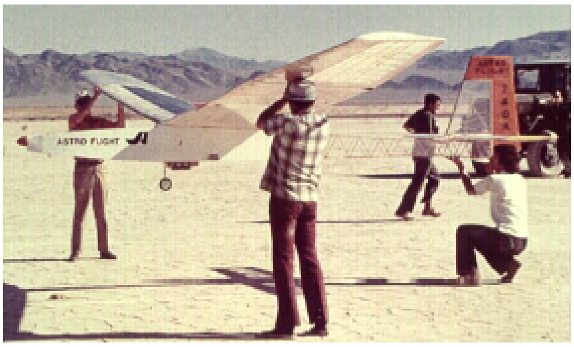

Figure 1.1: Sunrise I [4].

Another important landmark at that time was the solar aircraft *Solaris*, from Fred Militky. It completed three flights of 150 seconds at 50 m altitude. Other people, such as Dave Beck, who set two records in the F5 category with *Solar Solitude* that flew 38.84 km and could reach 1283 m of altitude [5]; Wolfgang Schaeper who was also distinguished at the time for *Solar Excel*, with a flight duration of more than 11 hours, 48.31 km travelled in straight line, 2065 m gained in altitude and a speed of 80.63 km/h [4].

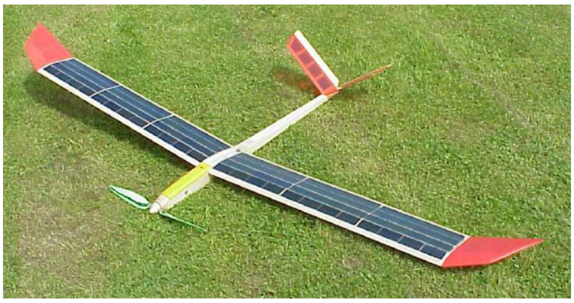

Figure 1.2: Solar Excel [4].

The interest of the use of solar power in aircraft started to rapidly increase and evolve.

With the concept of solar models proven, Britons David Williams and Fred To developed *Solar One* in 1978, the first manned solar aircraft [6]. Other manned solar aircraft like the *Solar Riser* and *Gossamer Penguin* also marked important stages in solar flight, despite the latter being deemed too unsafe to fly high above ground. Another important manned solar aircraft is *Solar Challenger*, a 14.2 m wingspan with 16128 solar cells capable of 2500 W, that crossed the English Channel. It flew 5 hours and 23 minutes, covering 262.3 km. While this project occurred, *Solair I*, a German competitor was also trying to achieve the same result, with a 16 m wingspan and 2499 solar cells producing a maximum power of 1800 W; however, due to the smaller solar cells area it needed a 22.7 kg nickel-cadmium battery [2].

In 1989, *Sunseeker*, an aircraft built by Eric Raymond, crossed the USA in 21 solar-powered flights performing a total of 121 hours of flight [7]. More recently, *Solar Impulse 2* flew around the Earth in seventeen stages during sixteen and a half months in 2015 [8].

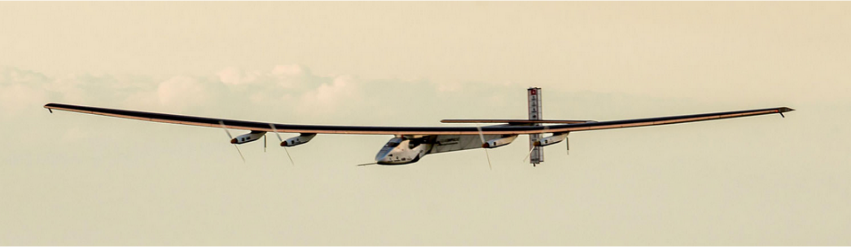

Figure 1.3: Solar Impulse 2 [9].

With the increasing development of solar aircraft, the concept of high-altitude, high endurance aircraft started to appear. The first prototype built was from AeroVironment Inc, who started to study these types of aircraft capable of flying above 19,812 m (65,000 ft). At this point, one of the major step backs was the energy storage systems which were inadequate for this type of missions. The solution to this problem was the use of solar power, and thus the first solar aircraft for high altitude long endurance missions, *Pathfinder*, with 30 m of wingspan and 254 kg of mass, was built and made its first flight in 1993 at Dryden. It broke the altitude record by reaching 15,392 m, and two years later reached 21,802 m. Following *Pathfinder*, there were developed new versions, like *Pathfinder Plus* with a larger wingspan and new systems, *Centurion* that was a technology demonstrator, and later the *Helios* family [4].

Other projects also presented a huge development of this type of aircraft. *Solitair* had 5.2 m of wingspan and adjustable solar panels for optimal radiation absorption. The *Helinet* project studied the feasibility of a solar-powered high-altitude aircraft with 73 m wingspan and 750 kg named *Heliplat*. It reached the prototyping phase with a 24 m wingspan prototype, which developed to a new project for an aircraft named *Shampo* [10, 11].

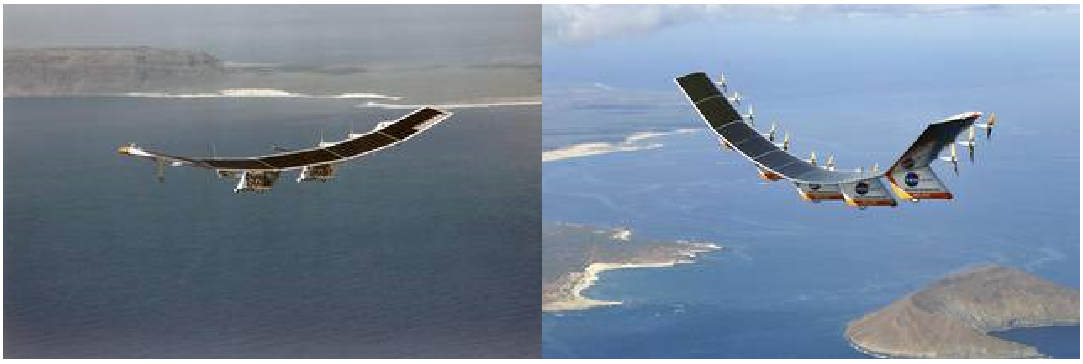

Figure 1.4: Pathfinder [12] (left) and Helios [13] (right).

Other companies also began to develop new solar aircraft, like *Zephyr* that hold the current record of endurance and altitude. The latest version, *Zephyr S*, has a 28 m wingspan and a total takeoff mass of around 75 kg. In the summer of 2008, it flew non-stop for almost 26 days [8]. There are also companies that are still in prototyping phase before building a full-scale aircraft. For example, *Phasa 35*, with a more conventional configuration and a UAVOS aircraft, *ApusDuo*, that uses a tandem configuration [14].

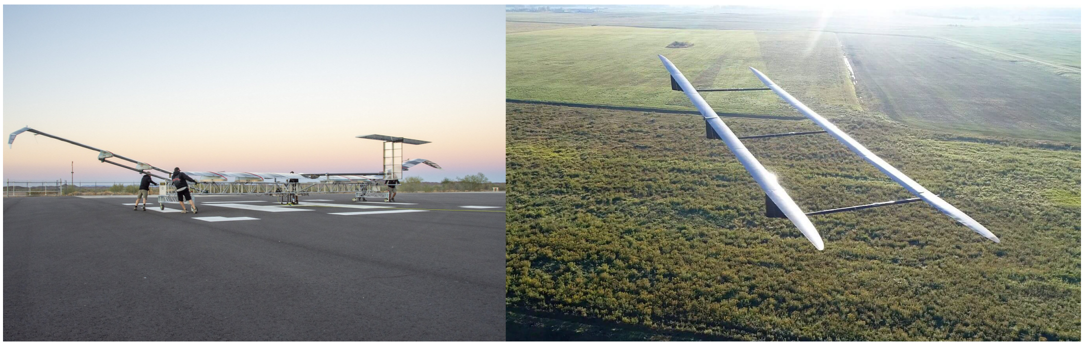

Figure 1.5: Zephyr S [15] (left) and ApusDuo prototype [16] (right).

It is also possible to find a great academic interest in solar aircraft too. For example, *AtlantikSolar* [17] holds the current endurance record for aircraft under 50 kg with 81 hours of continuous flight time; and André Noth aircraft *Sky-Sailor* [4] which was designed to fly on Mars.

As for the design process, very little information is available in the literature, and most of it is focused on the theoretical level. It is a complex matter and the designers of most aircraft do not make the design process publicly available, or publicate the process without validation. For instance, from *Sunrise*, Boucher published, in 1979, a description of the performance and hardware of the aircraft but did not describe the design methodology [18]. Gedeon, in 1978, presented the idea of the feasibility of solar aircraft [19], Schoeberl published his work on the propulsion and aerodynamics [20, 21], while Colozza presented the implementations of the solar cells [22].

The first time the design process was presented was in 1974, by Irving, for a manned aircraft [23], allowing the mass of several components to vary with wingspan and power. Bailey, in 1992, separated the mass models for the motor, controller, gearbox, propeller and fuel cell [24]. Hall and Hall developed a very accurate method for calculating the airframe mass of a solar aircraft, but it has proven to be very complex since it considered every element of the structure [25]. Most authors simplify the airframe mass model by making it proportional to the wingspan [26], but this method rapidly decreases the range for the validity of the model. Another source of information is work done by students in the academic environment, from design process and construction of prototypes to validate the methodologies used. For example, a team of students in Israel built *SunSailor* and presented the design methodology in 2006 [27], and from a consortium of Portuguese universities developed in 2014 a solar UAV for civilian applications with an endurance of 8 hours [28].

1.3 Structure of the work

This thesis can be divided into two main parts. In the first part, the methodology is presented, while the second part shows how the methodology was used for the current project.

The first part can be divided into three main phases. The first focuses on the conceptual design and is highly based on Noth work for *Sky-Sailor* [4]. Some modifications were made in order to analyse a greater range of configurations, such as the ability to analyse several combinations of airfoils for the wing and tail sections of the aircraft, the ability to calculate the aerodynamic coefficients for such airfoils and the calculation of extra performance metrics, such as takeoff distance and battery used to climb from takeoff to cruise altitude. Data for the Sun and airframe mass models is also presented. Next, the preliminary design, which begins with the values obtained from the previous design phase, is described. These values are iterated to obtain a more realistic aircraft configuration.

In this phase, it is also possible to obtain important performance metrics, such as flight speed, incidence angle of the wing and tail section of the aircraft, and energy used during the mission. In the end, the mission feasibility for a given aircraft configuration is also verified. Finally, the detailed design is presented. This design phase is tightly bonded with the preliminary design since results from the detail design can change important parameters of the preliminary design.

The second part, having the methodology explained, shifts the focus to the solar UAV design for the given project. In these chapters, in a similar structure as the one shown on the methodology is followed. It begins with the conceptual design, where the mission is defined as well as the payload to be used. Several airfoils for the wing and tail sections are also analysed, as well as the general configuration of the aircraft. The preliminary design starts by establishing some components based on the conceptual design, such as motor, maximum power point tracker (MPPT) and electronic speed controller (ESC). The correct components for the avionics systems are also chosen since in this phase the components need to be fixed and the aircraft should be designed around its payload and avionics systems. During this phase of the project, the size of the aircraft is iterated in conjunction to the power systems (that include the battery and solar cells), in order to find the size of the aircraft that best fit the mission. In this phase, an analysis for a possible full-scale aircraft is also made. It is important to note that the results from the full-scale analysis is only theoretical since it depends on the final real-world prototype performance in order to make corrections to the calculations in the analysis. Finally, a detailed design of the wing section of the aircraft is presented, where the structure of the wing is explained in detail.

In the end, a conclusion that includes future work, problems and lessons learned is presented.

Chapter 2

Methodology

Is this part of the document, the methodology developed will be exposed and explained in detail. This methodology, as can be seen in the following sections, it can be divided into three main phases.

The conceptual design phase will focus more on the search for aircraft with similar missions, components (for example: motors, ESC and MPPT in order to find correlations of mass with power or area with mass in case of the solar cells), payload type to complete the mission, airfoils for the wing and tail section of the aircraft and lastly, initial values for the aircraft size and components mass. Next, with the data from the conceptual design it is possible to pass to the preliminary design, where a more detailed analysis of the aircraft is made. In this part of the design, the components inside the aircraft will be fixed. Instead of analysing several aircraft configurations, meaning several combinations of wingspan, aspect ratio or chord, and airfoils, the aircraft configuration will be iterated in order to find the most efficient configuration for the mission. This will require not only parametric studies, but also an iterative process with all aircraft systems. In the end, the last stage of the design process, the detailed design will be presented. This design phase focus on the details that were left apart on the previous design phases, for example the connections between wing panels, fabrication process of the parts that constitute the aircraft as well as their assembly.

As said in Section 1.1, the methodology presented was adapted from previous class works in order to better fit the requirements of FEUP project, and to give more reliable results. Some of this changes that include, for example, the ability of having a mission with different cruise altitudes during day and night time, while the climb and descend time between these two altitudes are fixed by mission requirements.

2.1 General concept

A summary of the complete design process can be seen in Figure 2.1.

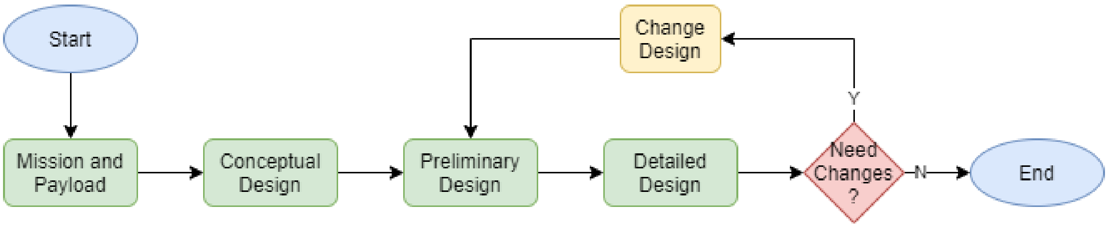

Figure 2.1: Design process.

The design process starts by creating a mission for a given application. So, the mission requirements should be well-defined earlier on. These requirements can change along the design process, but that will mean a change on the complete design and a need to correct past calculations. After the mission requirements are well-defined, a search for the payload configuration to complete the mission should be done, since the aircraft is designed around this system.

Next, it is possible to start the conceptual design. As the name suggests, in this phase the objective is to have the concept of the aircraft fixed. For that, a search for similar aircraft missions is done. This will help find patterns on the configuration of the aircraft and limit the number of aircraft considered to have more adequate data to compute correlations for some variables. It is also needed to do a compilation of components that will compose the several systems of the aircraft. For example, for the propulsion system a motor, ESC, propeller and optionally a gearbox; and in case of the energy system, batteries, battery management system (BMS), MPPT and solar cells are used. With the data of these components, it is now possible to compute linear correlations for the components properties. This step is important since the size of the aircraft is still unknown. The correlations will help to choose the correct components when the preliminary design starts. A database of airfoils should also be put together for the wing and tail sections of the aircraft. This database will allow to search for the most efficient combination of airfoils for the wing and tail sections. Lastly, an airframe mass model with similar aircraft should be developed in order to correlate the mass of the airframe with the size of the aircraft. With all the above data, it is possible to test several aircraft configurations in order to find the best size, airfoils and components mass for an aircraft that can complete the mission.

The preliminary design phase starts by choosing the correct components from the masses and power obtained from the previous phase, and the database created at the beginning of the design process. It is important to note that some components such as the propeller and battery configuration will be iterated in this phase, since a more detailed analysis will be done. Having fixed most of the components, a database of several propellers should be made in order to find the best propeller that maximizes the efficiency of the propulsion group. Then some parametric studies to understand the influence of some design variables on the size and total mass of the aircraft should be made. This will help fix for example the solar area ratio, which is the ratio between the solar cells area and the wing area. Having these concepts in mind, an iterative process for a given aircraft configuration can start. In the end of this design phase, it is possible to have the size of each part of the aircraft, the specific components that will be inside each system, and some mission performance metrics. Note that during this design phase, test should be made on each system individually to check for consistency with the results from the iterative process.

Having the preliminary design analysis finished, it is possible to pass to the detailed design phase of the project. It this phase, the main focus is the details, fabrication and assembly of the aircraft. Here the details such as connections between wing panels, to transmit torsion and bending loads and to prevent axial motion of the panels, are designed according to the specific stress requirements. The same can be done to the tail section of the aircraft, since the tail can be designed similarly to the wing of the aircraft. As for the tail boom and fuselage, the connections between these elements and the lifting surfaces should be designed too. Other elements should also be designed in this phase, for example the ailerons and tail control surfaces, that were only considered in the preliminary analysis but not fully designed. This process should always keep in mind the simplest fabrication processes with the available materials, and easiness of assembly before flying. In addition, structural tests on critical parts of the aircraft should be done to validate the designed structure. It is also important to note that this part of the design process is highly connected to the preliminary design phase, since change in some parts of the aircraft can drastically change the initial design output from the preliminary design phase. If that happens, corrections to the preliminary design should be made in order to have a more accurate design.

2.2 Conceptual design

In order to better understand this part of the design process, a flowchart is presented in Figure 2.2. In this part of the document, the conceptual design process will be explained in more detail.

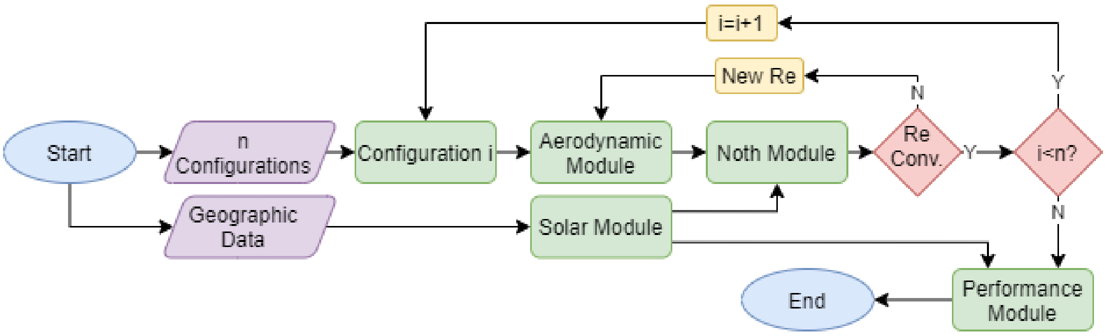
i=i+1
New Re
Start
n Configurations
Configuration i
Aerodynamic Module
Noth Module
Re Conv.
i<n?
Y
N
Geographic Data
Solar Module
End
Performance Module

Figure 2.2: Conceptual design flowchart.

As stated in the previous section, the mission, payload requirements and concepts should already have been thought of. Since the mission profile can include different altitudes during the day and night cruise, for this phase of the design process a weighted average, with time and altitude of flight for the atmospheric properties (including the air density and viscosity) is made. This process was necessary, since this part of the design is based on Noth work that only takes into account level flight throughout the mission [4]. This strategy of using a higher flight altitude during the day provides a way of storing extra solar energy as gravitic potential energy that can be used during the begining of the night descend phase. Since the energy saved as gravitic potential energy is not stored in the batteries their overall mass can be reduced, resulting on a smaller aircraft. Figure 2.3 shows a typical mission profile with the altitude changes along the day.

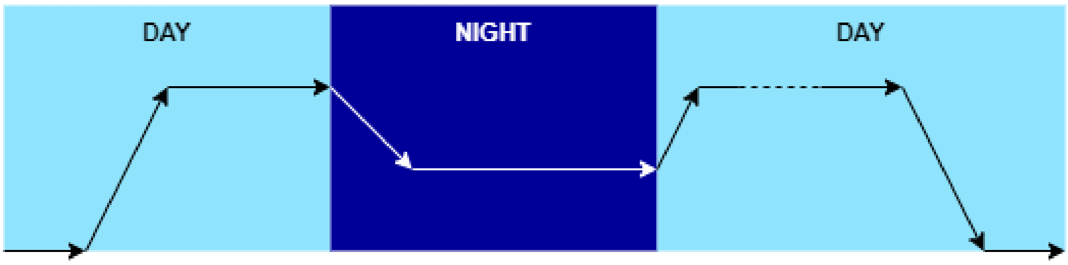
DAY
NIGHT
DAY

Figure 2.3: Mission profile.

Next, a compilation of solar UAVs with similar missions should be made. This search of similar UAVs will not only help to identify patterns on the design, but it will be very important to define the airframe mass model relations. Following this step, a compilation of components and airfoils for the aircraft should be put together. While the compilation of components is important to create correlations for the propulsion system and MPPT with its power and mass, and correlation between area and mass of the solar cells. The airfoils' database will be helpful to decide which airfoil to use on the wing and tail sections of the aircraft. It is important to note that it is possible to design a specific airfoil for the wing and tail sections for a specific mission, but that is not only time-consuming but also unnecessary since a very large range of airfoils to choose from already exists.

Other factors to consider are the solar and airframe mass model of the aircraft. The solar module will be used to calculate the average energy the aircraft is receiving from the Sun, while the mass model will use the database of aircraft created in the beginning to compute correlations between the size and mass of the airframe.

Next a range of wingspans, aspect ratio and combination of airfoils to use on the wing and tail sections of the aircraft is chosen to create the analysis range for these parameters. Other important geometric parameters are the tail volume coefficients and the distance between the wing and tail sections of the aircraft. In this design phase the typical values for the vertical and horizontal tail volumes coefficient as well as the relation between the wingspan and distance from the wing to the tail is obtained from similar solar aircraft.

Starting the analysis for a given configuration of wingspan, aspect ratio and combination of airfoils, the method starts by calculating the solar properties for the mission latitude and time of the year. Next it passes to an aerodynamic module where the airfoils are analysed using XFOIL beforehand. Next, with the polars for a given Reynolds number it is possible to calculate the aerodynamic coefficients that will be explained in more detail later.

Following the aerodynamic module, the same process Noth used for *Sky-Sailor* [4] was used. This module takes all the data for a given configuration, including the aerodynamic coefficients of the wing and tail sections, and outputs the mass of the components of the aircraft, cruise speed, solar cells' area and power used during cruise. This speed will be iterated with the Reynolds number of the aerodynamic module in order to have the right coefficients for the output speed of the Noth module. At the end of this phase a performance module, where other metrics were also calculated in order to have enough data to filter the best airfoils was added. This extra metrics include for example the battery used from takeoff to cruise altitude, solar area ratio and takeoff distance.

2.2.1 Airframe mass model

The airframe mass model that will be used during this design phase is the same that Noth used for his solar UAV, where the airframe mass, m_{af}, is related to the wingspan, b, and aspect ratio of the wing, AR, with constants, k_{af}, x_1 and x_2, obtained from correlations with existing aircraft. This model is given by

$$m_{af} = k_{af} b^{x_1} AR^{x_2} \quad (2.1)$$

2.2.2 Solar module

Inside this module, the average Sun energy that is reaching the solar cells will be calculated. To start the calculation, it is needed to know the day of the year and latitude of the mission. These two parameters come from the mission requirements.

In order to calculate the average Sun energy, first the time duration while the Sun is above the horizon, t_D, is calculated as [29]

$$t_D = 3600 \left[12 + \frac{N_{h_{max}} - N_{h_{min}}}{2} \sin\left(\frac{2\pi}{365} (n_D - 79) \right) \right] \quad (2.2)$$

where $N_{h_{max}}$ and $N_{h_{min}}$ represent the maximum and minimum hours of sunlight during the year, and n_D is the day to consider.

Next the declination of the Sun, δ_{Sun}, is calculated from

$$\delta_{Sun} = -\arcsin(0.39779 \cos(0.01720(n_D + 10) + 0.03341 \sin(0.01720(n_D - 2)))) \quad (2.3)$$

Lastly, the cosine of the solar zenith, $\cos(\theta_{Sun})$, for a given time of the day is calculated as

$$\cos(\theta_{Sun}) = \sin\left(\frac{\pi}{180} Lat\right) \sin(\delta_{Sun}) + \left(\frac{\pi}{180} Lat\right) \cos(\delta_{Sun}) \cos(h_D) \quad (2.4)$$

where Lat is the latitude that must be taken into account and h_D the angular hour.

The average of the Sun energy, is calculated as

$$E_{D_{av}} = avg(\cos(\theta_{Sun}))I_{Sun_{max}}t_D \quad (2.5)$$

where $I_{Sun_{max}}$ is the Sun maximum irradiance.

2.2.3 Aerodynamic module

Inside this module, the objective is to calculate the aerodynamic coefficients of the aircraft that maximizes endurance in order to pass them to Noth module. This module is iteratively computed in conjunction with Noth module to converge the Reynolds number. Before starting explaining this module, it is important to note that all airfoils that are going to be used need to be analysed first in XFOIL in order to have the aerodynamic polars, which include the curves $C_l(\alpha)$, $C_d(C_l)$ and $C_m(C_l)$ for different angles of attack and Reynolds numbers.

First, since the aerodynamic coefficients from the XFOIL polars are for an infinite wingspan wing (2D wing), it is necessary to correct them to a finite wing (3D wing). For that, the lift coefficient of the wing is calculated using the lifting line method where the lift coefficient is related to the angle of attack times a coefficient related to the aspect ratio of the wing

$$C_L = \frac{\delta C_l}{\delta \alpha}\frac{AR}{AR+2}\alpha + C_{l_{\alpha=0}} \quad (2.6)$$

Next, the parasitic drag and pitching moment coefficients are obtained by interpolation of the polars from the XFOIL analysis. For the complete drag coefficient, the induced drag is added, as

$$C_{D_i} = \frac{C_L^2}{eAR\pi} \quad (2.7)$$

$$C_D = C_{D_0} + C_{D_i} \quad (2.8)$$

where C_L is the finite wing lift coefficient, AR is the aspect ratio of the lifting surface, α is the angle of attack of the lifting surface, $C_{l_{\alpha=0}}$ is the infinite wingspan lift coefficient for an angle of attack of 0 degrees, C_{D_i} is the induced drag coefficient, e is the Oswald number, C_D is the total drag coefficient of the lifting surface and C_{D_o} is the parasitic drag.

For Oswald number typical values around 0.9 for a rectangular wing are used [30].

Next to calculate the tail lift coefficient, the equilibrium of pitching moments around the center of gravity, *CG*, is calculated as it is presented in Equation 2.9. This process is iterated with the pitching moment coefficient of the tail, since in theory a more cambered airfoil on the tail would need less lifting force, due to the increased pitching moment coefficient. The drag coefficient of the tail, $C_{D_{tail}}$ is again interpolated from the aerodynamic polars obtained from the XFOIL analysis and then added to the induced drag.

$$C_{L_H} = \frac{S_W}{S_H(l_{tail} - \bar{x}_{CG} c_W)} \left[C_{M_W} + C_{M_H} \frac{c_H S_H}{c_W S_W} + C_{L_W} c_W \left(\bar{x}_{CG} - \frac{1}{4} \right) \right] \quad (2.9)$$

where S_W and S_H are the wing and tail areas, l_{tail} is the distance from the leading edge of the wing to the leading edge of the tail, $\bar{x}_{CG}$ is the relative position of the center of gravity on the wing and c_W and c_H are the chords of the wing and tail, respectively.

Lastly, the aircraft lift and drag coefficients are calculated as

$$C_{L_{AC}} = C_{L_W} + C_{L_H} \frac{S_H}{S_W} \quad (2.10)$$

$$C_{D_{AC}} = C_{D_W} + \frac{C_{L_W}^2}{e\pi AR} + C_{D_{tail}} \frac{S_H}{S_W} + C_{D_{other}} \quad (2.11)$$

where $C_{D_{other}}$ represents the drag coefficient from other sections of the aircraft, like the fuselage and tailboom for example. For other sections of the aircraft a typical value of the drag area coefficient of 0.04 was used [31].

Since these two coefficients are calculated for every angle of attack of the wing, the angle of attack that provides coefficients that maximizes endurance, in other words, that maximize ${C_{L_{AC}}}^{3/2}/C_{D_{AC}}$, is chosen. In the end, a verification using Equation 2.12 is done, where it is verified if the corresponding aircraft speed is at least 1.2 times higher than the stall speed to provide a safe speed margin above stall in the presence of air turbulence and gusts which may reduce the aircraft kinetic energy to unsafe values [1].

$$\frac{C_{L_{AC_{max}}}}{C_{L_{AC}}} \geqslant 1.2^2 \quad (2.12)$$

$$C_{L_{AC_{max}}} = 0.9 C_{l_{max}} \quad (2.13)$$

where $C_{L_{AC_{max}}}$ is the stall lift coefficient.

2.2.4 Performance module

This module will be used to create more restrictions, mainly when choosing the airfoil combinations for both wing and tail sections of the aircraft. To have the extra performance metrics it was chosen to calculate the following metrics: takeoff and landing distance, time to climb, best climb rate and fraction of battery used during climb.

For the takeoff distance a simplification [1] given in Equation 2.15 was used, since this is still the concept design, a very accurate approach is not the best option.

$$V_{LO} = 1,2\sqrt{\frac{2gm_{AC}}{\rho_{TO} S_W C_{L_{AC_{max}}}}} \tag{2.14}$$

$$\begin{aligned} s_{TO} = &\left\{ \left[\frac{2C_{L_{AC_{max}}}}{A_1^2} \left(\frac{\frac{P_{propcr}}{\delta_{cr}} \sqrt{\frac{\rho_{TO} C_{L_{AC_{max}}} S_W}{gm_{AC}}}}{gm_{AC} A_1} - \mu_{TO} \right) - C_{D_{AC_{TO}}} \right.\right. \\ &\left.\left. - \mu_{TO} C_{L_{AC_{TO}}} \right] \frac{S_W \rho_{TO}}{2m_{AC}} \right\}^{-1} \end{aligned} \tag{2.15}$$

where V_{LO} is the lift off speed, g is the gravitational acceleration, m_{AC} is the aircraft mass, ρ_{TO} is the air density at takeoff altitude, $P_{prop_{cr}}$ is the propulsive power at cruise, δ_{cr} is the throttle level at cruise, A_1 is a constant with a typical value of 1.2, μ_{TO} the friction coefficient during takeoff wich can drastically change depending on the surface type and condition as well as with the take-off method used, since a lower friction coefficient would imply a smaller take-off distance, a value of 0.05 will be used, $C_{D_{AC_{TO}}}$ the drag coefficient during takeoff and $C_{L_{AC_{TO}}}$ the lift coefficient during takeoff.

Similarly, for the landing distance [1], it was used.

$$s_{LD_{circ}} = \frac{2m_{AC}}{S_W \rho_{LD}} \left(\frac{2\mu_{LD} C_{L_{AC_{max}}}}{A_2^2} + C_{D_{AC_{LD}}} - \mu_{LD} C_{L_{AC_{LD}}} \right)^{-1} + \frac{h_{obs}}{\tan(\gamma)} \tag{2.16}$$

$$s_{LD} = s_{LD_{cir}} - \frac{h_{obs}}{\tan(\gamma)} \tag{2.17}$$

where $s_{LD_{circ}}$ is the total landing distance, ρ_{LD} the air density at landing altitude, μ_{LD} the friction coefficient during landing, $C_{D_{AC_{LD}}}$ the drag coefficient during landing, $C_{L_{AC_{LD}}}$ the lift coefficient during landing, A_2 is a constant with a typical value between 1.15 and 1.30, h_{obs} the obstacle height, γ the approach glide path angle and s_{LD} the landing distance with contact to the ground.

For the climb metrics, the climb is divided into 10 intervals, which the climb rate, climb time and energy consumption are calculated at the ends of the intervals, with the following equations [1]:

$$V_{RC_{partial}} = \sqrt{\frac{2gm_{AC}}{\rho S_W}\sqrt{\frac{K}{3C_{D_{RC_{max}}}}}} \tag{2.18}$$

$$RC_{partial} = \frac{P_{prop_{cr}}/\delta_{cr}}{gm_{AC}} - \frac{\rho V^3_{RC_{partial}} C_{D_{RC_{max}}} S_W}{2gm_{AC}} - \frac{2gKm_{AC}}{\rho V_{RC_{partial}} S_W} \tag{2.19}$$

$$t_{clb_{partial}} = \frac{\Delta h}{RC_{partial}} \tag{2.20}$$

$$E_{clb_{partial}} = P_{elec_{RC_{partial}}} t_{clb_{partial}} \tag{2.21}$$

where $V_{RC_{partial}}$ is the speed for a given altitude step, K is the constant due to the induced drag, $RC_{partial}$ is the rate of climb for a given altitude step, $C_{D_{RC_{max}}}$ is the drag coefficient for the maximum rate of climb, $t_{clb_{partial}}$ is the climb time for a given altitude step, Δh is the altitude step size, $E_{clb_{partial}}$ is the energy used for a given altitude step, $P_{elec_{RC_{partial}}}$ the electric power used for a given altitude step.

2.3 Preliminary design

Moving to the preliminary design, first it is necessary to choose the components that will be part of the aircraft systems. These components include the motor, ESC, MPPT (type and quantity), avionics and control (receiver, autopilot, servo, telemetry, sensors, etc.) and the payload (camera, lens, image processing unit and a transmitter). With the components mass from the previous design phase, it is now possible to have for example the power needed for the motor. Since in the last phase correlations from a large compilation of components was used, it is important to keep in mind that if possible, a better component should be chosen if the right one is not available. For example, a higher motor power with similar mass or a motor with lower mass and similar power output.

With the components of the aircraft fixed, next a propeller database should be created. This database will be important to choose the best propeller size for the selected motor, since the objective is to find the most efficient system possible. The database should include several points of advance ratio and power coefficients for each propeller size.

Before analysing a specific aircraft configuration, it is necessary to also define a better airframe mass model. The airframe mass model from the previous phase while being adequate to have starting values, it only works in a very strict interval of dimensions of the wing. This new airframe mass model can be created by designing a structure with low attention to detail in order to better understand the interval of masses of each part of the structure. For example a wing structure as shown in Figure 2.4, where a general wing structure with skin on frame, two spars and truss ribs is represented, may be used.

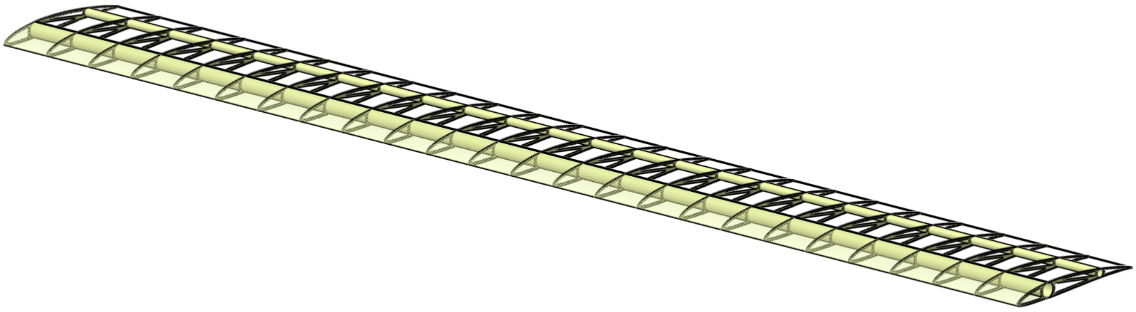

Figure 2.4: Initial wing structure example to calculate correlations between mass and size of each component.

To calculate the mass of structure a first simulation with the conceptual airframe mass model is done, which will allow to have a first value for the aircraft mass. Next the structure, in this case made from composite materials, is analysed and sized for the aircraft loads. This process will allow to calculate the first iteration of the correlations between the structure mass obtained from the structure sizing, and the size of each component, for example the mass of the ribs and the chord of the wing. Next for each iteration of the aircraft, this process should be repeated in order to have better results for the mass and size of the structure, which, in turn, will allow to have a better airframe mass model, since it is constantly being updated. This new model should be more accurate for a larger interval of wingspans and aspect ratios, and it should give some freedom to change the size of the aircraft while iterating it in this design phase. Note that this airframe mass model should be updated with the ongoing project, since it has high impact on the aicraft mass and size. For example, if it is found during the project that the real rib is heavier than the initial estimation due to the loads during flight or if the ribs' quantity should be increased to sustain those loads, one should do the respective corrections on the airframe mass model to increase the reliability of the final design. This process also allows to get the structural concept of the aircraft during the analysis, for example, define the spar and number of ribs, and is highly dependent on the detailed design in Section 2.4. The airframe mass model used is presented later in Section 4.1 (Equations 4.1 to 4.24), since this model can change from project to project, or if other correlations have to be used, for example, due to the structure type. There is also no mathematical model to make the changes needed during the project automatically since those changes can affect several variables, and also depend on the airframe mass model used.

Lastly, before starting the actual sizing, the solar module needs some changes, since in this phase of the project one of the objectives is to verify the viability of the aircraft to perform the mission. So, in this phase, instead of using the average solar energy, the day is divided into small-time steps and the solar energy is calculated for each time step.

Other important aspect should be the understanding of the variation of certain elements on the design, such as the influence of the solar area ratio and the battery specific energy on the total wingspan and mass of the aircraft, since the solar area ratio will influence directly the solar panel area, and the battery specific energy will change the amount of resources on the aircraft to store the energy collected during the day. This will also allow to fix the solar area ratio, and thus reduce the amount of variables during the iterative process for the size of the aircraft. As for the battery specific energy, it will be restricted mainly by the technology used, for example lithium based batteries have higher specific energy density than nickel based batteries as seen in Figure 2.5.

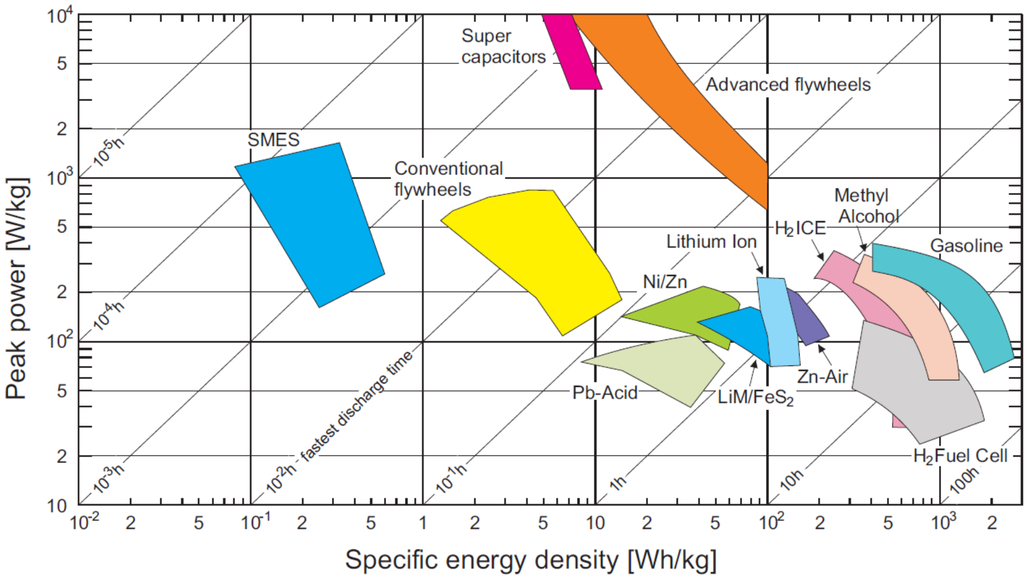

Figure 2.5: The Ragone Plot - Peak power and specific energy density of various energy storage methods [4].

Finally, it is also important to note that while on the conceptual design a weighted average of altitudes were used in case there were two different cruise altitudes during the mission, in this phase, the mission will be analysed phase by phase, meaning that the aircraft will be analysed for each and every phase of the mission. So, it is important to define not only the day and night cruise altitudes, but also the maximum allowable time for the aircraft to climb from night to day cruise altitude, the time for the aircraft to descend from day to night cruise altitude, takeoff and landing altitude and respective times. The time for landing will be more important if a mission with less than 24 hours is analysed, since in that case the aircraft will not need to have enough energy to fly the next day. Also, the tail volume coefficients are obtained differently from the conceptual design, where first it was obtained from similar existing aircraft, now the tail volume coefficients are iterated in conjunction with the stability analysis in order to have the smallest tail possible.

For the analysis process, first the stall speed for day and night cruise altitude is calculated, this will define the lowest possible speed during cruise calculations. Next, the main mission will be divided into four main phases: night cruise, day cruise, climb from night cruise altitude to day cruise altitude and descent from day cruise altitude to night cruise altitude.

Starting from the night cruise altitude phase of the mission, for a given range of velocities the aerodynamic properties, mainly the drag, power required, and incidence of wing and tail section of the aircraft are calculated. These values will enter a propulsion module, where, with the characteristics of the motor and for a given propeller, it will calculate the power usage, throttle and current of the propulsion system. This module will be explained in more detail in Section 2.3.2. Similarly, the properties for the day cruise phase of the mission are calculated, but this time in the aerodynamic module, the incidence of the wing and tail sections are fixed with the values obtained from the night cruise analysis. The reason behind this process is that during the day the aircraft is receiving power from the Sun, while during the nigh the aircraft is only using battery power, so in order to have the less amount of batteries on-board, it was chosen to sacrifice the efficiency of the day flight in order to have the most efficient night flight. Finally, the aircraft properties for the speed that uses less electrical power are chosen as the design points.

Having the cruise phases of the mission calculated, it is followed by the main climb and descent phases. For the climb phase of the mission the best climb rate that will minimize the power consumption is calculated, then it is checked if the time that the aircraft takes to climb between the cruise altitudes is less or equal to the one required by the mission. Since the descent have the time fixed, the power consumption is calculated in order to have the fixed descend rate required by the mission.

With the main mission complete, the next phase is to calculate the mission properties for the first day of flight, that include takeoff, climb to cruise altitude, and start of the mission until the end of the day. For the takeoff phase of the mission the best angle that the aircraft should have in order to minimize the takeoff distance is searched, while the climb to cruise altitude is calculated similarly to the climb during the main mission, but this time without a time constraint.

Finally, the energy balance throughout the day is computed for the starting day and the following 24 hours. This energy balance will help to understand if the aircraft is viable to do the mission, if it is lacking batteries, or solar cells.

The size of the aircraft and number of batteries are iterated for a given aircraft configuration until it is viable for the mission. In the end, this process will output a very detailed report with all geometric properties of the aircraft and all mission properties for all its phases. Like in the conceptual design, other performance metrics are also calculated, for example the top speed at day and night cruise altitudes.

A summary of this process can be found in Figure 2.6.

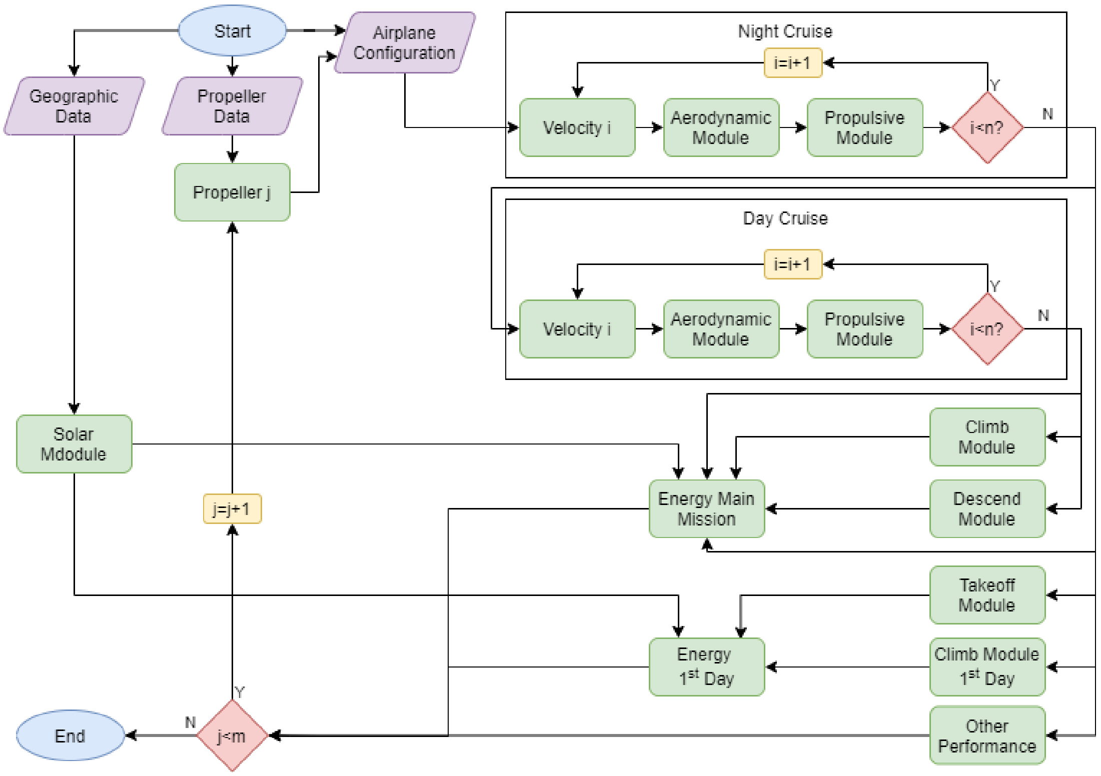
Start
Airplane Configuration
Geographic Data
Propeller Data
Propeller j
Night Cruise
i=i+1
Y
N
Velocity i
Aerodynamic Module
Propulsive Module
i<n?
Day Cruise
i=i+1
Y
N
Velocity i
Aerodynamic Module
Propulsive Module
i<n?
Solar Mdodule
Climb Module
Energy Main Mission
Descend Module
j=j+1
Takeoff Module
Energy 1st Day
Climb Module 1st Day
Y
End
N
j<m
Other Performance

Figure 2.6: Preliminary design flowchart.

2.3.1 Aerodynamic module

Inside this module the objective is to calculate, for a given flight phase, the drag, power requirement and in the case of the night cruise phase of the flight the incidence of the wing and tail of the aircraft. To calculate these aerodynamic characteristics first the Reynolds number of the wing is calculated, then similarly to the conceptual design, the lift coefficient of the wing is calculated using the lifting line method with the polars of the wing airfoil. The drag and pitching moment coefficient of the wing are computed for the respective lift coefficient.

Next in the case of the night cruise, where the incidence of both surfaces is not fixed, the coefficient of lift, drag and pitching moment of the tail is calculated using the same strategy as in the conceptual design. Then the incidence of the wing and tail are computed for the total lift of the aircraft to be equal to the aircraft weight. Finally, the drag and power required are interpolated for the respective lift force acting on the aircraft.

As for the other phases of flight, where the incidence of the wing and tail sections of the aircraft are fixed, the wing aerodynamic coefficients are computed the same way but for the tail aerodynamic coefficients, a correction related to the control surface deflection is needed. First, the tail lift coefficient is calculated, with relation to the wing angle of attack. This will give the base value of the tail lift coefficient, $C_{L_{H_{\text{no ctrl}}}}$, which is calculated assuming no control input and using the lifting line method as before. Next the tail lift coefficient is calculated such as the aircraft is in equilibrium, $C_{L_{H_{\text{equilibrium}}}}$, thus having the real tail lift coefficient needed. Finally, the control surface movement, δ_H of the tail can be calculated with Equation 2.22, since the control surface has to produce the difference in lift coefficient.

$$\delta_H = \frac{C_{L_{H_{equilibrium}}} - C_{L_{H_{no\ ctrl}}}}{\frac{\delta C_{L_H}}{\delta \delta_H}} \quad (2.22)$$

where $\delta C_{L_H}/\delta\delta_H$ is the change in lift coefficient of the tail with the movement of the control surface.

The drag and pitching moment coefficients are computed the same way as before, with relation to the lift coefficient of each part of the aircraft. Finally, the drag, D_{AC}, and power required, P_{req}, are calculated using the drag coefficient of the aircraft and speed by

$$D_{AC} = 0.5\rho V^2 C_{D_{AC}} S_W \quad (2.23)$$

$$P_{req} = D_{AC} V \quad (2.24)$$

where ρ is the air density and V is the velocity. This is one of the most important modules of this phase, since it will be needed inside all the other modules.

2.3.2 Propulsive module

Inside this module, the power usage for a given flight condition is calculated, with the power requirement input from the aerodynamic module. The motor properties for example the maximum voltage, maximum current, speed constant, internal resistance and idling current are also needed. The properties for a given propeller are also used, for example the power coefficient and advance ratio.

In order to calculate the power usage, first it is needed to make sure that the motor and propeller are being calculated for the same requested conditions. For that an iterative process is developed where the current of the motor, I, is iterated by equalizing the power coefficients of the motor, $C_{P_{mot}}$, and propeller, $C_{P_{prop}}$; and the throttle level, f, is iterated by equalizing the power output, P_{prop}, to the power required.

To have the power coefficient of the motor the following equations are used:

$$U = U_{max} f \quad (2.25)$$

$$U_i = U - IR \quad (2.26)$$

$$N = U_i Kv \quad (2.27)$$

$$I_{eff} = I - I_0 \quad (2.28)$$

$$P_{ele} = UI \quad (2.29)$$

$$P_{mot} = U_i I_{eff} \quad (2.30)$$

$$C_{P_{mot}} = \frac{P_{mot}}{\rho D_{prop}^5 (N/60)^3} \quad (2.31)$$

where U_{max} is the maximum voltage of the battery, R is the internal resistance of the motor, U_i is the back electromotive force on the motor, N is the rotational speed of the motor in rpm, I_o is the idle current of the motor, I_{eff} is the effective current of the motor, P_{ele} is the electrical power the motor is consuming and P_{mot} is the shaft power of the motor.

Since the power coefficient can be interpolated with the advance ratio of the propeller, J, the propulsive power can be calculated by Equation 2.38.

$$J_{factor} = 1 - \frac{0.329 S_c}{D_{prop}} \tag{2.32}$$

$$J = J_{factor} \frac{U}{D_{prop}(N/60)} \tag{2.33}$$

$$Re_f = \frac{\rho U l_{fus}}{\mu} \tag{2.34}$$

$$c_f = \frac{0.455}{(log_{10} Re_f)^{2.58} \, (1 + 0.144 \frac{U}{a})^{0.65}} \tag{2.35}$$

$$\eta_f = 1 - 1.558 \rho c_f \frac{S_{wet}}{1.225 D_{prop}^2} \tag{2.36}$$

$$\eta_{eff_{prop}} = \eta_{prop} \eta_f \tag{2.37}$$

$$P_{prop} = P_{mot} \eta_{eff} \tag{2.38}$$

$$\eta_{overall} = \frac{P_{prop}}{P_{ele}} \tag{2.39}$$

where S_c is the cross-section of the fuselage behind the propeller, D_{prop} is the propeller diameter, J_{factor} is a correction factor for the propeller advance ratio, Re_f is the fuselage Reynolds number, l_{fus} is the fuselage lenght, c_f is the friction coefficient, η_f is the correction of the propeller efficiency due to friction forces of the airflow, S_{wet} is the wet area behind the propeller, $\eta_{eff_{prop}}$ is the effective efficiency of the propeller and $\eta_{overall}$ is the overall efficiency of the motor and propeller.

2.3.3 Climb module

With the two major modules explained, it is necessary to calculate the properties for other phases of flight. In this module, the objective is to calculate the power usage during the climb. Note that there are two phases during the mission where this occurs, from the night cruise altitude to the day cruise altitude, and from the takeoff altitude to one of the cruise altitudes, depending on the takeoff time. The difference between these two phases besides the altitude difference, is that from the night cruise altitude to the day cruise altitude, the allowable time is restricted by the mission, as requested by FEUP.

First, the altitude difference is split into 10 altitude steps. Then for each ends of each step the best climb rate is calculated with Equation 2.40, where the power values come from the aerodynamic and propulsive calculations for each altitude step. With the power of the motor from the propulsive module, it is now possible to calculate the energy using Equation 2.21. Where the total energy and total time used will be the sum of the energies from each altitude step.

$$RC_{partial} = \frac{P_{prop} - P_{req}}{g m_{AC}} \quad (2.40)$$

where $RC_{partial}$ is the climb rate for a given altitude step, P_{req} is the required power.

Finally, the total climb time is cross-checked with the mission requirements. If the time exceeds the required time, an increase of the throttle level is required, if the throttle can not be increased a more powerful propulsion system is required. This throttle level and time to climb values can be adjusted to better fit the battery size. This adjustment can be done since for a faster climb would require more power but less overall energy, since a faster climb would make the aircraft stay at day cruise altitude longer (because it uses less power than the climb phase), but it also creates the need for more batteries since the solar energy during climb phase is negligible (very small when compared with the energy used), meaning that the aircraft is using only the battery energy during this phase.

2.3.4 Descent module

Similarly, to what is done for the climb, the objective is to calculate the energy used during this phase of the flight. Again, there are two different phases during flight where the aircraft performs a descent. First from the day to night cruise altitude, and the second from the cruise altitude to the landing altitude. In this case, in both scenarios the time to complete the descent is fixed, as requested by FEUP, so the calculations and verifications are the same for both situations.

First the descend rate is calculated, since the initial and final altitudes are fixed, and the time to complete the descent is also fixed. Next similarly to the climb module the altitude range is divided into 10 altitude steps. The difference between this module and the previous one is that while for the climb a throttle-controlled climb was done, here a constant equivalent speed descent will be done. Next, a range of equivalent speeds are given.

Given that the descent rate is fixed, due to the constraint in altitude and time, for every altitude step and equivalent velocity the propulsion and aerodynamic properties are calculated. Since the descent rate is fixed, the angle of attack of the aircraft can be calculated, and thus the power required can be found through the aerodynamic module. Since the descent rate can be calculated the same way as the climb rate in Equation 2.40, the power required from the propulsion system can be found, and thus the propulsive properties can be calculated with the propulsive module. Having calculated the energy used for every combination of altitude step and equivalent velocity step, the equivalent velocity that meets the time constraint of the mission requirements is chosen.

2.3.5 Take-off module

Inside this module, not only will the energy used during takeoff be calculated, but also the best angle the aircraft should have to take off in the shortest distance.

To be able to calculate such properties, the lift off speed with Equation 2.14 is calculated first. Then the range of speed from zero to the lift off speed is divided into 20 speed steps. In addition, an interval set of angles is also provided. Next, for each combination of speed and angle step, the aerodynamic properties are computed, together with the propulsion system properties with a throttle level equal to 1. The rolling drag force, F, during takeoff is also calculated using Equation 2.41. This will allow to calculate the acceleration, $a_{TO_{partial}}$, of the aircraft with Equation 2.42. Thus, with the speed step and acceleration, it is possible to calculate the time the aircraft takes on each speed step, $t_{TO_{partial}}$, and travel distance, $s_{TO_{partial}}$, with equations 2.43 and 2.44.

$$F = \mu_{TO}\left[g m_{TO} - L_{AC}\right] \tag{2.41}$$

$$a_{TO_{partial}} = \frac{T - D_{AC} - F}{m_{TO}} \tag{2.42}$$

$$t_{TO_{partial}} = \frac{V}{a_{TO_{partial}}} \tag{2.43}$$

$$s_{TO_{partial}} = V t_{TO_{partial}} \tag{2.44}$$

where m_{TO} is the total takeoff mass (it can be different from the mass during the mission if a takeoff trolley is used, for example) and V the speed step in use.

Next, the time, travel distance and energy used from every velocity step, for a given angle step are summed. Finally, the angle that minimizes the takeoff distance is chosen.

2.3.6 Other performance metrics

This final module calculates several extra performance metrics about the aircraft. These metrics include: top speed at day cruise altitude, top speed at night cruise altitude and landing distance. As for the top speed during day and night cruise altitude, the process consists in iterating the speed of the aircraft with the aerodynamic and propulsive module in such a way that the power required from the aerodynamic module equals the power output with maximum throttle from the propulsive module. The landing distance is calculated using the same method as the one used in the conceptual design.

2.4 Detailed design

In this last phase of the design the objective will be to test the design, design the details that were not considered in the past design phases, for example connections between parts, and to develop the fabrication and assembly process for each part of the aircraft.

As for the testing of the design, since the aircraft is electrically powered, there are three major tests to perform: avionics test, where systems like the communications and integration between components are verified; systems test, where all components inside the aircraft should be tested together in the way that the masses, efficiencies and energy consumption are verified alongside compatibility between components; and lastly structural tests, where critical elements from the structure of the aircraft should be at least tested virtually or, if possible, physically to assess the real strength and mass of the elements of the structure, meaning that during these tests the sizing of the structure will be done together with the update of the airframe mass model. The last test area is of great importance since it will influence directly the airframe mass, and thus the total mass of the aircraft. This real-world structural tests can include for example stress tests on the rib of the wing, while the virtual ones can include for example the spar of the wing. Ideally all the structure should be tested in order to understand the true limit of the aircraft, but that would not only require a lot of resources but also increase by a large margin the cost of the project. It is also important to refer to the construction and design of a prototype before a full-scale version is developed, since with a prototype it will be possible to test not only the electronic components during flight but also the design concepts. For the fabrication and assembly process of the parts, it should be thought in the simplest way possible with the available materials.

It is important to note that this design phase can drastically change the design from the preliminary design, since the mass of components or even the structure that was thought to be feasible can change, mainly because the sizing of the structure is only done in the detailed design. With this change, the preliminary design should be corrected in order to have a new aircraft design. One way around this problem is to make these tests in conjunction with the preliminary design. This will allow to make the changes earlier, thus being able to update the airframe mass model to more correct correlations of mass and size of each element, and possibly converge to a better solution faster.

Chapter 3

Conceptual design

In this chapter, the conceptual design process for a solar UAV to monitor wildlife for large periods of time will be presented.

3.1 Mission requirements

As it was said before, first it is needed to fix the main mission requirements, which are given by restrictions of FEUP project. For some of this requirements, for example, the cruise altitudes, the terrain altitude where animals typically are found and surronding mountains in Nepal were taken into account so the aircraft could fly safely. The requirements shown in the following list are for the full-sized aircraft (for theoretical perpetual flight).

- Day cruise altitude of 3000 m;
- Night cruise altitude of 500 m;
- Takeoff and landing altitude of 100 m;
- Takeoff with a detachable trolley;
- Perform belly landing;
- Must be capable of monitoring wildlife during day and night time;
- Descent time from day cruise altitude to night cruise altitude of 8 hours;
- Climb time from night cruise altitude to day cruise altitude no longer than 2.5 hours;
- Fly any time of the year at 30° N (preferebly in Nepal);
- Must use SunPower E60 or C60 solar cells;
- Must use MaxAmp batteries;

- Must be as small as possible.

In order to have small initial budget needs, first a smaller prototype for concept validation would be designed, where several systems and part of the mission will be tested. This prototype will only fly for less than a day, but it carries all the payload, avionics and control systems used for the full-sized aircraft. The prototype will takeoff 1 hour before Sunrise and land 3 hours after Sunset, giving a flight time endurance between 14 and 18 hours throughout the year.

3.2 Payload

The objective of the aircraft is to monitor wildlife during day and night. To achieve that, an optical camera to work during the day and a thermal camera during the night were chosen.

From tests, on previous works, where photographs have been taken from various distances, it was determined that the image from the camera should have no less than 100 pixels per square meter on the ground in order to distinguish objects or animals. In conjunction with FEUP, the Raspberry Pi HQ camera, with 12,330,240 pixels (4056 x 3040) with an Arducam 35 mm lens and 8^o of field of view (FoV), that according to the datasheet have an effective covering area of 0.14 m x 0.10 m at 1 m distance, would have 126,000 m^2 (420 m x 300 m) of covering area at cruise altitude (3000 m) during day, giving a pixel density of 97.9 pixels per square meter, for day monitoring. Despite being 2.1% lower than the target density, it was decided together with FEUP to use it since it should still be good for testing purposes of the prototype. As for the thermal camera for night monitoring, it was fixed by FEUP to be a FLIR Boson with a 36 mm lens and 12^o of FoV. This camera have 327,680 pixels (640 x 512), and with the respective FoV it should cover 8,837 m_2 (105 m x 84 m), despite the pixel density of 37.1 pixels per square meter, which is less 62.9% than the target pixel density. To control both cameras a RaspberryPi 4 was chosen since it has a low power consumption and can transmit the images via Wi-Fi in real time. The payload has a total of 0.4 kg and should not use more than 27 W of power at any time. These components can be seen in Figure 3.1.

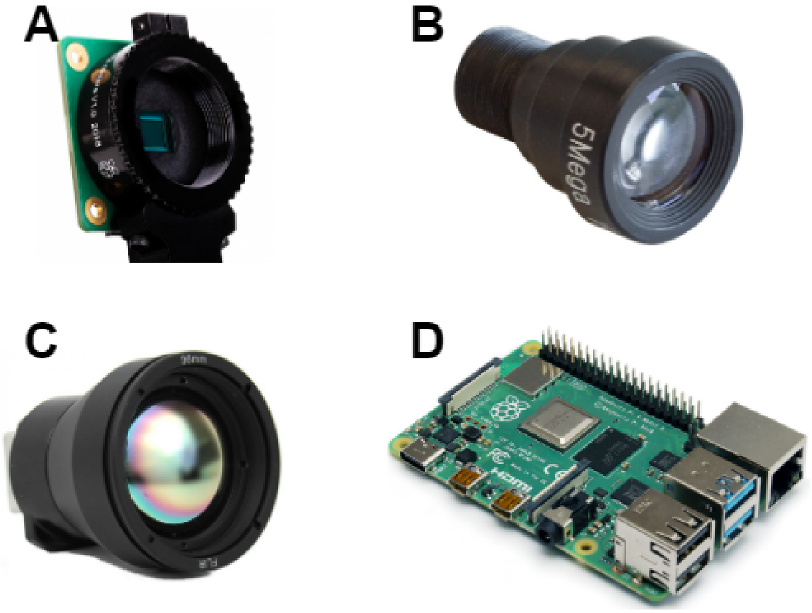

Figure 3.1: Payload components. A - Raspberry Pi HQ camera [32]; B - Arducam 35 mm lens [33]; C - FLIR Boson [34]; D - Raspberry Pi 4 [35].

3.3 Data and airfoils

In this section the database collected for the motor, ESC, MPPT and batteries from MaxAmp brand will be presented.

From a total of 2045 motors from brands such as Hacker, Plettenberg, Xoar, Maxon, ePropeller, Portscap, Badasspower, AXI and Scorpion; 34 ESC from Badasspower and Hacker; 12 MPPT from Genasun and MG Eletronics; and 29 batteries from MaxAmp, the following correlations were calculated:

$$m_{mot} = 0.0002248 P_{mot}, \qquad R^2 = 0.831 \tag{3.1}$$

$$m_{ESC} = 0.0000568 P_{ESC}, \qquad R^2 = 0.967 \tag{3.2}$$

$$m_{MPPT} = 0.0006128 P_{MPPT}, \qquad R^2 = 0.868 \tag{3.3}$$

$$m_{bat} = 0.0054498 E_{bat}, \qquad R^2 = 0.991 \tag{3.4}$$

$$m_{SC} = 0.448 A_{SC} \tag{3.5}$$

where m_{mot} is the motor mass, P_{mot} is the motor power, m_{ESC} is the ESC mass, P_{ESC} is the ESC power, m_{MPPT} is the MPPT mass, P_{MPPT} is the MPPT power, m_{bat} is the battery mass, E_{bat} is the battery energy, m_{SC} is the solar cells mass and A_{SC} is the solar cells area. As for the solar cells, since they are fixed to be SunPower E60 or C60, the values from the datasheets were used. The graphs for the components correlations can be seen in appendix A.3.

Next, it is necessary to create a database of aircraft with similar missions. But first it is required to have a general geometry of the aircraft, since even for similar missions very different aircraft can be found. Having *Zephyr S* as a reference, since it holds the current endurance record, a single pull propeller arrangement was selected since it increases the overall propulsion efficiency. A rectangular wing and a V shaped tail were adopted. The wing is rectangular because of its sizing and fabrication inherent simplicity owing to its constant cross-section geometry. The V-tail, also with constant chord, is better when compared with a conventional tail (inverted T) since the number of parts and mass are lower [36], and because they produce less interference drag. It also allows for ground clearance when landing. These two elements of the aircraft would use a skin on frame, with a transparent film acting as skin. Since the film is transparent, the impact on the solar panels' efficiency is low [28] in case the top part of the wing needs to be covered with film. This type of structure is also known to be lighter than a monocoque type of structure. Keeping this kind of layout of the aircraft and the type of mission, from 109 aircraft compiled (Appendix A.1), only 58 aircraft were used to compute the correlation between airframe mass, m_{af}, wingspan, b, and aspect ratio, AR, that can be shown in Equation 3.6 and Figure 3.2.

$$m_{af} = 0.10717 b^{1.81031} AR^{-3.164e-7} \quad (3.6)$$

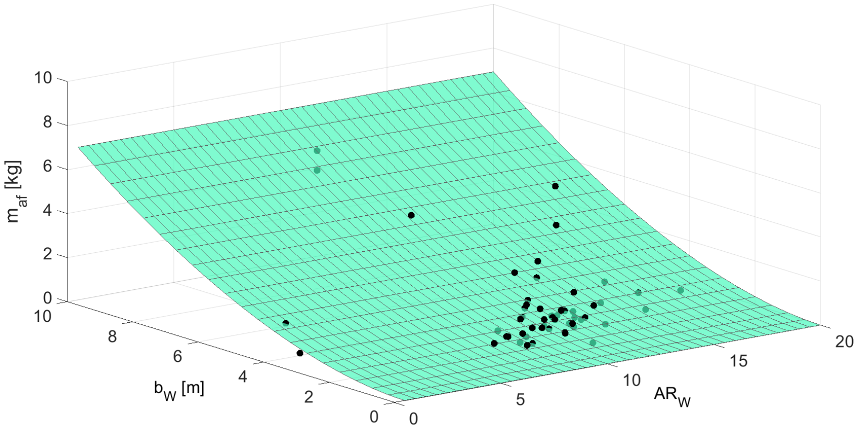

Figure 3.2: Aircraft used to compute the correlation between airframe mass, wingspan and aspect ratio, and respective correlation plane.

It is important to note that the majority of aircraft have very low wingspan because most of aircraft that exist with similar layout are still prototypes, so the number of solar aircraft with large wingspan is very small. This large concentration of small aircraft will create a problem when a large aircraft is needed, since this airframe mass equation has a very small interval of validity.

Lastly, for the wing and tail sections of the airplane, a total of 71 airfoils for the wing section and 75 airfoils for the tail section of the aircraft were compiled.

3.4 Conceptual analysis

With the data gathered so far, it is possible to start testing different aircraft combinations of wingspan, aspect ratio and airfoils for the wing and tail sections of the aircraft. Since the aircraft should fly throughout the year at a latitude of 30° N, the tests will be performed for winter solstice since it is the day with less average specific Sun energy, as it can be seen in figures 3.3 and 3.4, where the maximum Sun irradiance was assumed to be 1100 W/m^2.

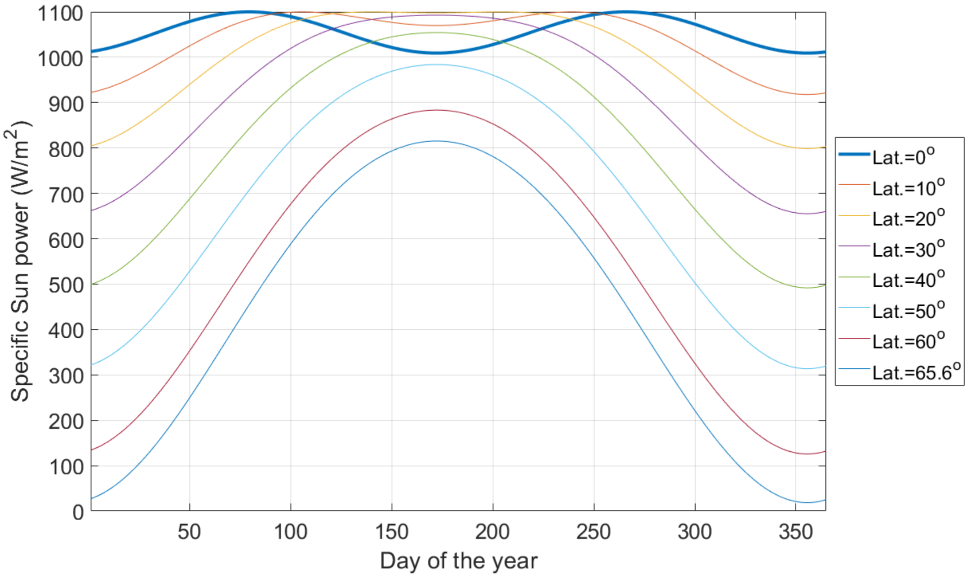

Figure 3.3: Peak specific Sun power for one complete year and different latitudes.

Next a range of wingspans between 10 m and 15 m, and a range of aspect ratios between 10 and 20 were adopted. The analysis on this phase was divided into two main steps to select the wing and tail airfoils without analysing all possible combinations, since from 71 airfoils for the wing and 75 airfoils for the tail would generate a maximum of 5325 combinations. The process used will only use 5 airfoils for the wing on the first step and 5 tail airfoils for the second step, only giving a total of 730 possible combinations, highly

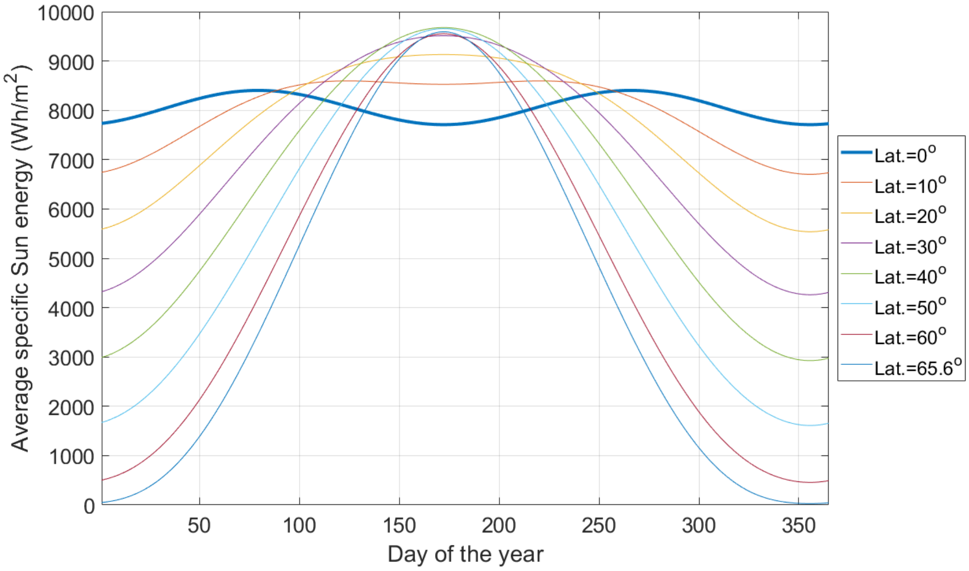

Figure 3.4: Average specific Sun energy for one complete year and different latitudes.

reducing computation time.

In the first step, five airfoils for the wing that had the best $C_l^{3/2}/C_d$ for a Reynolds number of 400,000 [37], were chosen. It is important to note that the Reynolds value used will not interfere with the final results since it is only used to chose the five starting airfoils. Starting with the following airfoils for the wing:

- DAE-51;
- NACA 63-412;
- SD7032-099-88;
- USA35bModified;
- WE3.55-9.3.

and with all possible airfoils for the tail section of the aircraft.

The best 5 airfoils for the tail section of the aircraft were selected based on the following criteria in order:

- Minimum total aircraft mass;
- More than one viable aircraft;
- Minimum required power;

- Reduced amount of noise in the results (since the aerodynamic coefficients are interpolated from the airfoils aerodynamic coefficient curves, a large amount of noise in the data may indicate numerous non-converged points in the polars).

The best tail airfoils found were:

- A18 inverted;
- E193 inverted;
- HS ACC2021 inverted;
- S4110 inverted;
- WE3.55-9.3 inverted.

In order to choose the best wing airfoil, a similar approach was used, where all 5 best tail airfoils together with the 71 wing airfoils were analysed. Together with the same criteria used before the airfoil thickness was also verified, since a thinner airfoil will result in a heavier wing for a given wing bending moment; and the airfoil camber, since the wing will use a skin on frame structure, a larger camber would make the adhesion of the film onto the ribs more difficult.

Having applied these criteria to the airfoils' selection, it was found that the smallest prototype aircraft has the characteristics shown in Table 3.1. The current method benefits higher aspect ratios, which is also mentioned in Noth work [4]. The final solutions and airfoils can be seen in Figure 3.5, 3.6 and 3.7, respectively.

Table 3.1: Conceptual analysis results.

Parameter	Value	Unit
Wing airfoil	WE3.55-9.3	-
Tail airfoil	E193 inverted	-
Wing span	10.1	m
Total mass	26.5	kg
Aspect ratio	16	-
Equivalent vertical tail volume coefficient	0.03	-
Equivalent horizontal tail volume coefficient	0.70	-
Distance between the aerodynamic center of the wing and tail	3.4	m

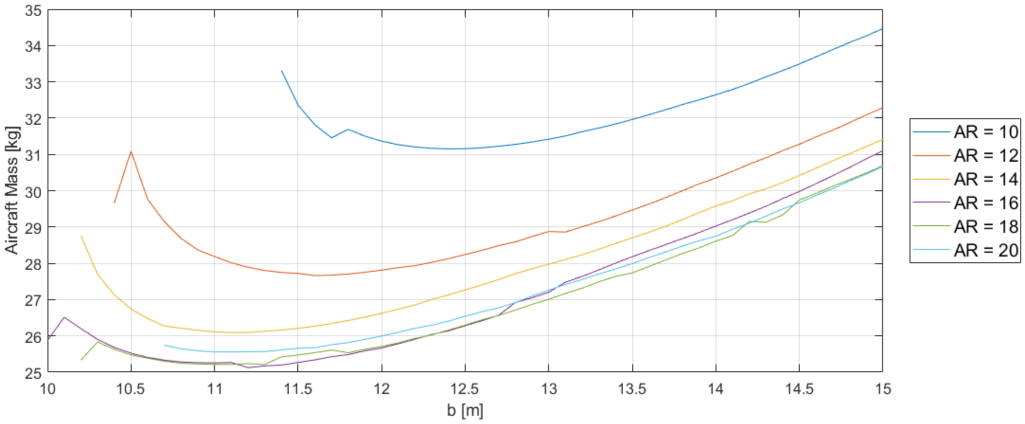

Figure 3.5: Total mass of the aircraft for several wingspan and aspect ratio values.

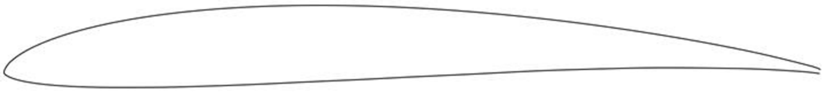

Figure 3.6: Wing airfoil, WE3.55-9.3.

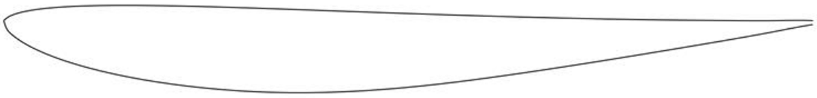

Figure 3.7: Tail airfoil, E193 inverted.

Chapter 4

Preliminary and detailed design

Inside this chapter, both preliminary design of the prototype aircraft (Section 4.2) and the detailed design of the wing will be presented. These two design phases were joined together in one single chapter since they are highly dependent of each other. In the end, the preliminary design for a final aircraft for perpetual flight will also be presented (Section 4.3).

4.1 Parametric studies

Before starting to choose the most appropriate components for the prototype aircraft, first it is needed to do some parametric studies to verify the influence of some variables on the design of the aircraft.

For that, a set of components were chosen for an aircraft capable of performing the complete mission. Next, it was chosen to test the influence of the solar area ratio and the battery specific energy on the wingspan and total mass of the aircraft. The results of such study can be seen in Figure 4.1.

From Figure 4.1 it is possible to see that both wingspan and total aircraft mass decrease with the increase of the solar area ratio and the battery specific energy. Since the aircraft should be as small as possible, a solar area ratio of 0.9 was chosen. The remaining 10% of the wing area cannot be covered with solar cells in order to account for spacing for aileron hinges and for the leading edge excessive curvature area. As for the battery specific energy, the restriction is given by the mission requirements by fixing the battery brand, where a 180 Wh/kg battery is used.

Other studies were made where the change in wingspan and total aircraft mass in function of day of the year, latitude, airframe mass and altitude during night cruise were analysed. The result of such study can be found in Figure 4.2.

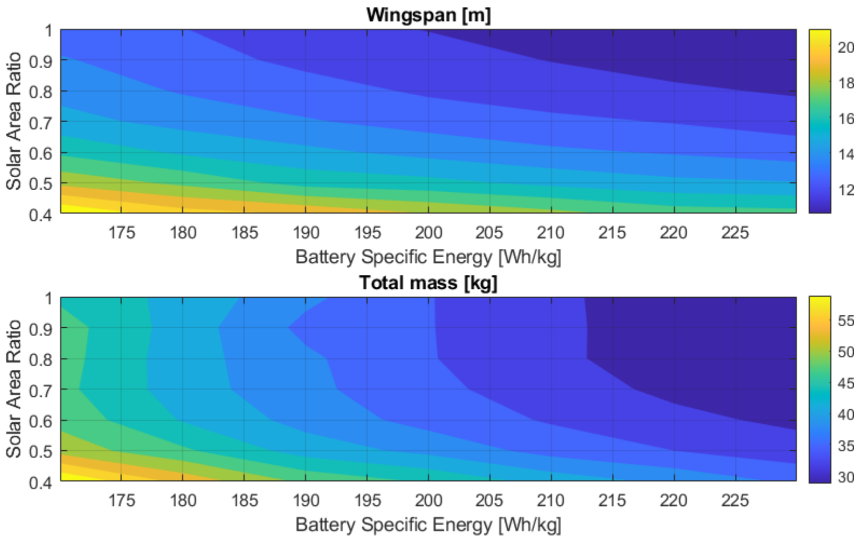

Figure 4.1: Wingspan and total aircraft mass as functions of solar panel area ratio and battery specific energy.

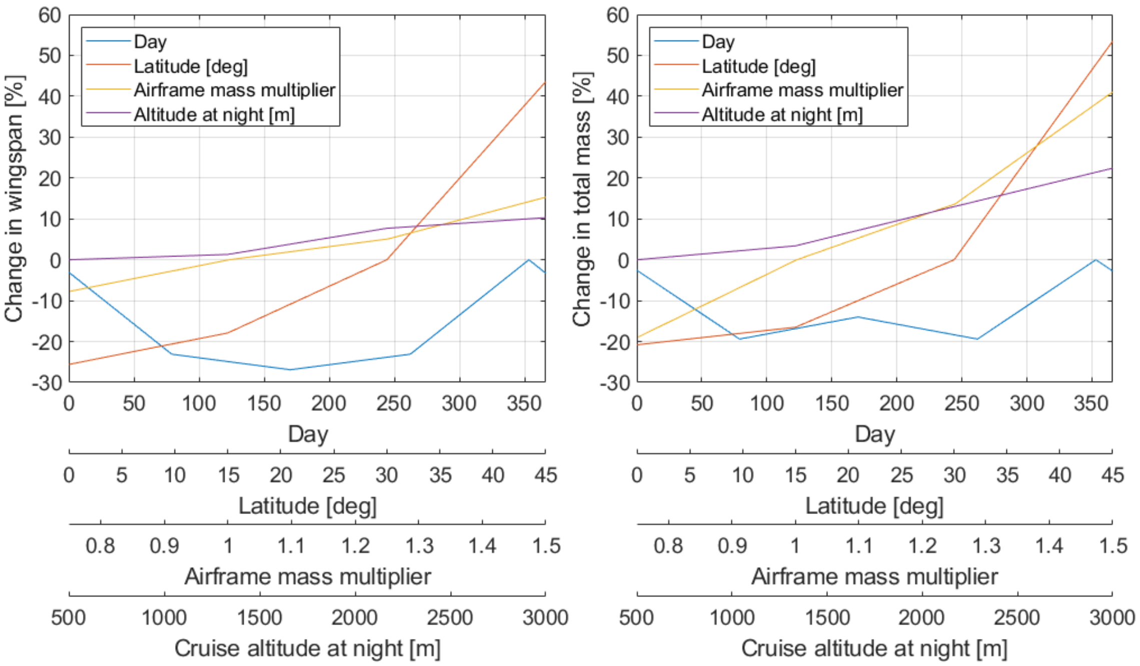

Figure 4.2: Percent change in wingspan (left), and in total aircraft mass (right), with day, latitude, airframe mass and altitude at night during cruise.

As it can be seen, the day of the year and the latitude of the mission have the most impact on the wingspan and total aircraft mass, while the airframe mass and the night cruise altitude mostly impacts the total mass.

Other factors to take into account are the battery cell configuration, propeller configuration and the correction of the mass model. As for the battery cell configuration, a lower maximum voltage is more suitable since it will allow to rotate the propeller slower and thus increase the propulsion system efficiency, but on the other hand it will increase the current that will be fed to the systems. A 6S battery was chosen to give a nominal voltage output of 22.2 V, which offers a good compromise between low maximum voltage for the motor, and high enough voltage to have fewer losses through Joule effect on other systems. In order to increase the propulsion group efficiency, a high diameter and a low propeller blade count together with a low speed constant motor should be used.

Finally, to use a more correct airframe mass model, an initial structure was made with low attention to detail, with a wing and tail structure similar to the one shown in Figure 2.4, and a monocoque fuselage and tubular tailboom. The structure was initially assumed to be all built with composite materials, due to its high specific strength. This new model should have a larger validity interval, but it should be updated throughout the design process. For the final airframe mass model it was defined that the distance between ribs for the wing and tail sections of the aircraft, $l_{ribs_{wing}}$ and $l_{ribs_{wing}}$, respectively, would be 0.126 m and 0.100 m (where the distance between ribs for the wing will be explained later in Section 4.2.5.2). Next the wing mass could be calculated by:

$$A_{rib_{wing}} = 0.032c_W^2 + 0.0146c_W \tag{4.1}$$

$$m_{rib_{wing}} = 0.444A_{rib_{wing}}\left(\frac{b}{l_{rib_{wing}}} + 1\right) \tag{4.2}$$

$$A_{spar_{wing}} = 0.351b \tag{4.3}$$

$$m_{spar_{wing}} = 0.775A_{spar_{wing}} \tag{4.4}$$

$$A_{LE_{wing}} = 0.56052c_W b \tag{4.5}$$

$$m_{LE_{wing}} = 0.087A_{LE_{wing}} \tag{4.6}$$

$$A_{skin_{wing}} = 2.028c_W b \tag{4.7}$$

$$m_{skin_{wing}} = 0.096A_{skin_{wing}} \tag{4.8}$$

$$m_{TE_{wing}} = 0.07b \tag{4.9}$$

$$m_{wing} = m_{rib_{wing}} + m_{spar_{wing}} + m_{LE_{wing}} + m_{skin_{wing}} + m_{TE_{wing}} \tag{4.10}$$

where $A_{rib_{wing}}$ is the surface area of one rib, $m_{rib_{wing}}$ is the total ribs mass of the wing, $A_{spar_{wing}}$ is the surface area of wing spar, $m_{spar_{wing}}$ is the total wing spar mass, $A_{LE_{wing}}$ is the surface area of the wing leading edge, $m_{LE_{wing}}$ is the total wing leading edge mass, $A_{skin_{wing}}$ is the skin area covering the wing, $m_{skin_{wing}}$ is the total wing skin mass, $m_{TE_{wing}}$ is the trailing edge sheet mass and m_{wing} is the total wing mass.

Similarly the tail mass could be calculated as

$$A_{rib_{tail}} = 0.0384c_{tail}^2 + 0.0146c_{tail} \tag{4.11}$$

$$m_{rib_{tail}} = 0.444A_{rib_{tail}}\left(\frac{b_{tail}}{l_{rib_{tail}}} + 2\right) \tag{4.12}$$

$$A_{spar_{tail}} = 0.195b_{tail} \tag{4.13}$$

$$m_{spar_{tail}} = 0.444A_{spar_{tail}} \tag{4.14}$$

$$A_{LE_{tail}} = 0.56052c_{tail}b_{tail} \tag{4.15}$$

$$m_{LE_{tail}} = 0.087A_{LE_{tail}} \tag{4.16}$$

$$A_{skin_{tail}} = 2.028c_{tail}b_{tail} \tag{4.17}$$

$$m_{skin_{tail}} = 0.096A_{skin_{tail}} \tag{4.18}$$

$$m_{TE_{tail}} = 0.07b_tail \tag{4.19}$$

$$m_{tail} = m_{rib_{tail}} + m_{spar_{tail}} + m_{LE_{tail}} + m_{skin_{tail}} + m_{TE_{tail}} \tag{4.20}$$

where $A_{rib_{tail}}$ is the surface area of one rib, $m_{rib_{tail}}$ is the total ribs mass of the tail, $A_{spar_{tail}}$ is the surface area of tail spar, $m_{spar_{tail}}$ is the total tail spar mass, $A_{LE_{tail}}$ is the surface area of the tail leading edge, $m_{LE_{tail}}$ is the total tail leading edge mass, $A_{skin_{tail}}$ is the skin area covering the tail, $m_{skin_{tail}}$ is the total tail skin mass, $m_{TE_{tail}}$ is the trailing edge sheet mass and m_{tail} is the total tail mass.

The tailboom and fuselage masses are calculated with

$$A_{tailboom} = 0.223\frac{b^2}{l_{tail}} \tag{4.21}$$

$$m_{tailboom} = 1.1094A_{tailboom} \tag{4.22}$$

$$m_{fuselage} = 0.554 \tag{4.23}$$

where $A_{tailboom}$ is skin area of the tailboom, l_{tail} is the distance between the leading edge of the wing and the leading edge of the tail, $m_{tailboom}$ is the tailboom mass and $m_{fuselage}$ is the fuselage mass.

The total airframe mass is calculated as

$$m_{af} = f_{strut}\left(m_{wing} + m_{tail} + m_{tailboom} + m_{fuselage}\right) \tag{4.24}$$

where f_{strut} is a safety factor of 1.5, to account for extra mass from the ailerons and connectors for example.

4.2 Prototype aircraft

Before starting with the preliminary design of the prototype aircraft, first it is needed to define extra mission requirements, since this aircraft will fly for less than a full day. The prototype aircraft should take off 1 hour before Sunrise, start the descent to land at Sunset and land 3 hours after Sunset.

After some tests, it was verified that this aircraft should be adaptive to the time of the year by using wing extensions. This would allow to have an optimal aircraft to fly during the summer and winter days. To make this possible, first the design is focused on the winter aircraft, where the conditions are more critical due to the lower Sun energy available. Next, with the geometry obtained from the winter aircraft, the wingspan and consequently the solar cells' area are reduced while the battery count is increased.

4.2.1 Components selection

The selection of components is not easy, and it requires an iterative process. Since the conceptual design is done for perpetual flight, the components given at that time can be oversized in some aspects.

4.2.1.1 Propulsion group

For the propulsion group, that includes the propeller, motor and ESC, a 20 in x 10 in two bladed folding propeller; a Hacker A50-16 L V4 motor with a speed constant of 265 rpm/V, 0.445 kg of mass, an internal resistance of 31 mΩ, capable of 1650 W and an idle current of 1 A; and an 85 A Mezon Pro 85 ESC with 0.081 kg of mass, as seen in Figure 4.3, were chosen. The choise of these components were made throughout an iterative process where several combinations of components were analysed with the objective of minimizing energy consumption throughout the mission and thus allow for a smaller aircraft.

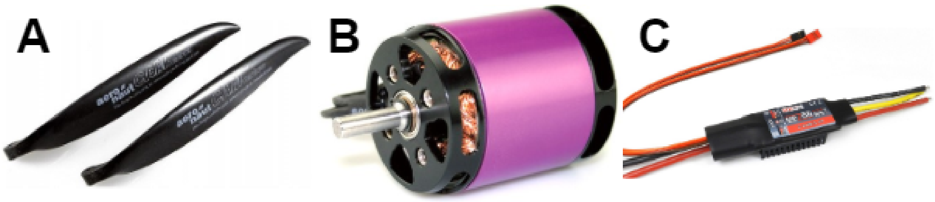

Figure 4.3: Propulsion components for the prototype aircraft. A - 20 in x 10 in propeller [38]; B - Hacker A50-16 L V4 motor [39]; C - Mezon Pro 85 ESC [40].

4.2.1.2 Electronics group

This group includes the batteries, MPPT, solar cells, and the BMS. As for the batteries, it was found that the winter aircraft would need 3 MaxAmp batteries in parallel, each one with a 6S configuration and 11 Ah of capacity, while the summer aircraft would need 5 of the same batteries in parallel. For the MPPT, 3 Genasun GVB-8 capable of receiving a total of 630 W from the solar cells should be used. All these components can be seen in Figure 4.4. For the BMS, it was chosen to build a custom BMS in order to better fit the aircraft needs. The solar cells are fixed from the mission requirements to be SunPower E60 or C60, which have an efficiency between 21 and 22%, the winter aircraft would need 216 solar cells, using 3.37 m^2 of wing area, including encapsulation space of 1 mm between cells, while the summer aircraft would need 168 solar cells, using 2.62 m^2 of wing area, including encapsulation space of 1 mm between cells, producing a peak power of 440 W and 571 W, during the winter and solar solstice, respectively. The quantity of solar cells was obtained from the analysis of the prototypes in Section 4.2.2 and 4.2.3, respectively.

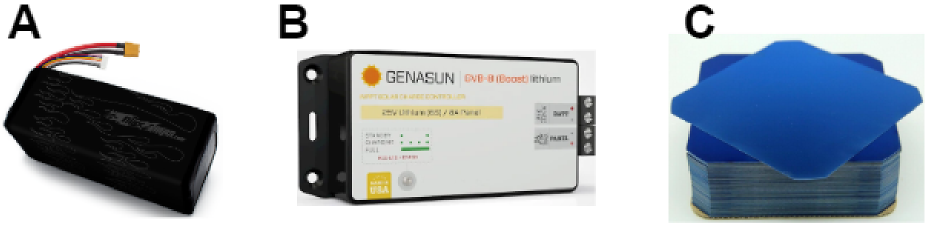

Figure 4.4: Energy components for the prototype aircraft. A - MaxAmp battery with 11 Ah capacity [41]; B - Genasun GVB-8 MPPT [42]; C - Stack of Sunpower C60 solar cells [43].

4.2.1.3 Avionics and control group

For this group it is possible to find the communication, control and telemetry modules, as seen in Figure 4.5. For the communications with the ground station, a long range

Dragonlink will be used. Next for the control systems, a Pixhawk4 for the autopilot and 6 Corona CS-939MG servos, 2 on each side of the wing, and 2 for the control surfaces of the tail are used. A GPS device and an airspeed sensor are also used. It also include cables for connections and additional telemetry sensors mass and power requested to be included by FEUP. The complete avionics and control group can be seen in Table 4.1. This group should not be heavier than 3.5 kg and use no more than 29 W of power. It is important to note that these values area calculated for the worst case scenario where the components are using its maximum power.

Table 4.1: Avionics and control components mass and power.

Component	Mass [kg]	Power [W]
Dragonlink	0.012	1.00
Pixhawk power board	0.036	1.00
Pixhawk 4	0.180	2.50
GPS	0.070	0.20
Airspeed sensor	0.020	0.02
Servos	0.600	16.00
Additional telemetry	0.600	8.30
Cables	2	-

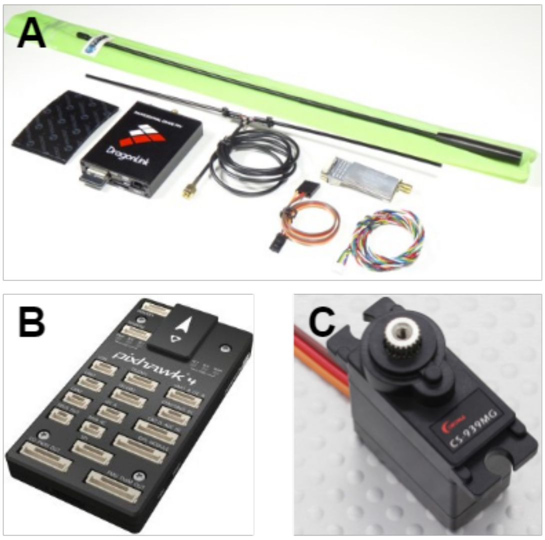

Figure 4.5: Avionics and control components. A - Dragonlink setup components [44]; B - Pixhawk 4 [45]; C - Corona CS-939MG servo [46].

4.2.2 Winter aircraft analysis

Starting from the winter aircraft, after an iterative process, it would have the characteristics found in Table 4.2. The value of the chord is calculated such as an integer number of solar cells, in this case 4, are used representing 90% of the chord. Despite having a high chord value, due to the solar cell size, it was necessary since a smaller chord would mean a larger difference in wingspan from the winter and summer aircraft. The detail drawings for this aircraft can be seen in appendix A.6, and a representation of the winter aircraft can be seen in Figure 4.6.

Table 4.2: Winter prototype aircraft characteristics.

Parameter	**Value**	**Unit**
Wing span	6.81	m
Chord	0.55	m
Distance between aerodynamic center of the wing and tail	2.175	m
Total mass	19.091	kg
Battery mass (ratio of total mass)	3.886 (20)	kg (%)
Structure mass (ratio of total mass)	7.355 (39)	kg (%)
Tail angle with horizontal plane	44	degrees
Tail span	1.4	m
Tail chord	0.25	m
Wing incidence	1.5	degrees
Tail incidence	-1.5	degrees

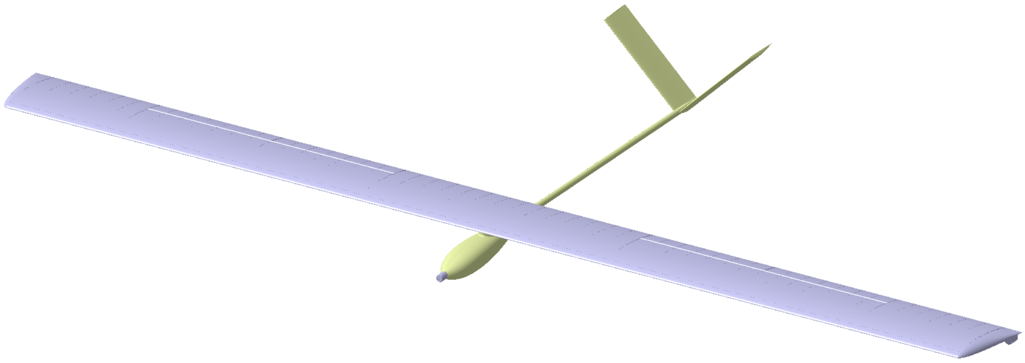

Figure 4.6: General representation of the winter aircraft.

Regarding the energy balance throughout the mission, it can be seen in Figure 4.7. The figure is composed by 5 graphs. The first shows the energy inside the battery pack, the second shows the energy that is reaching the batteries from the solar cells, the third and fourth graph shows the power usage by the aircraft and the power flux of the battery, respectively, while the fifth shows the solar energy being harvested but not used, meaning that the harvested solar energy is only totally used where the graph is at 0 W. It is important to note that in the first graph 0 Wh is measured relative to 20% of the battery capacity, since using more energy can damage the battery.

Some important points on the graph to note are: the takeoff point, where a power spike on the power usage can be observed, the first minimum of energy inside the battery, which represents the point where the Sun energy in enough to sustain cruise flight, the area with excess power collected from the Sun, which represents when the batteries are full and there is enough Sun energy to sustain the mission, and the end of the mission

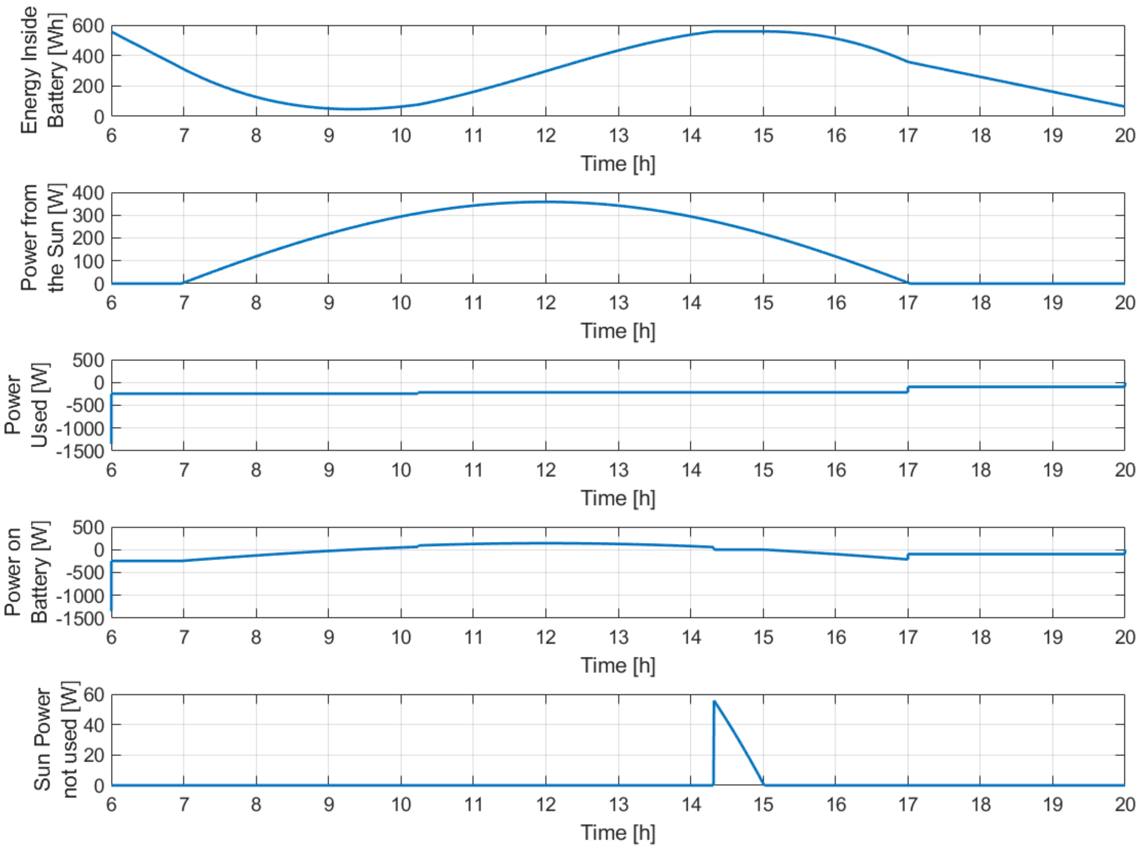

Figure 4.7: Energy and power graphs for the winter aircraft mission.

which has an energy similar to the first energy minimum. The throttle from takeoff to cruise altitude should be adjusted in order for the 2 energy minimums to coincide, since a lower first minimum means that the aircraft could actually fly more time, while a second lower minimum means that the climb could be done faster. Since the amount of batteries and solar cells has to be discrete, it was expected to have some excess power from the solar cells, as seen in the fifth graph. This excess power can be used to make non-planed maneuvers or even to climb higher in order to increase the energy stored as gravitic potential energy, thus saving more energy for night flight.

Having the geometry of the aircraft fixed, it is now possible to compute the V-n diagram. According to Federal Aviation Regulations (FAR) Part 23 [47] a maximum load factor of 3.8 should not be surpassed, and according to Raymer [1] the typical values stay between 2.5 and 3.8. With this data a maximum load factor of 2.5 was chosen. As for the wing gust diagram, the guidelines given in CS-VLA were followed. The V-n diagram for the winter aircraft can be found in Figure 4.8.

Despite the top speed from the analysis being 19.6 m/s equivalent speed, a reduction was needed, since the structure would be much heavier, and the aircraft would need to be

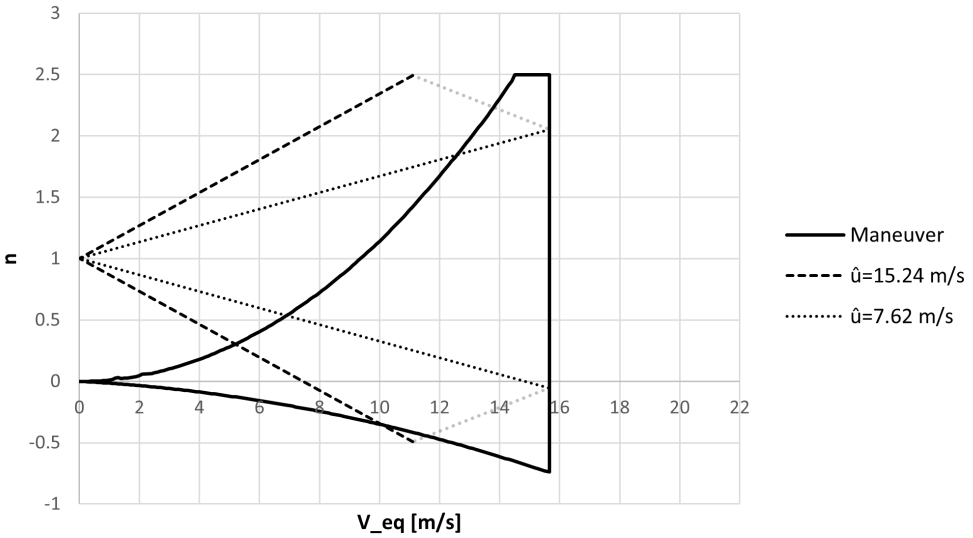

Figure 4.8: V-n diagram for the winter aircraft, with *û* as the mean gust velocity.

much larger to complete the mission requirements. The mission metrics can be seen in Table 4.3, and the drag polar can be seen in appendix A.4.

Table 4.3: Mission metrics for the winter prototype aircraft

Parameter	Value	Unit
Climb time from TO to day cruise altitude	4.2	h
Average climb rate	0.2	m/s
L/D	27.5	-
Power consumption	217	W
Power of propulsion system	142	W
Propulsion system efficiency	64	%
Stall speed	8.9	m/s
Cruise speed	13.3	m/s

For the stability of the aircraft, MIL-F-8785C [48] alongside XFLR5 were used (appendix A.5). The MIL-F-8785C defines 3 levels for the stability of an aircraft as follows:

Level 1: Flying qualities clearly adequate for the mission Flight Phase;

Level 2: Flying qualities adequate to accomplish the mission Flight Phase, but some increase in pilot workload or degradation in mission effectiveness, or both, exists;

Level 3: Flying qualities such that the aircraft can be controlled safely, but pilot workload is excessive, or mission effectiveness is inadequate, or both.

As for the static stability the aircraft is statically stable longitudinally, since $\delta C_M/\delta\alpha$=-0.011<0, and it has a static stability margin of 16% relative to the *CG* position at 27% of the wing chord. For the dynamic stability, it was found that the aircraft is only unstable in the spiral mode, which according to the MIL-F-8785C is in level 2, since it needs 8.2 s to double the amplitude. The remaining modes are all present in level 1.

It is important to mention that the wing will be built without dihedral angle, since this angle will be produced by the deflection of the wing due to the bending moment produced by the lift, which will be calculated in Section 4.2.5.1.

4.2.3 Summer aircraft analysis

For the summer aircraft all elements except wingspan were fixed, and consequently the solar cells' area, and the battery pack quantity. When analysed with the same componentes for the propulsion, avionics, control and electronics system, it was reached the values represented in Table 4.4. The chord, distance between the aerodynamic center of the wing and tail and tail dimensions, as well as the incidence of the wing and tail, remained constant.

Table 4.4: Summer prototype aircraft characteristics.

Parameter	**Value**	**Unit**
Wing span	5.30	m
Distance between aerodynamic center of the wing and tail	2.175	m
Total mass	20.668	kg
Battery mass (ratio of total mass)	6.477 (32)	kg (%)
Structure mass (ratio of total mass)	6.200 (30)	kg (%)

Regarding the energy balance of the aircraft, it is shown in Figure 4.9. Here the same points as the ones on the winter aircraft can be observed. The difference being the power usage, number of batteries and the amount of solar cells.

As for the V-n diagram, making use of the same strategy from the winter aircraft, it can be seen in Figure 4.10. Again, despite the analysed equivalent top speed being 21 m/s, a reduction was needed to decrease structural mass due to dynamic pressure. The remaining mission metrics are represented in Table 4.5.

For the stability, the same method as the one presented in the winter aircraft was used. As for the static stability the aircraft continues to be statically stable longitudinally, since $\delta C_M/\delta\alpha$=-0.013<0, and it has a static stability margin of 22% from the *CG* position at 27% of the chord. These results were expected, since with the same tail as the winter aircraft and a smaller wing, the equivalent horizontal tail is oversized. Regarding the dynamic stability, both phugoid and spiral modes are in level 2, with the fungoid damping

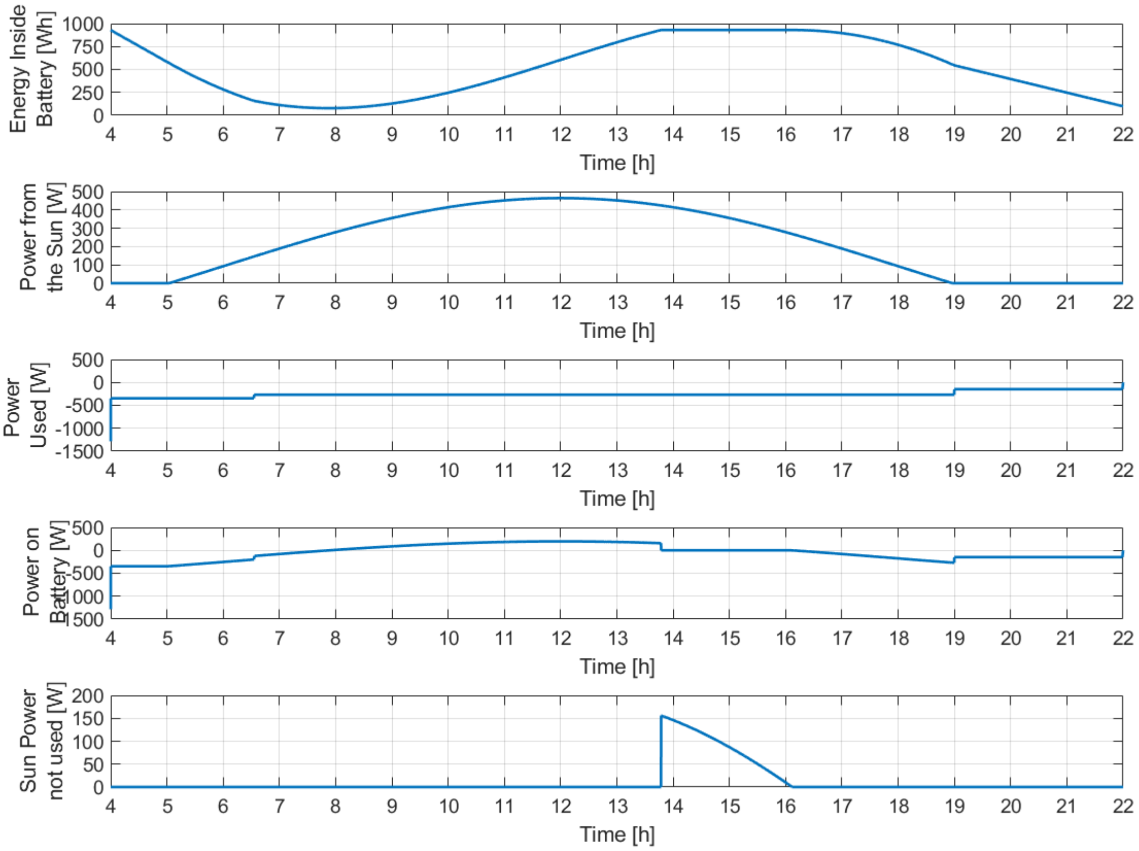

Figure 4.9: Energy and power graphs for the summer aircraft mission.

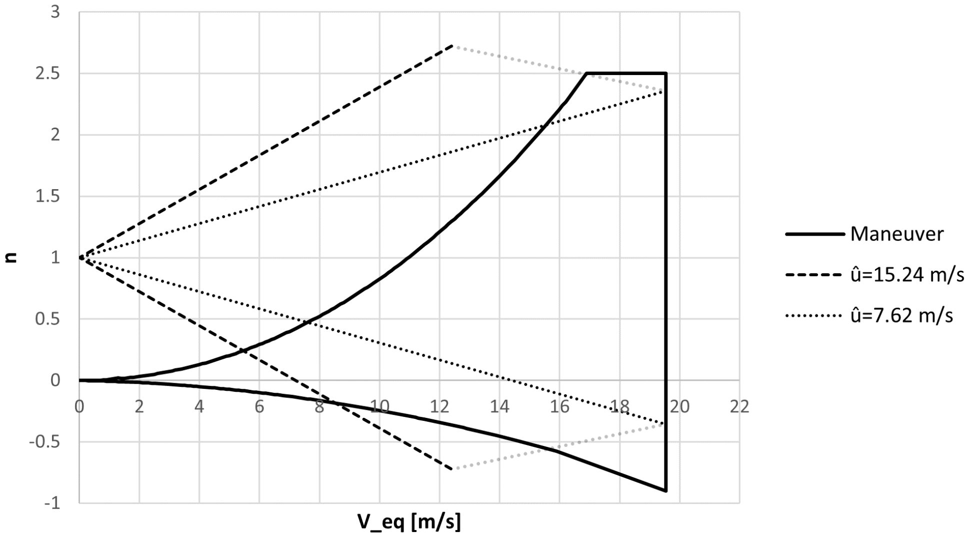

Figure 4.10: V-n diagram for the summer aircraft, with $\hat{u}$ as the mean gust velocity.

ratio at 0.028, and the time to duplicate the effect of the spiral mode at 7.8 s.

Table 4.5: Mission metrics for the summer prototype aircraft

Parameter	**Value**	**Unit**
Climb time from TO to day cruise altitude	2.7	h
Average climb rate	0.3	m/s
L/D	22.3	-
Power consumption	275	W
Power of propulsion system	197	W
Propulsion system efficiency	64	%
Stall speed	10.3	m/s
Cruise speed	14.4	m/s

4.2.4 Components inside the fuselage

In order to make the general shape of the fuselage, it was necessary to have the correct amount of space to put all components inside in the correct place, so the *CG* would be in the right place, at 27% of the wing chord. The table for the *CG* position can be found in appendix A.2. Figure 4.11 shows the internal layout of the fuselage, where the difference between the winter and summer aircraft is the two most backwards batteries, battery 4 and 5, which are removed. The current fuselage has 0.9 m in length, 0.2 m in width and 0.16 m in height.

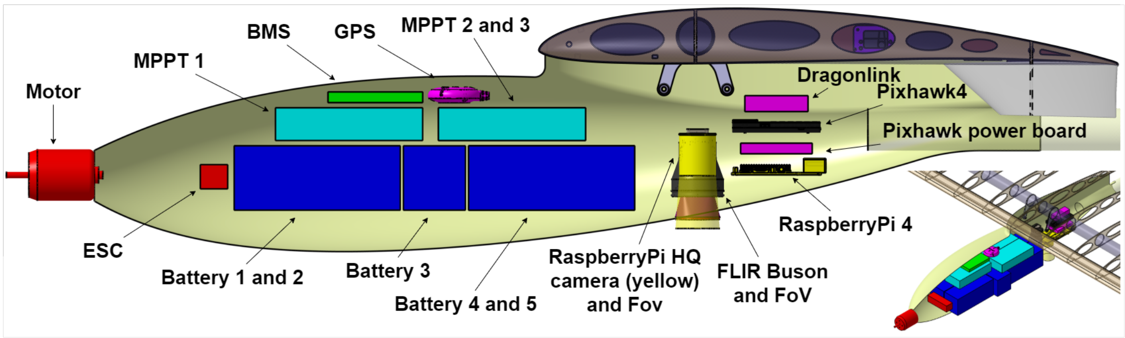
BMS
GPS
MPPT 2 and 3
MPPT 1
Motor
Dragonlink
Pixhawk4
Pixhawk power board
ESC
Battery 1 and 2
Battery 3
Battery 4 and 5
RaspberryPi HQ camera (yellow) and Fov
FLIR Buson and FoV
RaspberryPi 4

Figure 4.11: Components layout inside the fuselage.

It is important to note that in the figure it is visible an empty space in front of the ESC. This space exists in case the components need to be moved forward to correct the *CG* position. If it is needed to move the *CG* backward, there is room to move the MPPT backwards or in a worst case, some weights should be added to the tail. Due to the large distance between the tail and the *CG* position, the addition of tail weight should be very small if needed.

4.2.5 Wing structure

In this section, the wing structure, for the winter and summer aircraft will be presented in detail. Despite only being presented the detailed design of the wing, other parts of the aircraft should have the concept of the structure well thought. For the fuselage it should be made with a monocoque structure with carbon fiber, the tail boom should be made of a tube of carbon fiber since it is easy to fabricate or to find manufacturers, and the tail should follow the same structure concept that will be presented for the wing. The composite materials are very good for this type of structures since their specific strength is very high. Additionally, balsa wood is also on the list of possible materials to use for its very low density.

Before discussing in detail the detailed design of the wing, first it is necessary to define some aspects for the building of the wing. Since the aircraft will have wing extensions, it was chosen to divide the summer wing into 3 main panels, consisting of a middle panel and two panels containing ailerons. The wing panels and ailerons will have the same structure concept, consisting of a spar and ribs, with solar cells on the top part of the airfoils, and a film on the bottom side of the panel. It will also have a leading edge cap. Additionally, the wing panels will have connections to prevent motion between panels and relative to the fuselage. The final wing can be seen in Figure 4.12. During the sizing of the wing, a safety factor of 1.5 with a quality factor of 1.25 were used.

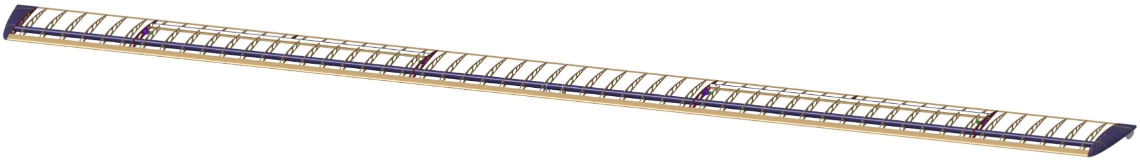

Figure 4.12: Complete wing structure without solar cells.

4.2.5.1 Spar

Starting from the spar sizing, first it was thought on using a main and a secondary spar. But it was verified that the use of a single, stronger main spar would be much easier to size and much lighter. This single spar is considered as the only load carrying element.

In order to size the spar, Torayca T700 prepreg fabric properties from a tube manufacturer capable of producing custom tubes was used. The properties of this prepreg material can be seen in Table 4.6 [49]. This fabric is available in 3 different variants: 160

g/m^2 unidirectional at 0 degrees, 300 g/m^2 unidirectional at 0 degrees and bidirectional at ±45 degrees with 400 g/m^2. In order to reduce the mass of the spar, it was divided into 5 sections, one for each wing panel, as seen in Figure 4.13. While the middle and intermediate wing panel have 1.765 m of wingspan, the tip panel only has 0.767 m of wingspan. Since there will be 2 different wingspan sized aircraft, the problem can be divided into 2 interlinked problems, where the first, for the summer aircraft have a middle and an intermediate spar, and a second that have the same middle and intermediate spar plus the extension panel spar. In both cases, the tip of the spar cannot deflect more than 10% of the wingspan (representing a maximum dihedral angle of 11 degrees) and rotate more than 2 degrees. The transition between two spars is also important, where the deflection and rotation (in the wingspan and length axis of the aircraft) should be equal from one spar to another. Before starting to do calculations for the spar, first the loads on each spar should be calculated. The load was assumed to be uniform, which is an approximation since the true load on the wing is similar to an ellipse, but this way the stresses are conservatively calculated, since the total bending moment will be calculated by the lift force obtained by the V-n diagram times one quarter of the wingspan, the drag is not considered since it is residual when compared to the lift force. As for the pitching moment, it was calculated for the pitching moment coefficient of the respective lift force of each case. This would give a wing loading as seen in Table 4.7.

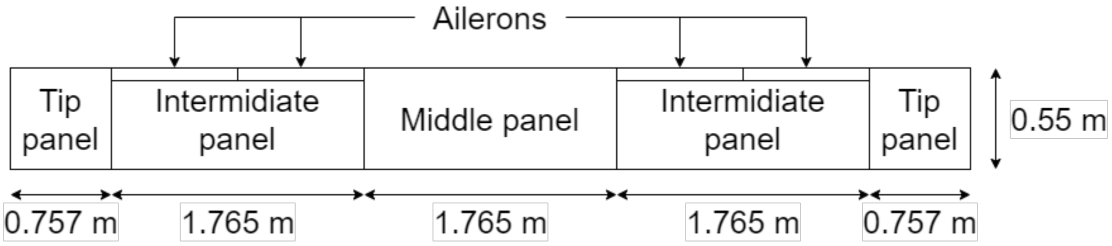

Figure 4.13: Wing panels layout.

Starting from the summer aircraft, three stations were created, the root, where a fixed support was implemented; the transition between the middle and the intermediate spar; and the tip of the intermediate spar. For each station the total tensile and shear stress for 4 points (top, bottom, left and right) is calculated with the following equations:

$$\sigma_{max} = \frac{L\left(b/2 - x_{station}\right)^2 D_{station}}{4bI_{station}} \qquad (4.25)$$

$$\tau_{torsion} = \frac{T_W\left(\frac{b}{2} - x_{station}\right)}{2A_{station}bt_{station}} \qquad (4.26)$$

$$\tau_{shear} = 1.5\frac{L\left(b/2 - x_{station}\right)}{A_{solid}b} \tag{4.27}$$

$$\sigma_{top} = -\sigma_{max} \tag{4.28}$$

$$\sigma_{bottom} = \sigma_{max} \tag{4.29}$$

$$\sigma_{left} = \sigma_0 \tag{4.30}$$

$$\sigma_{right} = \sigma_0 \tag{4.31}$$

$$\tau_{top} = \tau_{torsion} \tag{4.32}$$

$$\tau_{bottom} = \tau_{torsion} \tag{4.33}$$

$$\tau_{left} = \tau_{torsion} + \tau_{shear} \tag{4.34}$$

$$\tau_{right} = \tau_{torsion} - \tau_{shear} \tag{4.35}$$

where, σ_{max} is the maximum tensile stress of a given station, $x_{station}$ is the spanwise position from the centerline of the station, $D_{station}$ is the inner diameter, $I_{station}$ is the second moment of area of the section, $\tau_{torsion}$ is the maximum shear stress produced by the pitching moment in the station, T_W is the total pitching moment of the wing, $A_{station}$ is the cross section area, $t_{station}$ is the spar thickness at the station, τ_{shear} is the maximum shear stress produced by the shear force, A_{solid} is the full cross section area, σ_{top}, σ_{bottom}, σ_{left} and σ_{right} are the tensile stress at a given station for the 4 points and, τ_{top}, τ_{bottom}, τ_{left} and τ_{right} are the shear stress at a given station for the 4 points.

Table 4.6: Torayca T700 mechanical properties.

Property	**Value**	**Units**
Young' modulus (fiber directions)	104.3	GPa
Young' modulus (perpendicular to the fibers)	7.77	GPa
Poisson ratio	0.3	-
Shear modulus	3.6	GPa
Tensile strengh (fiber direction)	2354	MPa
Compression strengh (fiber direction)	1102	MPa
Tensile strengh (perpendicular to the fibers)	34.3	MPa
Compression strengh (perpendicular to the fibers)	184	MPa
Shear strengh	104.5	MPa
Density	1600	kg/m^3

Table 4.7: Wing loading for the wing spar sizing.

Aircraft	**V-n diagram conditions**		**L_{AC} [N]**	**Pitching moment coeficient, C_{M_W}**	**T_W [Nm]**
	n	**V_{eq} [m/s]**			
Summer	2.5	16.9	506.71	-0.13	36.426
	2.5	19.6	506.71	-0.13	48.995
	-0.9	19.6	-182.42	-0.09	33.920
Winter	2.5	14.5	468.05	-0.13	34.482
	2.5	15.7	468.05	-0.13	40.426
	-0.75	15.7	-140.42	-0.09	27.987

Next for each point in each section failure is verified using the maximum direct stress, the maximum shear stress and the Tsai-Hill criteria [50], where the maximum of the three is considered, where it is possible to see if that particular spar is oversized or undersized. In order to optimize the layer stacking, an evolutionary solver based on the theory of natural selection was used, where extra parameters such as a maximum of 10 layers, and to only use an integer number of layers are used. The objective of the optimization problem is to minimize the mass, given the material strengh and stifness constraints mentioned above. This solver works by creating a population for each iteration, where the base of that population is the best solution found from the previous one. The best solution of a given iteration is considered to be the one where the spar is lighter.

At the same time a similar approach is used for the winter aircraft, where now it exists 4 stations: for the root; for the transition between the middle and intermediate spar; for the transition between the intermediate spar and tip spar; and for the tip of the spar. Again, all stations have 4 points (top, bottom, left and right) where the stresses calculated above are calculated for this aircraft. Next, the failure criteria are evaluated to check if more, or less layers are needed. This process happens at the same time as the process for the summer aircraft since the most critical case is considered for final evaluation, and the middle and intermediate spar are shared between the two aircraft. Other important factor is that the inner diameter of the spar was fixed to be 36 mm, since most companies use a rolling method for the fabrication of the tubes, where the inner diameter is easier to control. From combined analysis of the winter and summer aircraft, it was found the following spar properties for each section:

Table 4.8: Spar properties for each section.

Section	**Number of layers**			**Inner diameter [mm]**	**Thickness [mm]**
	0° 160 g/m²	**0° 300 g/m²**	**±45° 400 g/m²**		
Middle panel	0	3	2	36	1.73
Intermidiate panel	1	1	3	36	1.69
Tip panel	0	1	1	36	0.57

With this layer stacking, the summer aircraft would have its wing tip deflected a maximum of 5.4% of the wingspan and it would twist a maximum of 1.53 degrees, while the winter aircraft would have its wing tip 8.2% deflected with respect to the wingspan and it would twist 1.72 degrees for a load factor of 2.5 and maximum diving speed. The inner diameter remained constant since it would be used for the connection of the wing panels. With these results it is possible to see that the winter aircraft would have a 4.5 degrees of dihedral due to the deflection of the wing, while the summer aircraft would have a 2.9 degrees, for a load factor of 1.

4.2.5.2 Rib

For the ribs, first it is necessary to know how many ribs the aircraft should have, or in other words the spacing between ribs. Since the wing would have full solar cell covering in the wingspan direction, and the solar cells would be glued to the ribs, it was fixed that the ribs should be positioned between the solar cells. First it was thought that two solar cells per pair of ribs should work, but from previous aircraft built it was quickly verified that the spacing of 252 mm, would probably create a large unwanted curvature to the skin. This unwanted curvature appears from the positive pressure from the bottom part of the wing, which forces the skin inward. If the distance between ribs is to large, this curvature, due to aerodynamic forces, pushes the skin even further in the wing, resulting in a deformed airfoil with unknown properties. This way only one solar cell, which have 126 mm by 126 mm including the space between cells, per pair of ribs will be used, giving a spacing between ribs of 126 mm. With this spacing, a total of 15 ribs in the middle and intermediate panels, and 7 ribs on the tip panels are used.

First it was thought that a sandwich, truss elements with an external contour would be used. At this time, a secondary spar and 2 solar cells per pair of ribs was still being used. After analysing the structure with the help of Mechanical Workbench of Ansys [51] software in order to optimize the structure, it was found that the truss elements would need two different types of sandwich. This analysis would have the main spar connection fixed and the load divided into two separate uniform loads; one from the leading edge up to the main spar (front load), and a second one from the spar to the trailing edge (back load). To calculate each load, a simulation in XFOIL was done for a Reynolds number of 300,000 and 4 degrees, obtaining the pressure coefficient graph seen in Figure 4.14. The pressure coefficient was integrated for the two conditions (front load, and back load). Next each load was divided by the total load on the rib, resulting in a front load ratio of 0.43 and a back load ration of 0.57, for a spar at 27 % of the chord, as seen in Figure 4.15. To calculate the total load of the rib it was considered the maximum lifting force component that comes from the maximum between the mass of the winter and summer aircraft divided by the respective number of spaces between ribs, 27 in the winter aircraft and 21 in the summer aircraft, times the maximum load factor from the V-n diagram, 2.5, giving a limit load of 24.12 N of force. The lift force was considered uniform which will not only simplify the calculation but also provides a conservative approach to the sizing of the ribs. As for the pitching moment, it was calculated for the corresponding lift coefficient of the wing, and considered the worst case between the summer and winter aircraft, divided by the number of ribs. The pitching moment was also considered uniform along the wing. It is important to note that the ribs in the tip and middle of a panel are equal, meaning that the tip ribs are oversized.

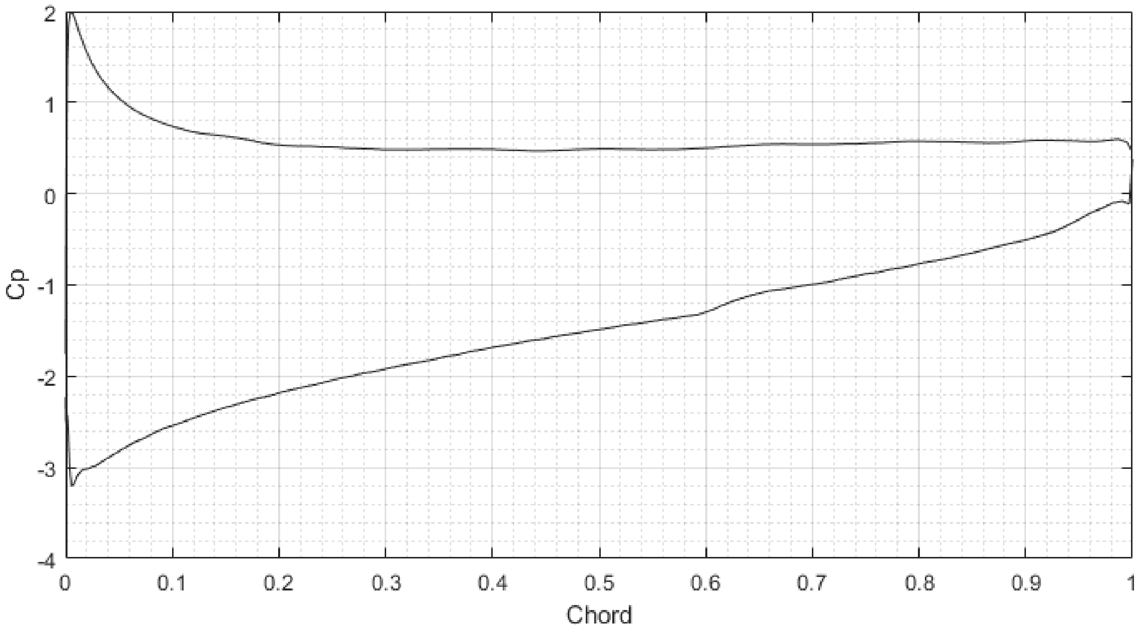

Figure 4.14: Pressure coefficient graph for the wing airfoil with a Reynolds number of 300,000 and 4 degrees of angle of attack.

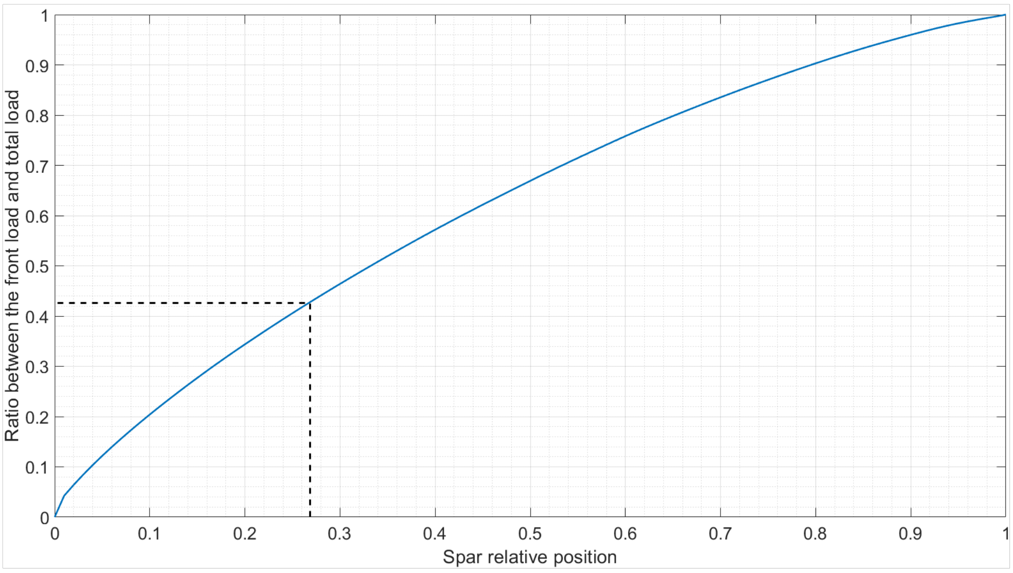

Figure 4.15: Ratio between the force from the leading edge to the spar (front load) with relation to the total load.

As for the material, the first type, found in the truss elements and the external contour, would be made of 2 layers, on each side, of 30 g/m^2 carbon fiber unidirectional and 2 mm green AIREX core. These elements would have the fibers aligned with them. The second type, found in the region of the spars, would be made of 2 layers of 30 g/m^2 at +45 and -45 degrees, with 2 mm green AIREX core. This sandwich would allow to transmit the loads to the spars. Figure 4.16 shows the safety factor from the analysis made where it is possible to see a very small element with a safety factor bellow 2, due to mesh problems when changing layers very rapdly. Due to the origin of this problem this element was considered not important.

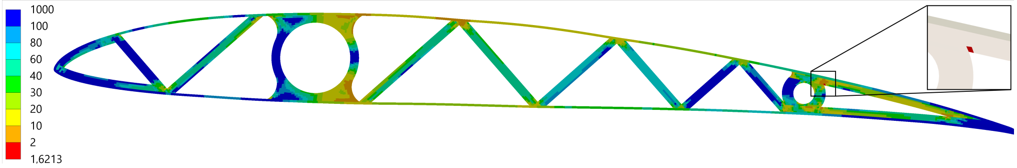

Figure 4.16: Safety factor of the carbon fiber sandwich wing rib from the software structural analysis.

This rib was also built and tested with point loads in order to simulate the real loads. During this test it was possible to see that the manufactured rib was double the expected mass, 10 g instead of the estimated 5 g. This increase in mass was due to the fact that the AIREX core absorbs a lot of resin during the laminating process. During the test, it was found that the rib broke at 2.6 times the limit load due to instability. Taking into consideration a 1.25 quality factor for the fabrication process, it would give a safety factor of 2. This carbon fiber rib is shown in Figure 4.17, where the areas of bidirectional sandwich are marked with red.

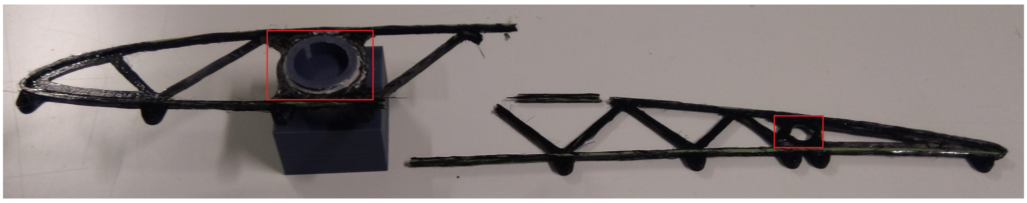

Figure 4.17: Carbon fiber sandwich rib, with a bidirectional sandwich marked by the red areas.

To manufacture this type of ribs four molds printed in PLA were used, where two of the molds would press agaist the sides, and the the other two would press the rib from the top and bottom. Next the manufacturing process started by putting the carbon fiber aligned with the truss elements on one of the side molds, followed by the AIREX core (with the truss shape) and the second carbon fiber layer, and finally the other mold side. For the countour part of the airfoil, a strip of laminated carbon fiber sandwich with AIREX core, was put around the airfoil, followed by the top and bottom molds to secure the strip in place. This process takes more than 3 hours per rib, and was found to be too hard and time-consuming, since the fibers of each element of the truss and external contour would have to be aligned individually. The use of a pre-made sandwich sheet made with bidirectional fibers was thought to substitute this method, but the increase in mass would not be justified, despite the easiness of fabrication since it would only need to be cut with the truss element size. So, an alternative was to design balsa wood ribs.

For the new 3 mm thickness balsa ribs, only the main spar and a single solar cell per pair of ribs is considered, changing the limit load applied to the ribs to 12.06 N due to the increase of the ribs number. Iterations were made from a full balsa rib to the final rib visible in Figure 4.18. For the load test a setup shown in Figure 4.20, consisting of levers, was used to distribute the load to the correct point loads of the rib. This way, the total load could be applied directly to the setup and distributed to point loads. Because of uncertainty of the balsa density and mechanical properties [52], it was seen by tests made that the balsa density should be considered around 150 kg/m^3 as well as a final load of 40 N for the final rib design, giving a safety factor of more than 2.5.

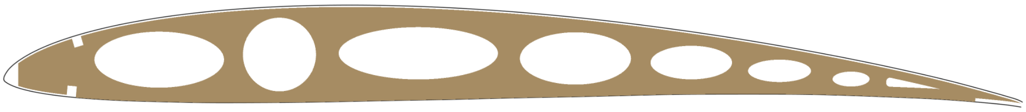

Figure 4.18: Balsa rib.

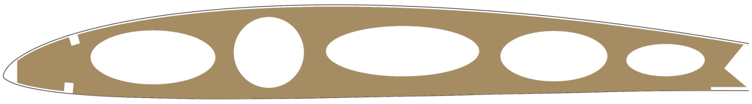

Figure 4.19: Balsa rib used on the aileron panel.

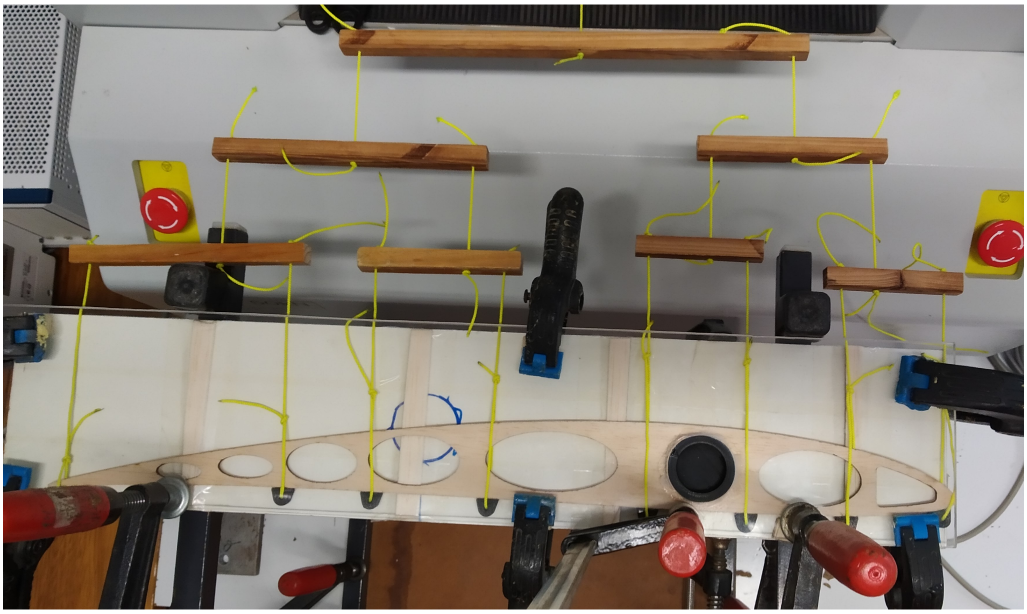

Figure 4.20: Setup for testing the balsa ribs.

As for the tip panel ribs, the use of a stronger wood is necessary to resist the pulling force from the skin on the underside of the panel. A 4 mm plywood rib with similar holes of the balsa rib is used. For this specific rib, the force derived by the torsion pin was also tested. The rib only broke after the expected final load. Proving the validity of the rib. This type of ribs can be seen in figures 4.21 and 4.22.

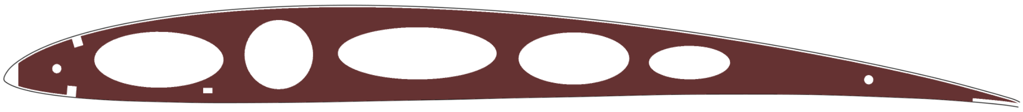

Figure 4.21: Plywood rib.

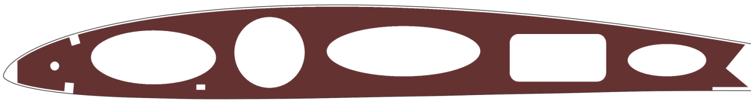

Figure 4.22: Plywood rib used on the aileron panel.

The ribs of the intermediate panel need 2 sheets of 1 mm balsa in order to close the trailing edge. This will allow creating space for the deflection of the aileron.

It is important to note that the ribs shown in Figures 4.18, 4.19, 4.21 and 4.22 have cuts (shown as the difference between the airfoil outline in black and the actual ribs) to account for the solar cells with an estimated thickness of 1 mm, leading edge sheets with 1 mm thickness, leading edge spars, trailing edge sheet made of 2 mm balsa that will help glue the skin, and in the case of the plywood ribs they also have holes for the torsion pin, axial pin and for the servo position in the case of the aileron panel. These cuts can be seen by the difference from the airfoil in black to the actual rib. Another important factor is that all ribs are able to be laser cut, reducing the fabrication process time considerably.

4.2.5.3 Leading edge

For the leading edge, the first idea was to use a carbon fiber sheet with the leading edge shape to make sure the leading edge kept its original shape. In order to know the correct amount of layer, or even if the need of a sandwich type of composite was necessary, it was tested the manufacturing process. But the manufacturing process was proven to be hard, since to laminate the correct shape was not easy, and the carbon fiber sheet was not rigid enough.

To facilitate the manufacturing process, it was decided to use three small balsa spars, where two of these spars of 5 mm by 5 mm in cross-section would be used to support the top and bottom sheets, while a leading edge spar would cover the leading edge of the wing. Additionally, two more rectangular balsa sheets with a thickness of 1 mm would also be used. This process also requires for the skin to completely cover the leading edge. This structure is represented in Figure 4.23. Note that the top spar is not completely covered by the balsa sheet. This will allow to also support the solar cells in the right position.

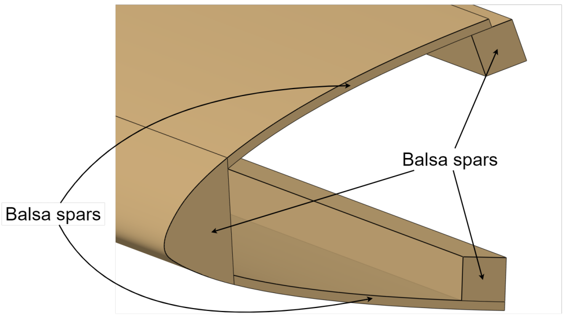

Figure 4.23: Leading edge structure.

In order to have the right shape of the leading edge spar, a square shaped cross-section balsa spar could be machined to the most approximated shape possible followed by a polishing process to give the final smooth and correct shape. Then the three spars should be bonded to the ribs in the correct position, followed by the bonding of the two balsa sheets. To give a smooth finish between the parts some sanding should be made in order to flush the leading edge spar with the balsa sheets.

4.2.5.4 Solar cell encapsulation

Regarding the solar cells encapsulation, it was decided to do 4 different size panels to fit all solar cell places of the wing (main panel with a 4 by 14 grid, intermediate panel with a 3 by 14 grid, tip panel with a 4 by 6 grid and aileron surface with a 1 by 7 grid), as shown in Figure 4.24.

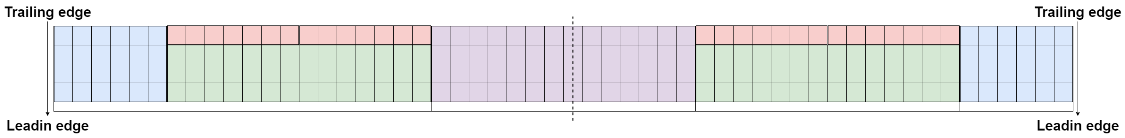

Figure 4.24: Solar cell layout. Purple - grid 3 by 14; Green - grid 3 by 14; Blue - grid 4 by 6; Red - grid 1 by 7.

Before encapsulating the solar cells, first it is needed to make the electric connections between cells of the same panel. To do that task, spacers with no more than 1 mm should be used to make sure each cell is no more than 1 mm apart from the cells next to it. After the soldering of the solar cells, a bay with the size of each different panel 1 mm deep should be created, this will allow to control the thickness of the solar panel.

Following this step, a laminate is created, between the bay boundary and 2 layers of straight glass, with a sheet of glass fiber, the soldered solar cells and resin. Finally, some weights should be put on top from the center to the tips in order to remove not only excess resin but also air bubbles that would reduce the solar cell efficiency. The layers of this process are shown in Figure 4.25.

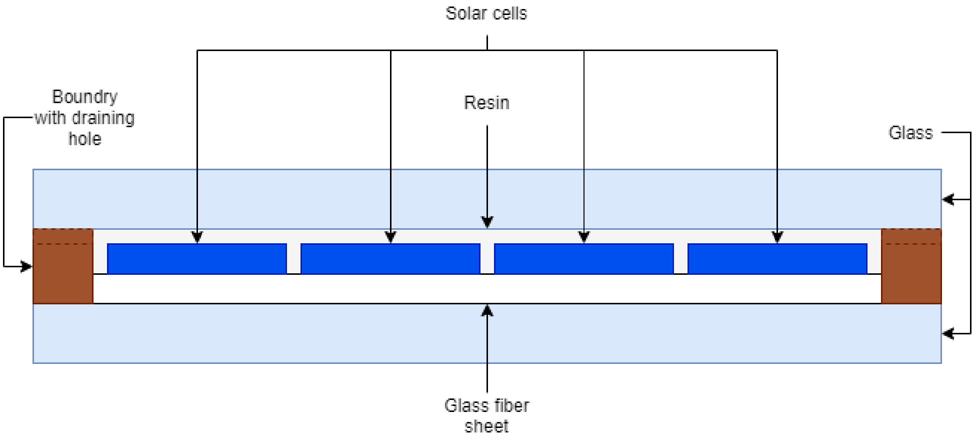

Figure 4.25: Solar cell encapsulation layers.

To connect the manufactured panels to the wing structure, glue should be used. Since the solar panels are flat, flexible and with the exact dimension necessary to cover the top of the wing panels, it should fit between the leading edge cover and the trailing edge. The top of the wing panels are now fully covered. It is important to note that it is expected some electric efficiency loss during the encapsulation process. As seen in prevous works [28], where a study of solar system for a long endurance UAV was made, it was concluded that covering a solar array with transparent film would reduce about 1 % in efficiency. With those results it is excpected to have an equal or slightly bigger loss, since the solar cells will be covered by resin instead of a transparent film. Other factors like temperature also have impacts on the solar cell efficiency, since colder cells also provided higher efficiencies.

4.2.5.5 Aileron structure and assembly

The aileron structure can be divided into several parts, like the wing. In order to reduce the servo workload and as a redundancy feature, two aileron surfaces on each side of the wing (in the intermediate panels) will be used, as shown in appendix A.6.

Starting from the aileron spar, a similar approach to the wing spar is used. Where before, the loads were calculated with the V-n diagram, this time the lift can be calculated by integrating the pressure coefficient with the chord and span of the aileron, where the pressure coefficient can be obtained by an analysis of the airfoil with the aileron deflected 20 degrees down in XFLR5 for maximum dive speed, and with 0.13 m of chord and 0.88 m of aileron span. The pressure coefficient of the airfoil for this analysis can be seen in Figure 4.26, where the red boundary represents the region of the aileron, or in other words, the interpolation region of the pressure coefficient. This way, a limit load of 13.8 N was calculated. The hinge moment is calculated by Equation 4.36, where the hinge moment coefficient is obtained with the XFLR5 analysis done previously, with the value of 0.2, giving a hinge moment of 4.13 Nm.

$$H_{mom} = 0.5\rho V^2 C_{H_{mom}} b_{aileron} \quad (4.36)$$

where H_{mom} is the hinge moment, $C_{H_{mom}}$ is the hinge moment coefficient and $b_{aileron}$ is the aileron span.

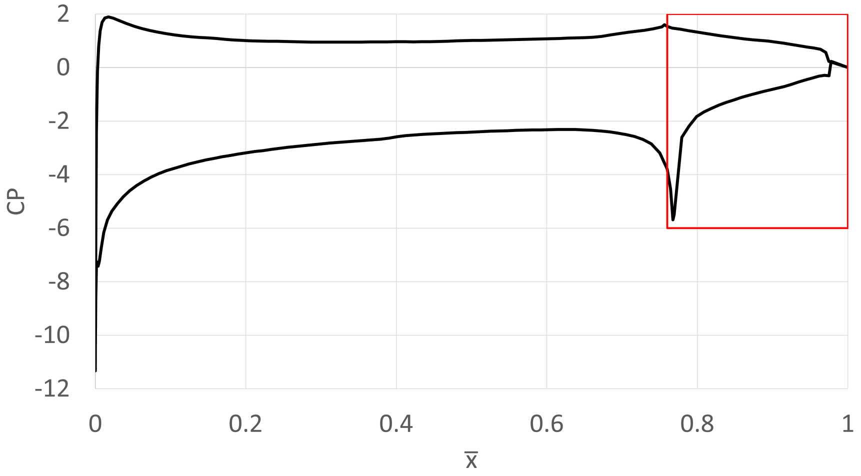

Figure 4.26: Pressure coefficient as a function of the relative position of the chord, $\bar{x}$, where the red boundary represents the aileron position.

By using the same materials as the ones used for the wing spar, the properties in Table 4.9 were found, where a maximum relative deflection of 1.1% and a maximum rotation of 1.93 degrees is achieved.

Table 4.9: Aileron spar properties.

Section	**Number of layers**			**Inner diameter [mm]**	**Thickness [mm]**
	0° 160 g/m²	**0° 300 g/m²**	**±45° 400 g/m²**		
Middle panel	0	0	1	18	0.41

Additionally, in order to pass cables from the solar cells on the aileron surface to the wing panels, holes in the spar where cut, together with cable guides on the tip of the spars to prevent unwanted twisting of the cables that could lead them to break during flight. Figure 4.27 shows a representation of this part of the aileron spar.

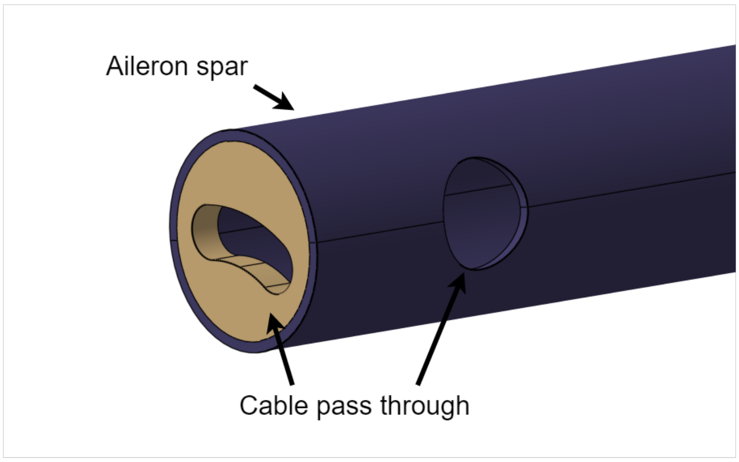

Figure 4.27: Aileron spar tip with cable guide.

Next, for the ribs of the aileron with the same spacing as the ribs of the wing, the same materials as the ones used on the wing panels will be used. This means the tip ribs are made of 4 mm plywood, and the middle ribs are made of 3 mm thick balsa wood. These ribs can be seen in Figure 4.28. Note that the plywood ribs do not have any holes, this is to prevent an opening to appear when the aileron is deflected.

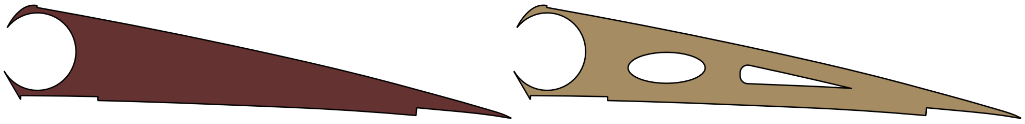

Figure 4.28: Aileron tip ribs (left) and middle (right).

It is important to note that while the wing only has a sheet of 2 mm balsa on the trailing edge, these ribs require a 2 mm sheet on the trailing edge and a 1 mm sheet on the leading edge. This 1 mm sheet is required to have enough material on the rib to glue on the spar.

Since there will exist a gap between the leading edge made by the aileron spar, and the solar cells, a leading edge sheet should be built. This sheet is made of two layers of bidirectional carbon fiber composite at ±45 degrees with 30 g/m^2. The aileron will also have its bottom part covered by a skin, similar to the wing.

In order to fix the aileron to the wing, nylon hinges are used. It was found that 4 hinges per control surface should work, but calculations for the transmitted load from the aileron to the wing ribs were made. This way, 3 options where available. Counting from the inner tip rib of the wing intermediate panel, the hinges would be located on the ribs as shown in Table 4.10, where the increase to the final load on those ribs, relative to a normal rib, is also presented.

Table 4.10: Hinge position marked by the percent increase to the final load in the intermediate panel ribs.

	Inner aileron								**Outer aileron**							
Rib number	**1**	**2**	**3**	**4**	**5**	**6**	**7**	**8**	**8**	**9**	**10**	**11**	**12**	**13**	**14**	**15**
Option 1	2	-	27	-	-	27	-	2		-	27	-	-	27	-	2
Option 2	22	-	-	30	-	10	-	10		-	10	-	30	-	-	22
Option 3	-	16	-	2	2	-	16	-		16	-	2	2	-	16	-

Despite option 1 not being the one with less increase in rib loading, this option was chosen since it had hinges on both tips of each control surface. This would help to better secure the aileron to the wing panel. As for the control of the aileron, a part design to be built using additive manufacturing of PLA was done. This part, shown in Figure 4.29, is a ring that is glued to the aileron spar. The complete aileron structure attached to the wing is shown in Figure 4.30 and the aileron mounting can be seen in Figure 4.31.

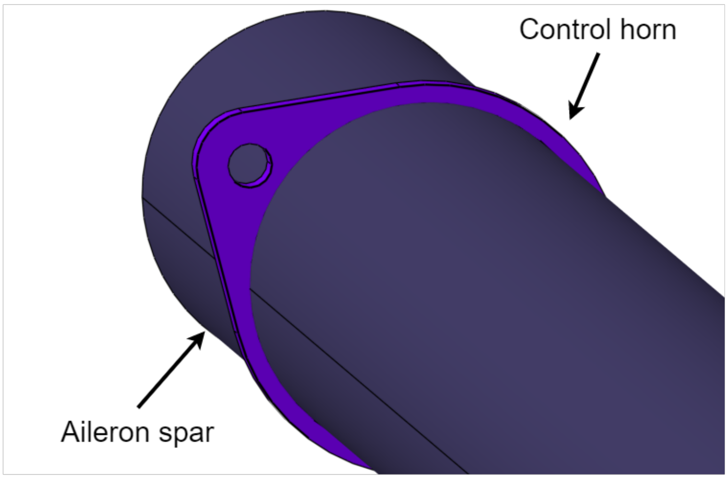

Figure 4.29: Aileron control horn.

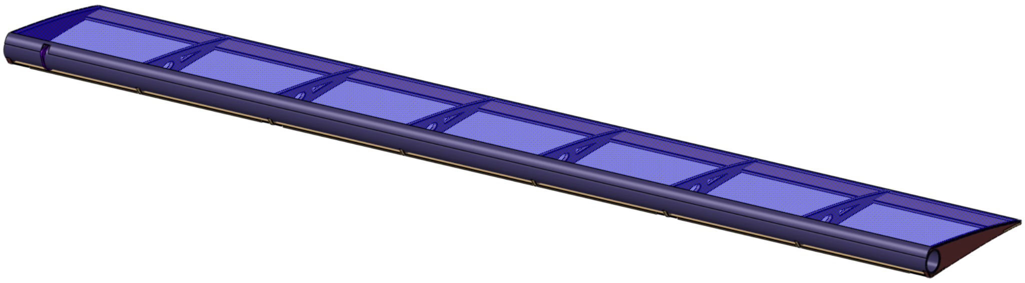

Figure 4.30: Complete aileron.

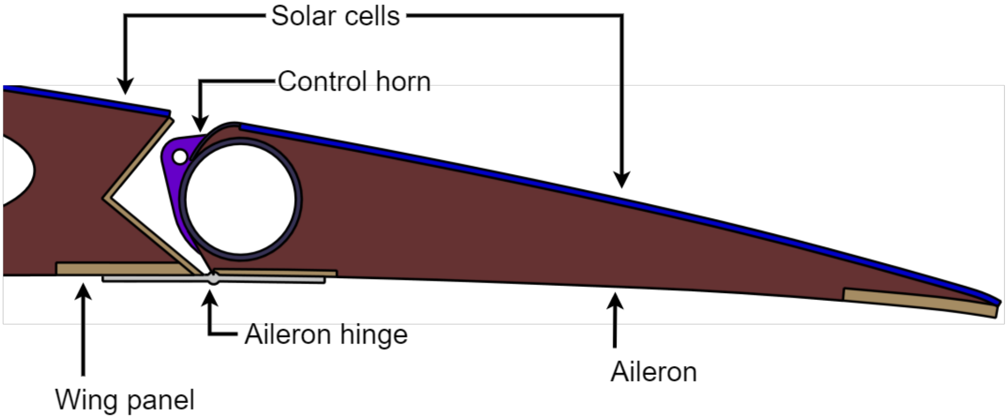
Solar cells
Control horn
Aileron hinge
Wing panel
Aileron

Figure 4.31: Aileron mounting.

4.2.5.6 Servo mount

For this part of the wing, the servo mount is designed. For that, a support on the tip ribs where the servo is inserted is designed to be built by additive manufacturing of PLA, since it will give more freedom to the design and make the fabrication process easy.

The servo mount will be located on the tip ribs of the aileron panels and composed by 2 complementary parts. The first one will be fixed to the rib and will not only secure the servo in place, but also transmit the force of the servo to the rib. This part is glued to the rib face, and can be seen in Figure 4.32. As for the second part, it will serve as an adapter to the servo to fix on the first part and can be seen in Figure 4.33. It should be noted that since there will be two different control surfaces on each side, two different parts are designed for the servo to be in the correct orientation. This system is integrated with the aileron as shown in Figure 4.34.

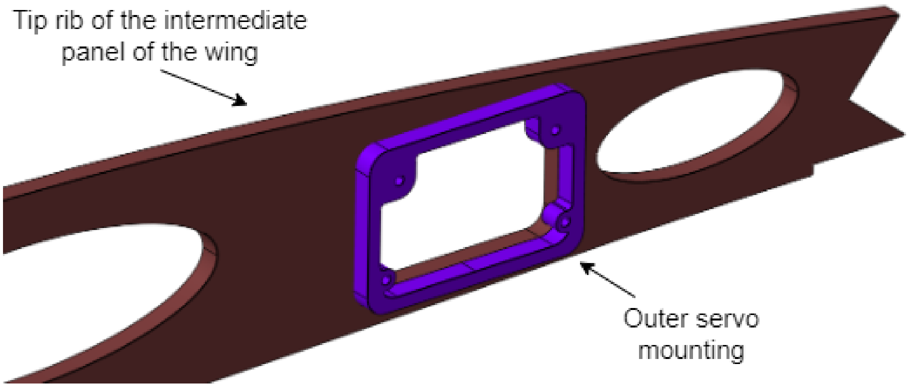
Tip rib of the intermediate panel of the wing
Outer servo mounting

Figure 4.32: Servo mount, outter part.

It is important to note that both parts should use threaded inserts, to greatly increase

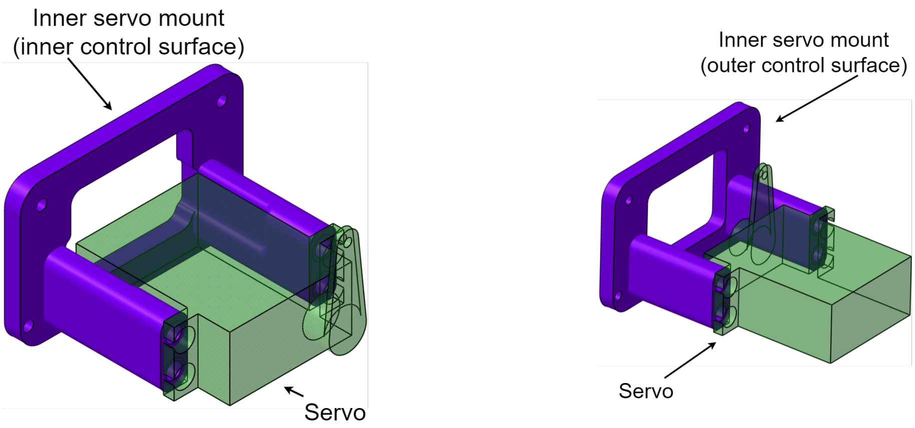
Inner servo mount
(inner control surface)
Servo
Inner servo mount
(outer control surface)
Servo

Figure 4.33: Servo mount, inner part, for the inner control surface (left) and outer control surface (right).

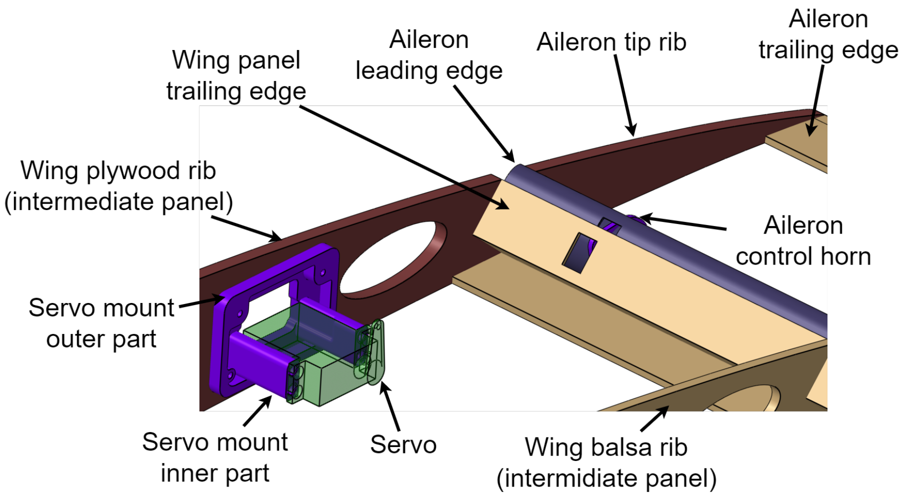
Wing panel
trailing edge
Aileron
leading edge
Aileron tip rib
Aileron
trailing edge
Wing plywood rib
(intermediate panel)
Aileron
control horn
Servo mount
outer part
Servo mount
inner part
Servo
Wing balsa rib
(intermidiate panel)

Figure 4.34: Servo integration with the aileron.

the lifetime of the PLA parts that are joined by bolts. For example, a IUB-M2-1 from SI brand, that uses heat to melt the plastic while inserting the threaded insert, after the insert is in the right place the plastic cools down and secures the threaded insert, creating a brass nut inside the plastic part.

4.2.5.7 Wing tip

The wing tip design is not easy. The wing tip should have a part facing down in order to protect the skin of the bottom part of the wing from touching the ground and potentially break the skin. The first iteration of the wingtip was composed by a smooth rotation and tapering of the airfoil 90 degrees down. It would be made from carbon fiber with a tip of glass fiber, since glass fiber has good abrasion properties.

This type of wing tip would require a very hard and time demanding fabrication process, for the molds and laminating process. In order to fix that, the wing tip was switched to a two parts piece where the first part would close the wing tip, and a second part would be facing down to protect the wing skin. The first part would be made of carbon fiber due to its light weight, as the second would be made from glass fiber. Inside this panel two spars with the function of passing the loads to the wing panel were added. This process is much easier because it allows to have the wing tip build in two different parts that are glued together. The final result is shown in Figure 4.35.

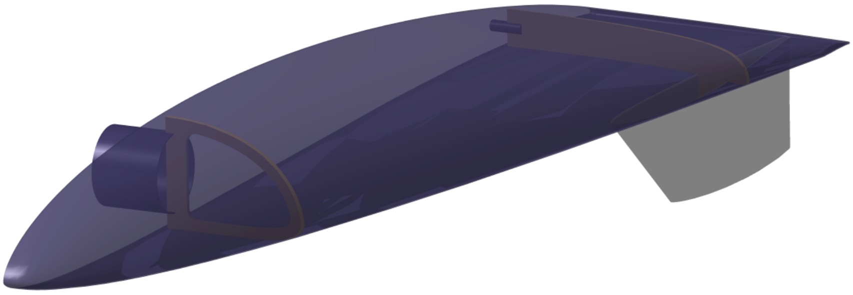

Figure 4.35: Final wing tip.

4.2.5.8 Wing connection

The wing connections can be divided into 4 categories. The first category is responsible to transmit the bending moment between spars of two different wing panels. All panels have the same connector. This connector was sized similarly to the spar with the critical bending moment between the middle and intermediate spar. As for the material used, it was the same as the ones used on the spar of the wing. One thing to keep in mind is that the inner diameter was iterated in order to have the tighter connector that could resist the loads. Another thing is that this connector should not allow a higher deflection between spars, since the analysis from the wing spar assumed a continuous spar despite changing dimensions between panels. This connector will not have any torsion applied to it, but a single layer of ±45 degrees fabric was added to prevent the unidirectional layers from breaking from unexpected loads. The laminate layers and dimensions are presented in Table 4.11.

Table 4.11: Spar connector layers and dimensions.

Section	**Number of layers**			**Inner diameter [mm]**	**Thickness [mm]**
	0° 160 g/m²	**0° 300 g/m²**	**±45° 400 g/m²**		
Middle panel	4	1	1	32	1.80

One thing to keep in mind is that despite the wing panel connector had 20 cm of length each, the wing tip connector only had 3 cm, since the bending moment of this part of the aircraft is not significant.

Next, the torsion pin connector will prevent the panels to rotate alongside the wingspan axis. This pin will be a carbon fiber rod with 5 mm diameter, since with this dimension it should be able to sustain the final load without breaking. This pin will be presented on the leading edge of all wing panel to wing panel connection, and it will be located on the trailing edge of a wing panel to wing tip connection. This switch to the trailing edge is due to the fact that an impact from the ground is supported by the trailing edge of the wingtip, and the load should be transmitted to the spar of the wing. This way, the stresses from the wing tip can be transmitted to the plywood rib of the wing panel.

Lastly, a pin to prevent axial motion of the panels is needed. This is just a safety feature to be sure the wing does not come off during flight. This is a very small piece of steel, with a thread on one of the sides. It will be used on every panel tip rib of the wing. It has a prismatic shape where half is glued to one panel, and the other side has a thread for a screw that passes through the rib of the other panel. These 3 wing connectors are shown in Figure 4.36.

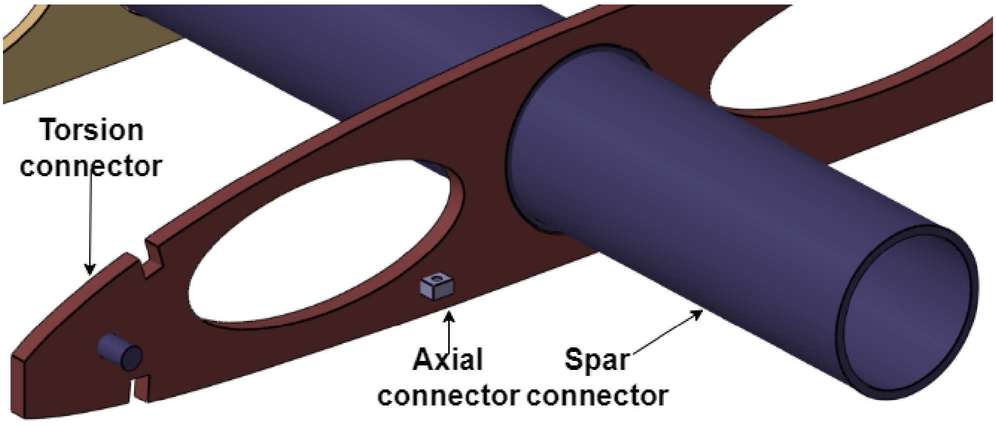

Figure 4.36: Wing spar, torsion and axial connectors.

Another connector that must exist on the wing is the connection between the wing and the fuselage. For this, two aluminium AL 7075 3 mm sheets, with an inverted V shape are used. On the wing it will be glued to the spar with a fiber glass sheet in between, while for the fuselage part riveting nuts will be used. These riveting nuts allow to permanently fix nuts to the aluminium sheet, since it consists of a rivet with a thread on the tip, for example M4RESO-S-T from Rivetwise, which provide a M4 riveting nut. This connector is shown in Figure 4.37. The glass fiber sheet will be used to isolate the aluminium from the carbon fiber, and thus prevent galvanic corrosion. In Figure 4.38 the result of a load test is shown. In this test, the forward arm is loaded with 8 N while the backward arm had 246 N for the condition of maximum load factor ($n = 2.5$). An additional load of 50 N in the direction of the wingspan was also added to account for lateral impacts that might occur in the ground. Since the maximum load of the material, accounting with the safety and quality factor, is 260 N, it is possible to see that this part can handle the final load during flight. It is important to note that the shear load on the connection with the wing spar should not be above 30 MPa, since the resin will take the torsion load from the wing.

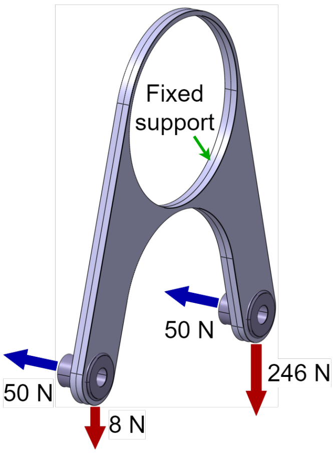
Fixed support
50 N
246 N
50 N
8 N

Figure 4.37: Wing connector for the fuselage and applied loads.

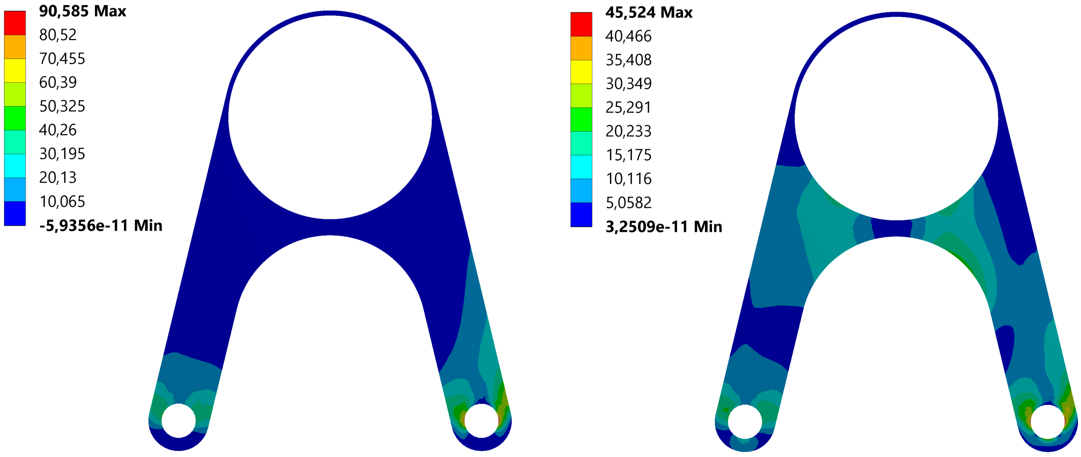
90,585 Max
80,52
70,455
60,39
50,325
40,26
30,195
20,13
10,065
-5,9356e-11 Min
45,524 Max
40,466
35,408
30,349
25,291
20,233
15,175
10,116
5,0582
3,2509e-11 Min

Figure 4.38: Maximum principal stress (left) and maximum shear stress (right), in MPa, for the connector between the wing and the fuselage.

4.2.5.9 Validation of the structure

To validate the structure concept, the structure of a section of the aileron panel with 3 ribs, 2 with plywood and a middle one made of balsa was built. This test would allow to see any problems with the concept since it allows seeing problems that would happen in the middle and tip panels as well as problems from the aileron panel of the wing.

To make the section, a jig was designed, that can be adapted in the future to also assist on the wing building. The jig designed can be seen in Figure 4.39. It uses 2 sheets of 1.5 mm plywood to support the ribs, and 6 mm plywood to connect the supports. It also has 1.5 mm thick plywood *H* shaped supports to make sure the ribs are straight. During the building of the jig, it was found that extra support was needed to prevent the ribs from moving in relation to each other. This additional piece is built with 6 mm plywood and glued to the sides of the jig.

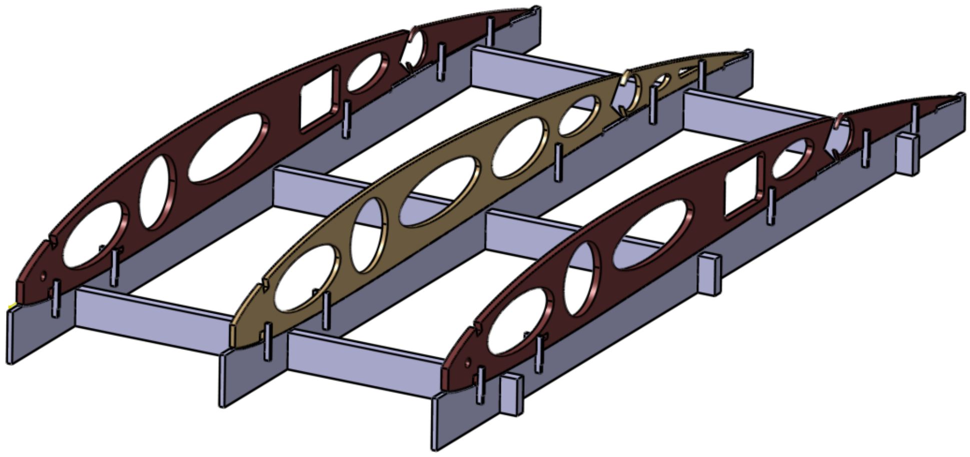

Figure 4.39: Jig used to help build the structure.

Some components were manufactured using additive manufacturing of PLA, for example the wing and aileron spar, torsion pin and axial pin. This was done since the correct tubes for the spar were not yet available and the section strength could not be tested before the conclusion of this thesis. The manufactured torsion and axial panel connectors can be seen in Figure 4.40.

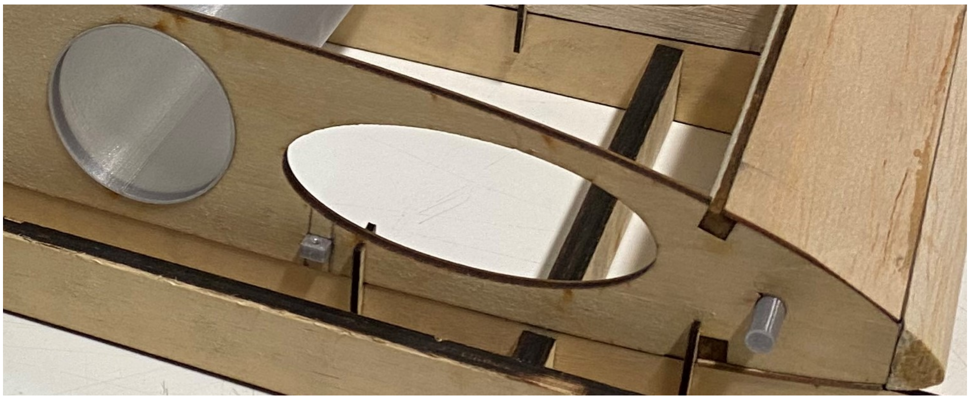

Figure 4.40: Panel torsion and axial connectors on the built wing section.

An important remark during the manufacturing process regarding the leading edge spar shape, as seen in Figure 4.41, is that in the full wing panel the leading edge should be machined first with a CNC router for example, then glued to the section and finally finished with sand paper together with the leading edge balsa sheets in order to produce a smooth surface. Passing to the axial pin connector, the wall thickness of the rib that is secured with the screw is too small, leaving less than 1 mm between the screw and the outer part of the rib. To fix this issue, an extra layer of 4 mm plywood is glued locally in order to increase the wall thickness around the screw. Next, the servo mounting needed corrections to better fit the screws and the threaded inserts as seen in Figure 4.42. The hole for the control rod from the servo to the control horn on the aileron was found to be too small, and the hole had to be increased up to the top of the balsa sheet. To support the larger hole, 2 smaller ribs were added on each side of the hole with 3 mm balsa, as shown in Figure 4.42.

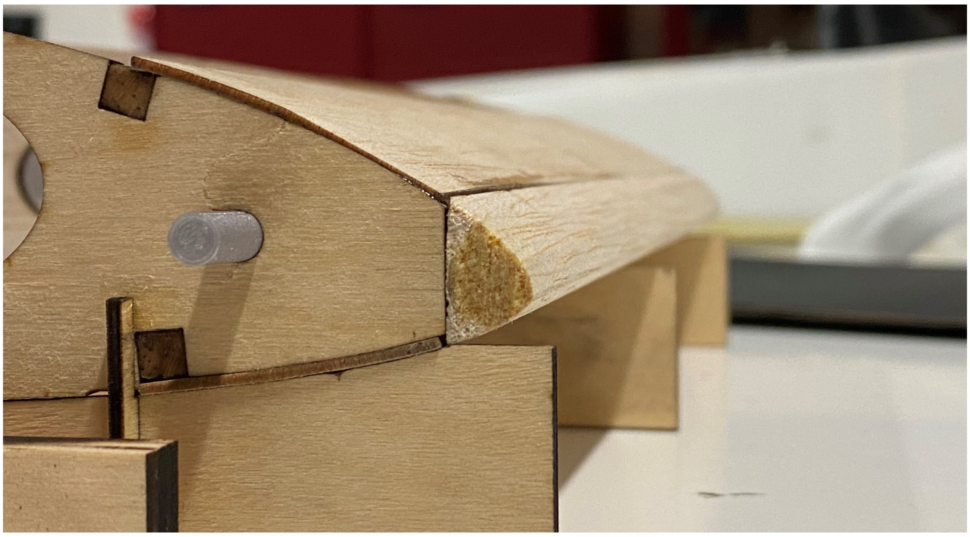

Figure 4.41: Leading edge of the built section.

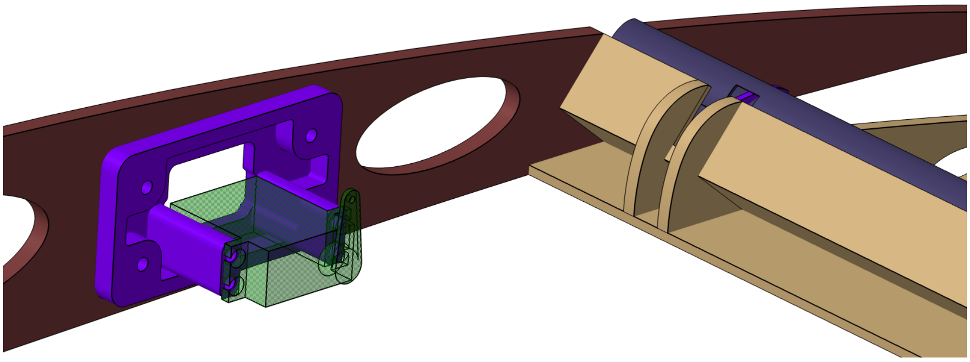

Figure 4.42: New servo mount and reworked trailing edge of the wing panel with the small ribs.

Considering to the aileron, the leading edge balsa sheet used to secure the skin should be changed to 2 mm thick, since the 1 mm sheet was found too flexible. This change will not only prevent unwanted curvature, by increasing the thickness and allowing the sheet to be supported on the aileron spar, but also allow the hinge to be flushed with the airfoil reducing the drag of the hinges. The control horn was also changed to be only half of a circumference, since the first iteration was found fragile, hard to mount, and it would prevent the aileron from deflecting up to its maximum extension. The final aileron mounting is shown in Figure 4.43.

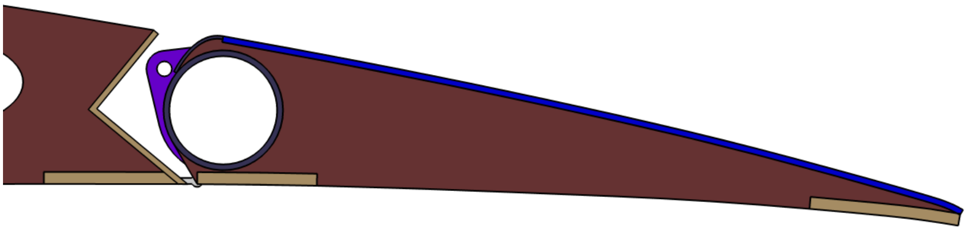

Figure 4.43: Reworked aileron mounting with flushed hinges and increased leading edge balsa sheet thickness.

When testing the solar cell encapsulation, the thickness around the soldering joints was found to be hard to control and usually they were thicker than 1 mm. This can cause problems on the ribs, since the ribs should be between solar cells. To try and solve the issue, the ribs were moved to the middle of the solar cells, where the thickness is better controlled. This process should not cause any problems with the loads, since each panel has an extra rib with this change. This change in position of the ribs is not shown in Figure 4.44, since this problem was only discovered after building the prototype panel.

As a final note, the ribs of the aileron and wing panel are somewhat fragile and should be handled with care until they are glued to the spars. After the spar of the panel, spar of the leading edge and the balsa sheets are glued to the wing panel, and the aileron spar is glued to the aileron panel, both structures are rigid enough to be handled. The final built structure can be seen in Figure 4.44.

4.3 Perpetual flight aircraft

In this section of the document, an aircraft to complete the main mission, shown in Section 3.1, will be sized. While the previous aircraft would only serve as testing ground, this aircraft is supposed to fully accomplish the mission objectives. The major achievement of this aircraft is the possibility of flying for several days without landing. It would carry the same payload of 0.4 kg with a peak power of 27 W, composed by and optical cam-

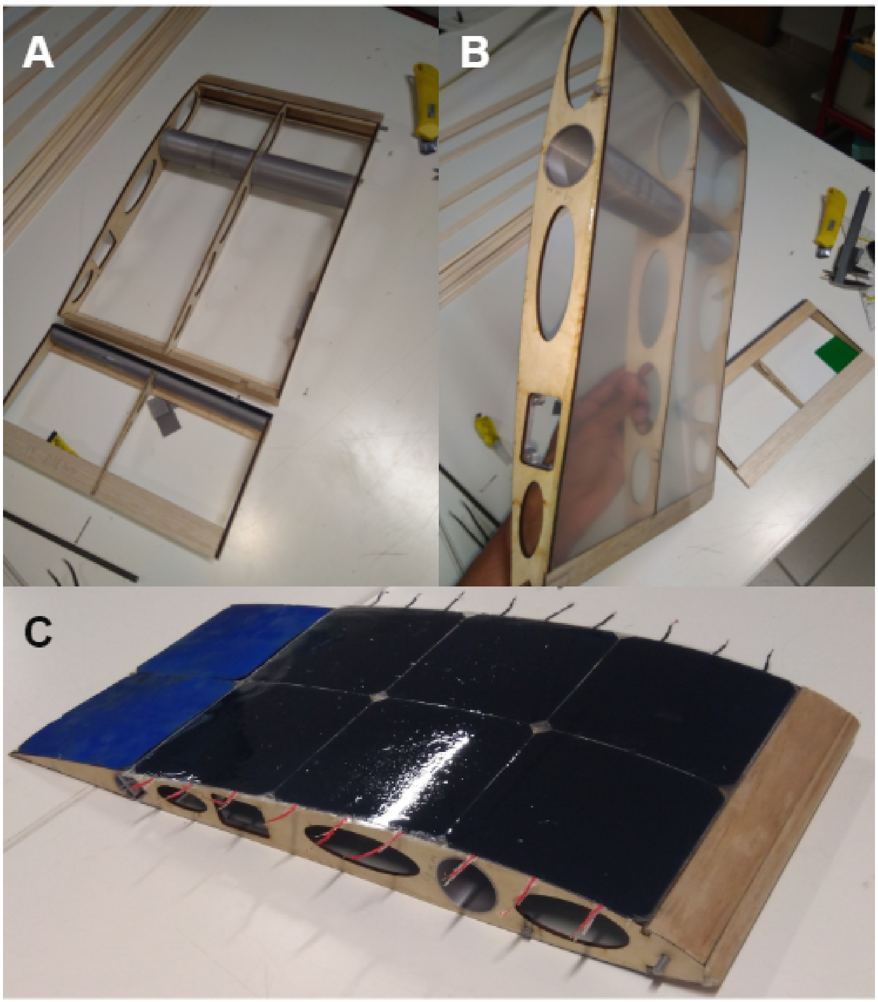

Figure 4.44: Built wing section. A - Without skin and solar cells; B - With skin on the bottom and without solar cells; C - With skin on the bottom and solar cells on top of the section.

era, thermal camera and an image processing unit as shown in Section 3.2. The avionics and control elements will also be the same as the ones in Section 4.2.1.3, with a total mass of 3.5 kg and 29 W of peak power.

4.3.1 Components

Like in the previous section, several iterations of components in order to select them was done. It is important to note that all components outside the propulsion and electronics group remained fixed, meaning that only the propeller, motor, ESC, battery and MPPT will change, since the size of the aircraft will change requiring different power requirements from these components. It is also important to note that the airframe mass module used is the same.

Regarding the propulsion group, a 50 in x 23 in folding propeller with two blades, a Hacker Q100 - 7L motor with a speed constant of 99 rpm/V, R of 8.5 mΩ, and a maximum current above 300 A with 3.2 kg, and a Jeti SPIN Pro 300 opto ESC with 0.2 kg capable of supplying constant 300 A were chosen. A gearbox was not considered since from the gearboxes found for this amount of power it would be very heavy and with low efficiency.

Passing to the electronics group, a 23 Ah capacity battery with 2.478 kg from MaxAmp was chosen, since this is the battery pack with the highest specific energy inside that brand. As for the MPPT, the MG Energy Systems WSC-si capable of 700 W was chosen due to its high-power rating and compatibility with silicone substrate solar cells. These components can be seen in Figure 4.45.

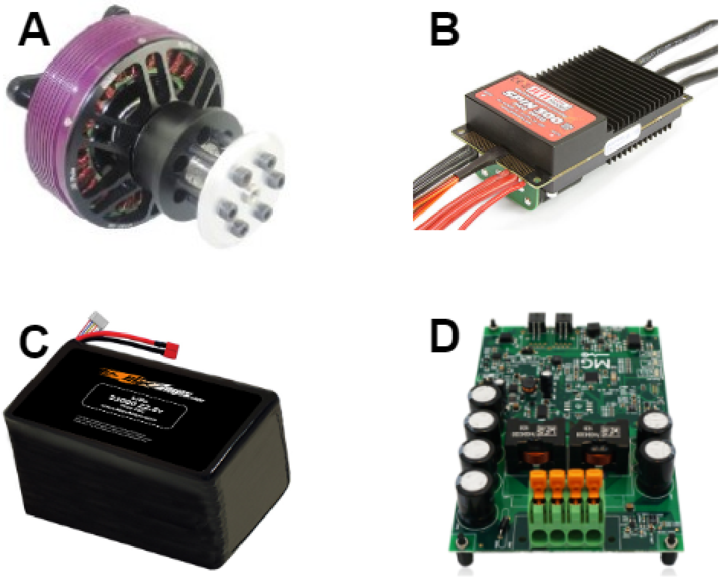

Figure 4.45: Full size aircraft components. A - Hacker Q100 - 7L motor [53]; B - Jeti SPIN Pro 300 opto ESC [54]; C - MaxAmp battery with 23 Ah capacity [55]; D - MG Energy Systems WSC-Si MPPT [56].

4.3.2 Aircraft analysis

After iterating the aircraft size together with the battery pack quantity, and using the same airfoils for the wing and tail section of the aircraft (WE3.55-9.3 for the wing and E193 inverted for the tail), a final aircraft described by Table 4.12 was achieved. Several simulations, seen in Figure 4.47, were made to achieve the final aircraft. It is important to note that the smallest aircraft with 17.5 m of wingspan and 88 kg was chosen due to mission requirements, but if the wingspan would increase to about 18.5 m (+5.7%), the total mass would decrease to 76 kg (-13.6%), which would represent the lightest aircraft, giving a good possible solution if a compromise in size could be made.

Table 4.12: Perpetual flight aircraft characteristics.

Parameter	Value	Unit
Wing airfoil	WE3.55-9.3	m
Tail airfoil	E193 inverted	m
Wing span	17.5	m
Aspect ratio	15.8	m
Distance between aerodynamic center of the wing and tail	5.67	m
Total mass	88.0	kg
Battery mass (ratio of total mass)	43.0 (49)	kg (%)
Structure mass (ratio of total mass)	23.5 (27)	kg (%)
Tail angle with horizontal plane	45	degrees
Tail span	3.44	m
Tail chord	0.48	m
Peak power during winter solstice	1955	W
Peak power during summer solstice	3260	W
Number of MPPT	5	

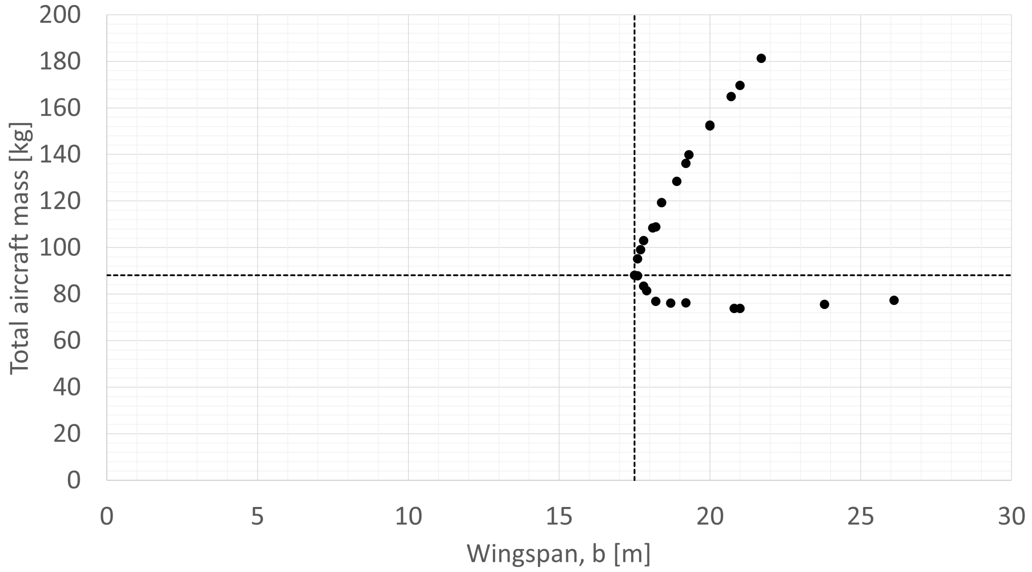

Figure 4.46: Total aircraft mass of several perpetual flight capable aircraft in function of wingspan.

The expected energy balance for this aircraft on the winter solstice is shown in Figure 4.47, where it is possible to see the energy balance from takeoff to mid-night (blue dashed line), and for the following 24 hours (orange line). For the first day it is possible to see the takeoff spike similar to the prototype aircraft, and it is also possible to see that the majority of the Sun energy is not being used, this is due to the fact that the aircraft should take off with full batteries, hence a complete day to recharge them is not necessary. It is also possible to verify that this aircraft is viable since not only the battery never runs out of energy, but also the energy inside the battery on the first day is the same as the energy inside the battery at the end of the following 24 hours. The peak power sent to the battery is around 1850 W.

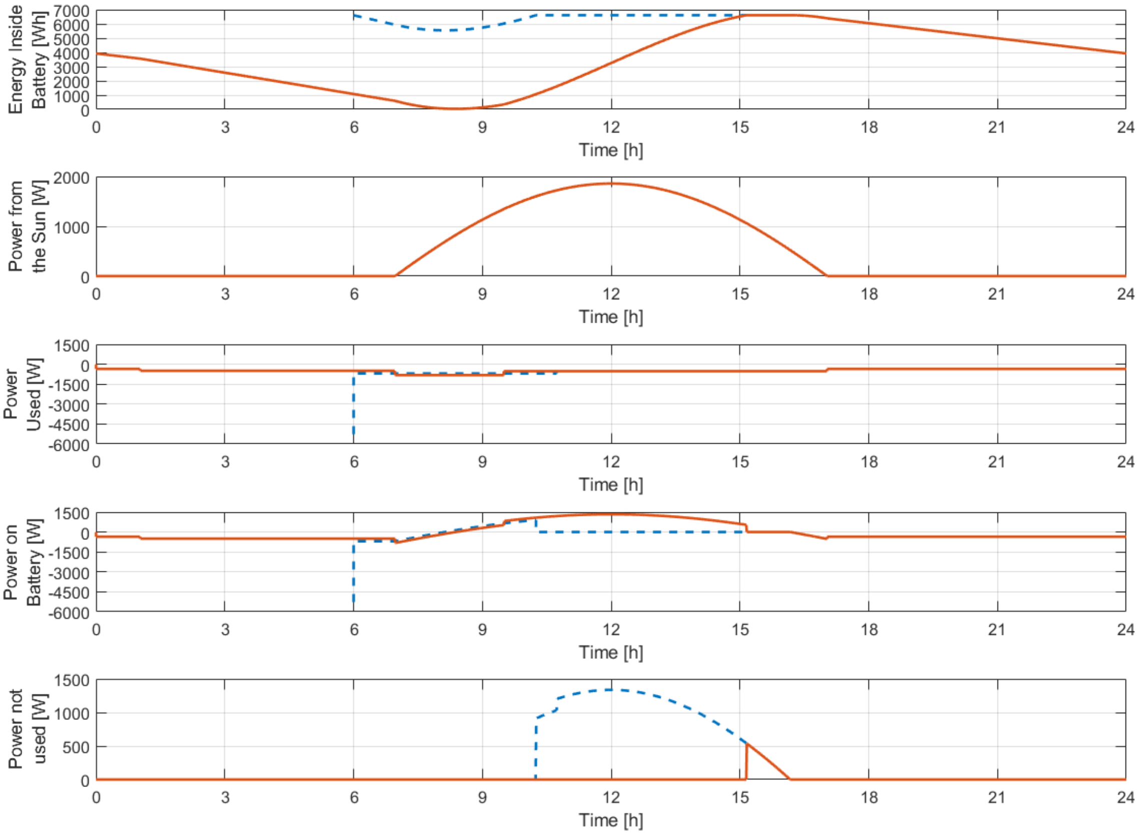

Figure 4.47: Energy and power graphs for the perpetual aircraft at winter solstice.

It is important to note that these values are only theoretical since the parameters used should be changed according to the conclusions from the building and testing of the prototype aircraft, which may change critical design parameters or components. It is also important to verify the validity of the airframe mass model for such different aircraft dimensions.

Chapter 5

Conclusions

In this thesis, the methodology to design a solar UAV is presented. The conceptual and preliminary design of a prototype solar UAV for a fixed mission where the requirements are known, and the detailed design of the wing is also presented. In the end, the preliminary design of a full-size aircraft to perform the mission is shown. The mission of this aircraft is based on the monitoring of wildlife animals at 30° N latitude region any day of the year with a payload of 0.4 kg, composed by an optical and a thermal camera with a peak power of 27 W.

In general, the design process to design a solar UAV is very complex and multidisciplinary matter. One of the hardest parts is the development of the airframe mass model. In the conceptual design, the airframe mass model used is the same as in Noth work. This model is simple, but it has a very small range of validity. Next, in the preliminary design a new mass model is used. In this new model all parts of the structure are taken into account, but since only estimated values were used, the validity range is somewhat unknown, despite having a bigger interval of validity than the previous model. This new mass model becomes more accurate as it is being updated throughout the project.

Another hard part of the structure design is to select not only the right materials but also the right geometries, for example for the ribs, where first a carbon fiber sandwich composite was used, but it proved to be too hard to manufacture. To solve this, balsa wood ribs were used. To test such elements, real structural tests were made in order to validate the parts. In the end, a section of a panel was built to validate the structure concept. In this section several problems were observed, from the axial pin connector, where an extra plywood sheet had to be added locally to increase the wall thickness around the screw; the servo mounting mechanism that had to be redesigned to better fit the screws and the threaded inserts; the trailing edge of the wing panel where the control rod from the servo passes needed a larger hole, and an extra two smaller ribs were added for support; the thickness of the balsa sheet from the leading edge of the aileron that needed to be increased to 2 mm in order to prevent unwanted curvature on the skin, to be supported by the spar, and to allow the hinges to be flushed with the skin ; the control horn that was cut in half to ease the mounting and allow for better movement of the aileron; and finally the ribs that needed to be moved to the middle of the solar cells in order to better fit them to the wing, due to the uncertainty of the thickness in the soldered spots on the solar cells.

As for future work, despite the detailed design of the wing being done, it is still missing the detailed design of the fuselage, tail boom and tail, where the tail should have a similar construction concept as the wing, but without the solar cells. Next, the prototype should be built and tested in order to understand the problems and difficulties one may find in the make of a full-size aircraft. Following this step, the data of the preliminary design should be adjusted according to the conclusions taken from the prototypes, in order to have a better sizing for the full-scale aircraft. For future projects, it would be nice to make a study to increase the precision of the airframe mass model. This study should at least include structural tests with built structural parts.

Bibliography

[1] D. P. Raymer *et al.*, "Aircraft design: a conceptual approach," *Published by American Institute of Aeronautics and Astronautics Inc*, pp. 515–552, 1992. 2, 16, 17, 18, 47

[2] R. Boucher, "History of solar flight," in *20th joint propulsion conference*, 1984, p. 1429. 2, 3, 4

[3] U.S. Department of Energy. (2021) History of solar. [Online]. Available: http://www.eere.energy.gov/solar/pdfs/solar_timeline.pdf 3

[4] A. Noth, "Design of solar powered airplanes for continous flight," Ph.D. thesis, ETH Zurich, 2008. 3, 4, 5, 6, 12, 13, 20, 37

[5] FAI. (2021) The World Air Sports Federation. [Online]. Available: http://www.fai.org 3

[6] D. Howe, "The Design of the Aeroplane," *The Aeronautical Journal*, vol. 106, no. 1062, pp. 459–459, 2002. 4

[7] Solar Flight. (2021) Sunseeker from Eric Raymond. [Online]. Available: http://www.solar-flight.com/ 4

[8] Airbus. (2021) Airbus Zephyr Solar High Altitude Pseudo-Satellite flies for longer than any other aircraft during its successful maiden flight. [Online]. Available: https://www.airbus.com/newsroom/press-releases/en/2018/08/Airbus-Zephyr-Solar-High-Altitude-Pseudo-Satellite-flies-for-longer-than-any-other-aircraft.html 4, 5

[9] Solar Impulse Fundation. (2021) Solar Impulse, "Around the World In a Solar Airplane". [Online]. Available: https://aroundtheworld.solarimpulse.com/our-story/major-steps?utm_source=site&utm_medium=thumbnail&utm_content=story&utm_campaign=major-steps#.VAnJoMJdVfY 4

[10] G. Romeu, G. Frulla, E. Cestino, and G. Corsino, "HELIPAT: design, aerodynamic, structural analysis of long-endurance solar-powered stratospheric platform," vol. 41, no. 6, pp. 1505–1520, 2004. 5

[11] T. Tozer, D. Grace, J. Thompson, and P. Baynham, "UAVs and HAPs-potential convergence for military communications," in *IEEE Colloquium on Military Satellite Communications (Ref. No. 2000/024).* IET, 2000, pp. 10–1. 5

[12] NASA. (2021) NASA Armstrong Fact Sheet: Pathfinder Solar-Powered Aircraft. [Online]. Available: https://www.nasa.gov/centers/armstrong/news/FactSheets/FS-034-DFRC.html#.VAmILcJdVfY 5

[13] ——. (2021) NASA Dryden Past Projects: Helios Prototype Solar-Powered Aircraft. [Online]. Available: https://www.nasa.gov/centers/dryden/history/pastprojects/Helios/#.VAmNG8JdVfY 5

[14] V. Isaienko, V. Kharchenko, M. Matiychyk, and I. Lukmanova, "Analysis of layout and justification of design parameters of a demonstration aircraft based on solar cells," in *E3S Web of Conferences*, vol. 164. EDP Sciences, 2020, p. 13007. 5

[15] Airbus. (2021) Zephyr S. [Online]. Available: http://www.airbus.com/defense/uav/zephyr.html/ 5

[16] UAVOS. (2021) ApusDuo. [Online]. Available: http://www.uavos.com/products/fixed-wing.uavos/apusduo-atmospheric-satellite 5

[17] P. Oettershagen, A. Melzer, T. Mantel, K. Rudin, T. Stastny, B. Wawrzacz, T. Hinzmann, S. Leutenegger, K. Alexis, and R. Siegwart, "Design of small hand-launched solar-powered UAVs: From concept study to a multi-day world endurance record flight," *Journal of Field Robotics*, vol. 34, no. 7, pp. 1352–1377, 2017. 5

[18] R. Boucher, "Project Sunrise-A Flight Demonstration of Astro Flight Model 7404 Solar Powered Remotely Piloted Vehicle," in *15th Joint Propulsion Conference, AIAA-79-1264, Las Vegas, Nevada*, 1976. 6

[19] J. Gedeon, "Some thoughts on the feasibility of a solar-powered plane," *Technical Soaring*, vol. 6, no. 1, pp. 11–18, 1980. 6

[20] E. Schoberl, "Solar-powered aircraft desing," *Technical Soaring*, vol. 15, no. 2, pp. 38–47, 1989. 6

[21] E. Schoeberl, "Possibilities and Requirements for Long Endurance High Flying Solar Powered Platforms," *Technical Soaring*, vol. 23, no. 3, pp. 66–70, 1999. 6

[22] A. J. Colozza, D. A. Scheiman, and D. J. Brinker, “GaAs/Ge Solar Powered Aircraft,” *SAE Transactions*, vol. 108, pp. 49–54, 1999. 6

[23] F. Irving and D. Morgan, “The feasibility of an aircraft propelled by solar energy,” in *2nd International Symposium on the Technology and Science of Low Speed and Motorless Flight*, 1974, p. 1042. 6

[24] M. Bailey, *High altitude solar power platform.* National Aeronautics and Space Administration, George C. Marshall Space, 1992, vol. 103578. 6

[25] D. W. Hall and S. A. Hall, “Structural sizing of a solar powered aircraft,” NASA, Tech. Rep. 172313, 1984. 6

[26] S. A. Brandt and F. T. Gilliam, “Design analysis methodology for solar-powered aircraft,” *Journal of Aircraft*, vol. 32, no. 4, pp. 703–709, 1995. 6

[27] A. Weider, H. Levy, I. Regev, L. Ankri, T. Goldenberg, Y. Ehrlich, A. Vladimirsky, Z. Yosef, and M. Cohen, “Sunsailor: solar powered UAV,” *Technion IIT, Haifa, Israel*, 2006. 6

[28] J. C. C. Sousa, “Solar System for a Long Endurance Electric UAV,” Master’s thesis, Universidade da Beira Interior, 2015. 6, 34, 62

[29] Global Monitoring Laboratory. (2021) Solar Calculation Details. [Online]. Available: https://gml.noaa.gov/grad/solcalc/NOAA_Solar_Calculations_day.xls 14

[30] Pedro Gamboa. (2021) UBI - Aircraft Design - Escolha do Perfil e da Geometria. [Online]. Available: https://webx.ubi.pt/~pgamboa/pessoal/10403/apontamentos/capitulo05.pdf 16

[31] E.-S. Aziz, C. Chassapis, S. Esche, S. Dai, S. Xu, and R. Jia, “Online wind tunnel laboratory,” in *2008 Annual Conference & Exposition*, 2008, pp. 13–949. 16

[32] RaspberryPi. (2021) RaspberryPi HQ camera. [Online]. Available: https://www.raspberrypi.org/products/raspberry-pi-high-quality-camera/ 33

[33] UCTRONICS. (2021) Arducam 35 mm lens. [Online]. Available: https://www.uctronics.com/arducam-35mm-8-degree-1/1.7-m12-lens-with-lens-adapter-for-high-quality-camera.html 33

[34] FLIR. (2021) FLIR Boson camera with lens. [Online]. Available: https://www.flir.com/products/boson/?model=20640A012 33

[35] RaspberryPi. (2021) RaspberryPi 4. [Online]. Available: https://www.raspberrypi.org/products/raspberry-pi-4-model-b/ 33

[36] J. Gundlach, *Designing unmanned aircraft systems: a comprehensive approach.* American Institute of Aeronautics and Astronautics, 2012. 34

[37] R. Santos, P. Neto, M. Ribeiro, B. Penouço, and F. C. Branco, "Projeto de um UAV Solar para Monitorização de Gado - Relatório," 2020, Universidade da Beira Interior - Projeto de Aeronaves. 36

[38] TOPMODEL. (2021) 20 in x 10 in propeller. [Online]. Available: https://www.topmodel.fr/en/product_detail.php?id=20104&templ=1 44

[39] Hacker. (2021) Hacker A50-16L V4 motor. [Online]. Available: https://www.hacker-motor-shop.com/Brushless-Motors/Hacker-Outrunner/Hacker-A50/A50-14pol/A50-16-L-V4-kv265.htm?shop=hacker_e&a=article&ProdNr=15726842&p=6681 44

[40] ——. (2021) Mezon Pro 85 electronic speed controller. [Online]. Available: https://www.hacker-motor-shop.com/Speed-controller-and-accessories/Master-Mezon-Mezon-Pro/MEZON-Pro-Opto/Mezon-PRO-85-opto.htm?shop=hacker_e&SessionId=&a=article&ProdNr=11009085&p=11112 44

[41] MaxAmps. (2021) MaxAmp 6S 11Ah LiPo battery pack. [Online]. Available: https://www.maxamps.com/lipo-11000-6s-22-2v-uav-battery-pack 44

[42] Genasun. (2021) Genasun GVB-8 maximum power point tracker. [Online]. Available: https://genasun.eu/products/genasun-gv-boost-8-lithium-56-8-volt-mppt 44

[43] FullBattery. (2021) Sunpower C60 solar cells. [Online]. Available: https://fullbattery.com/products/sunpower-c60-solar-cell 44

[44] FPVPro. (2021) Dragonlink setup. [Online]. Available: http://www.fpvpro.com/dragon-link-v3-advanced-complete-system 45

[45] MYBOT shop. (2021) Pixhawk 4. [Online]. Available: https://www.mybotshop.de/Pixhawk-PX4-Drone-UAV_1 45

[46] HobbyKing. (2021) Corona CS-939MG servo. [Online]. Available: https://hobbyking.com/en_us/corona-939mg-metal-gear-servo-2-5kg-0-14sec-12-5g.html?___store=en_us 45

[47] F. A. Regulations, “Part 23 Airworthiness Standards: Normal, Utility, Acrobatic and Commuter Category Airplanes,” *Washington DC, US Government Printing Office, Revised January*, 1989. 47

[48] U.S. Military, “Military Specification: Flying Qualities of Piloted Airplanes (MIL-F-8785C),” Nov. 1980. 48

[49] RockWestComposites. (2021) Torayca T700 prepreg properties. [Online]. Available: https://www.rockwestcomposites.com/media/wysiwyg/T700SDataSheet.pdf 52

[50] Pedro Gamboa. (2021) UBI - Estruturas em Materiais Compositos. [Online]. Available: https://webx.ubi.pt/~pgamboa/pessoal/10373/apontamentos/02-EstruturasMateriaisCompositos.pdf 55

[51] Ansys. (2021) Ansys Mechanical. [Online]. Available: https://www.ansys.com/products/structures/ansys-mechanical 56

[52] D. E. K. David W. Green, Jerrold E. Winandy, “Mechanical Properties of Wood,” *Wood handbook Madison, WI: US Department of Agrieculture, Fofest Service, Products Laboratory*, pp. 4–1, 1999. 59

[53] Hacker. (2021) Hacker Q100-7L motor. [Online]. Available: https://www.hacker-motor-shop.com/Brushless-Motors/Hacker-Outrunner/Hacker-Q100/Q100-7L-kv99.htm?shop=hacker_e&a=article&ProdNr=19990738&p=8589 75

[54] JetiModel. (2021) Jeti SPIN Pro 300 opto electronic speed controller. [Online]. Available: https://www.jetimodel.com/katalog/?oldpath=speed-controllers/@produkt/spin-pro-300-opto/ 75

[55] MaxAmps. (2021) MaxAmp 6S 23Ah LiPo battery pack. [Online]. Available: https://www.maxamps.com/lipo-23000-6s-22-2v-battery-pack 75

[56] MG Energy System. (2021) MG Energy System WSC-Si maximum power point tracker. [Online]. Available: https://www.mgenergysystems.eu/products/mg-solar-mppt/ 75

Appendix A

Appendix

A.1 Aircraft list

Here is presented the compilation of solar aircrafts.

Table A.1: Database of solar aircraft.

Nr.	Name	Wingspan [m]	Mean chord [m]	Lenght [m]	Total mass [kg]
1	Sunrise I	9.750	0.860	4.380	12.450
2	Sunrise II	9.750	0.860	4.380	10.210
3	Solaris	2.060	0.200	-	0.610
4	RA	1.370	0.120	0.840	0.190
5	Utopie	2.530	0.200	1.320	0.970
6	Solar-Student	1.960	0.220	1.040	0.930
7	Solar One	20.720	1.170	6.700	104.320
8	Solar-X4	2.500	0.170	1.130	0.850
9	Solar Silberfuchs	4.000	0.250	1.520	2.100
10	Solar Riser	9.140	1.040	2.440	124.700
11	Solar-HB79	2.800	0.240	1.450	1.510
12	Solair I	16.000	1.380	5.400	200.000
13	Gossamer Penguim	21.640	2.630	-	67.700
14	Solar-HB80	2.840	0.230	1.480	1.720
15	Solar Challenger	14.800	1.480	9.220	153.000
16	Solus Solar	3.200	0.290	0.880	2.200
17	Poly	3.240	0.290	0.880	2.480
18	Combi	2.960	0.260	0.850	2.260
19	Solariane	3.080	0.280	1.720	1.800
20	Helios (model)	2.140	0.180	-	1.400
21	Bloch	2.900	0.240	-	1.250
22	Grosholz	3.070	0.190	-	1.850
23	Combi 2	2.950	0.280	1.540	1.700
24	Ikaros	2.500	0.230	-	1.800
25	Bleher	2.000	0.240	-	1.550
26	Romarino	2.000	0.200	-	1.800
27	Sol-e-moi	3.000	17.000	-	2.100
28	Wolf	3.000	0.210	-	1.600
29	WS-Solar	2.500	0.220	-	1.550
30	Ariane Ultra	1.980	0.210	1.140	3.020
31	Solar Voyager	3.200	0.250	-	1.300
32	Mardini	2.400	0.250	-	2.500
33	Solisolar	2.980	0.230	-	1.230
34	PB 26-FL	2.600	0.220	-	2.300
35	Solarbaby	1.700	0.160	-	1.250
36	Bleher	2.000	0.220	-	1.550

Nr.	Name	Wingspan [m]	Mean chord [m]	Lenght [m]	Total mass [kg]
37	Uccello	2.700	0.230	-	11.900
38	Sole Florentino	2.500	0.170	-	1.200
39	Solisolar	2.080	0.180	-	1.500
40	Playboy	2.400	0.190	-	1.350
41	WS12 (then WS16)	2.500	0.160	1.100	0.840
42	Solar Flyer	2.640	0.230	1.480	1.600
43	Blue chip	2.200	0.230	1.250	0.750
44	Solar max	3.480	0.300	1.590	2.540
45	Sollisolar 89-2	2.980	0.230	1.340	1.240
46	Phonix	2.620	0.210	1.290	1.180
47	Sunseeker	-	-	-	-
48	Solar UHU	2.300	0.230	1.200	1.450
49	Blue-Wing	3.340	0.180	1.050	0.750
50	Solar schilti 1	1.740	0.190	1.160	0.700
51	Solar schilti 2	1.990	0.180	1.050	0.820
52	Silzi Solar	2.250	0.210	1.300	1.080
53	Solix	2.370	0.200	1.300	1.050
54	Solar mini Challenger	1.550	0.180	-	0.940
55	Rival-8 Solaris	1.960	0.220	1.130	0.660
56	Pathfinder	26.500	0.400	3.600	252.000
57	MikroSol	1.130	-	-	0.190
58	Solair II	20.000	0.860	6.120	230.000
59	Icare II	25.000	1.030	7.700	360.000
60	Lo 120 Solar	15.460	1.030	-	-
61	Solarflugzeug	18.000	1.500	-	280.000
62	O sole mio	20.000	1.230	-	220.000
63	Solar Solitude	2.700	0.200	-	2.000
64	NanoSol	1.110	-	-	0.160
65	Centurion	61.800	2.400	3.600	862.000
66	Trosollmuffel	2.500	0.250	-	1.140
67	Global Flyer	2.500	0.230	1.200	1.040
68	Pathfinder Plus	36.300	2.400	3.600	315.000
69	Solar Excel	2.100	0.160	1.020	0.720
70	Solitair	5.200	-	-	-
71	PicoSol	0.990	-	-	0.130
72	LFMA	1.900	0.250	-	1.200
73	Helios HP01	75.300	2.480	3.600	930.000
74	Sunrazor (Sunriser)	2.700	0.300	-	1.100
75	Goldcap2	-	-	-	-
76	Solarus	2.300	0.190	-	0.480
77	FlyG	6.000	0.600	2.700	10.000
78	Solar Pleaser	1.040	0.150	1.010	3.250
79	No name	0.140	0.015	0.120	0.002
80	Solar Splinter	4.270	0.350	2.130	4.500
81	Sol-Mite	0.810	0.120	-	0.130
82	Sky-Sailor	3.200	0.240	1.820	3.000
83	Zephyr 6	18.000	1.550	-	30.000
84	Solong	4.750	0.320	-	12.600
85	NanSun	3.200	0.400	2.600	4.100
86	HowieMark	2.430	0.200	-	0.450
87	NunSailor	4.200	0.320	2.200	3.600
88	Aphelion	3.130	0.220	-	-
89	2.765 g Solar MAV	0.140	0.040	0.150	0.003
90	SolFly	0.070	-	-	0.001
91	Micro-mite	0.200	0.050	-	0.010

Nr.	Name	Wingspan [m]	Mean chord [m]	Lenght [m]	Total mass [kg]
92	Sun-Surfer I	0.770	-	0.730	0.120
93	Sun-Surfer II	0.780	0.110	0.740	0.188
94	Sun-Sailor	4.200	3.110	2.200	3.600
95	AtlantikSolar AS-2 UA	5.650	-	-	6.930
96	SUAV: Q hybrid	4.000	-	-	3.364
97	Cranfield University	3.700	-	-	3.000
98	Zephyr 7	22.500	1.900	10.300	53.000
99	LA-252	75.300	2.440	-	115.000
100	EAV-1	2.720	0.320	1.700	-
101	EAV-2	6.930	0.350	3.020	18.000
102	EAV-2H	10.830	0.540	5.000	20.000
103	EAV-3	19.500	1.120	8.800	46.000
104	Apus Duo	15.000	-	-	43.000
105	Zephyr 8/Zephyr S	28.000	-	-	75.000
106	AircraftDesign	30.000	1.780	12.000	111.000
107	AtlantikSolar	5.690	-	-	6.930
108	LEEUAV	4.500	0.330	-	4.900
109	SHAMPO	73.000	2.630	-	924.000

A.2 Detailed mass and position of all components for the prototype aircraft

Here the mass and position of all components of the aircraft is shown. The wing includes not only the structure but also the solar cells and servos, while the tail only includes servos and the structure. The origin of the referential is in the leading edge of the wing and is positive towards the tail of the aircraft.

Table A.2: Mass and position of all components of the prototype aircraft.

	Winter Aircraft		**Summer Aircraft**	
Component	**Mass [kg]**	x_{CG} **[mm]**	**Mass [kg]**	x_{CG} **[mm]**
Propeller	0.100	-0.506	0.100	-0.506
Motor	0.445	-0.454	0.445	-0.454
ESC	0.200	-0.309	0.200	-0.309
Fuselage	0.900	-0.032	0.900	-0.032
Battery pack 1	1.270	-0.211	1.270	-0.211
Battery pack 2	1.270	-0.211	1.270	-0.211
Battery pack 3	1.270	-0.100	1.270	-0.100
Battery pack 4	-	-	1.270	0.012
Battery pack 5	-	-	1.270	0.012
MPPT 1	0.200	-0.181	0.200	-0.181
MPPT 2	0.200	-0.026	0.200	-0.026
MPPT 3	0.200	-0.026	0.200	-0.026
BMS	0.100	-0.201	0.100	-0.201
GPS	0.070	-0.081	0.070	-0.081
Airspeed sensor	0.020	0.005	0.020	0.005
Cables	3.000	0.200	3.000	0.200
Antennas	0.020	0.200	0.020	0.200
RaspberryPi HQ Camera	0.050	0.150	0.050	0.150
FLIR Boson	0.100	0.150	0.100	0.150
RaspberryPi 4	0.050	0.226	0.050	0.226
RaspberryPi Wi-Fi antenna	0.200	0.200	0.200	0.200
Pixhawk power board	0.036	0.226	0.036	0.226
Pixhawk 4	0.180	0.226	0.180	0.226
Dragonlink	0.012	0.226	0.012	0.226
Wing	7.812	0.138	6.849	0.138
Tailboom	0.842	1.312	0.842	1.312
Tail	0.544	2.318	0.544	2.318
Total	19.091	0.162 (0.29c_W)	20.668	0.144 (0.26c_W)

A.3 Components correlations

Here it is possible to see the graphs of the correlations for the 2045 motors, 34 ESC, 12 MPPT and 29 batteries.

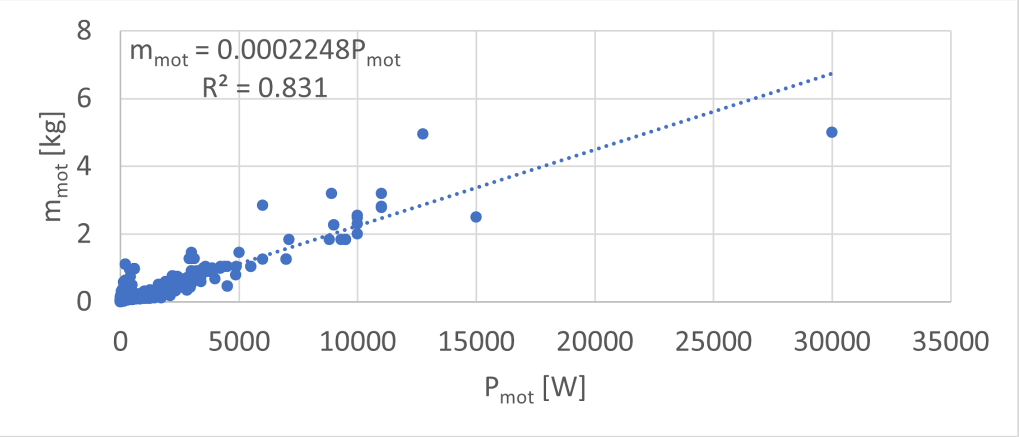

Figure A.1: Correlation between the power and mass of the motors.

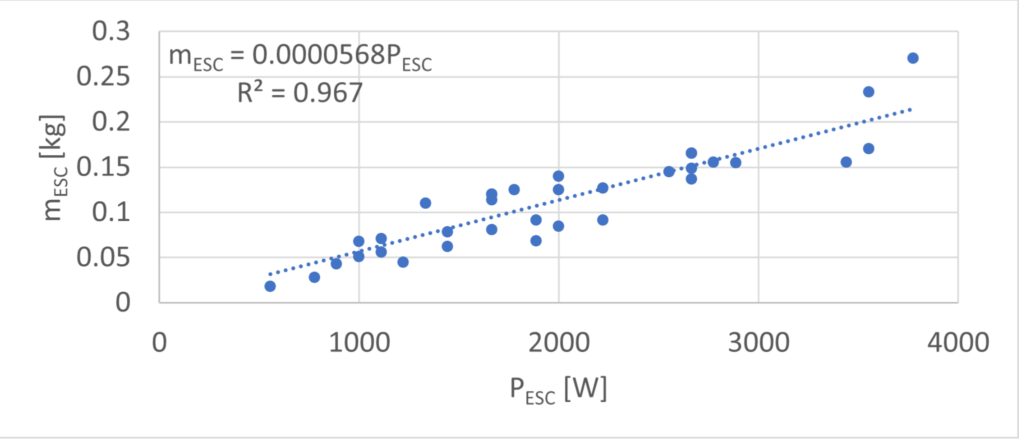

Figure A.2: Correlation between the power and mass of the ESC.

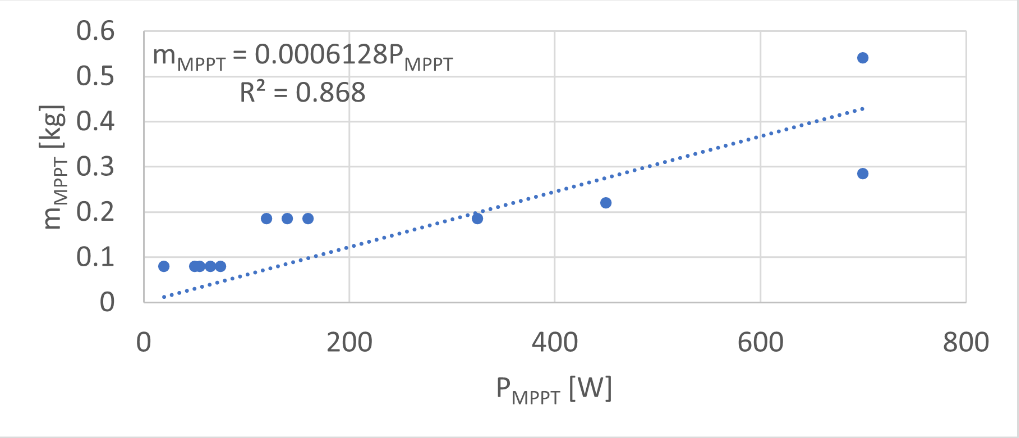

Figure A.3: Correlation between the power and mass of the MPPT.

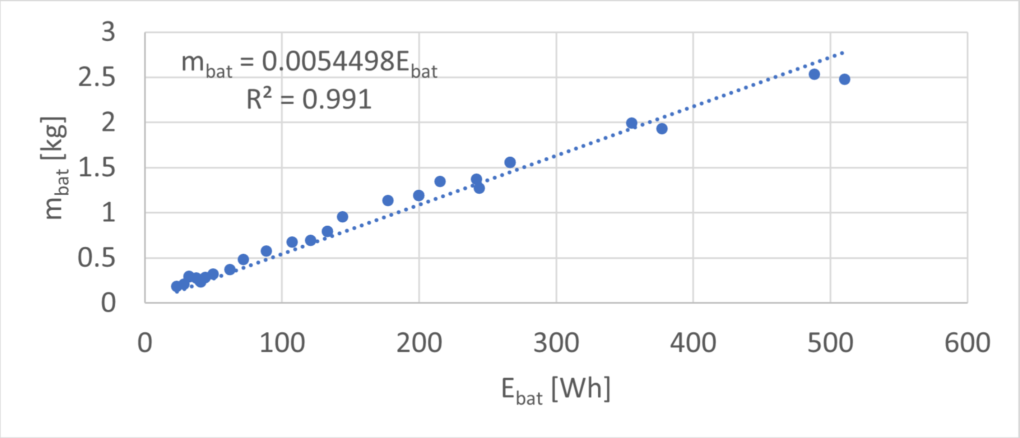

Figure A.4: Correlation between the energy capacity and mass of the batteries.

A.4 Drag polar for the winter and summer prototype aircraft

Here is presented the drag polar for both winter and summer prototype aircraft.

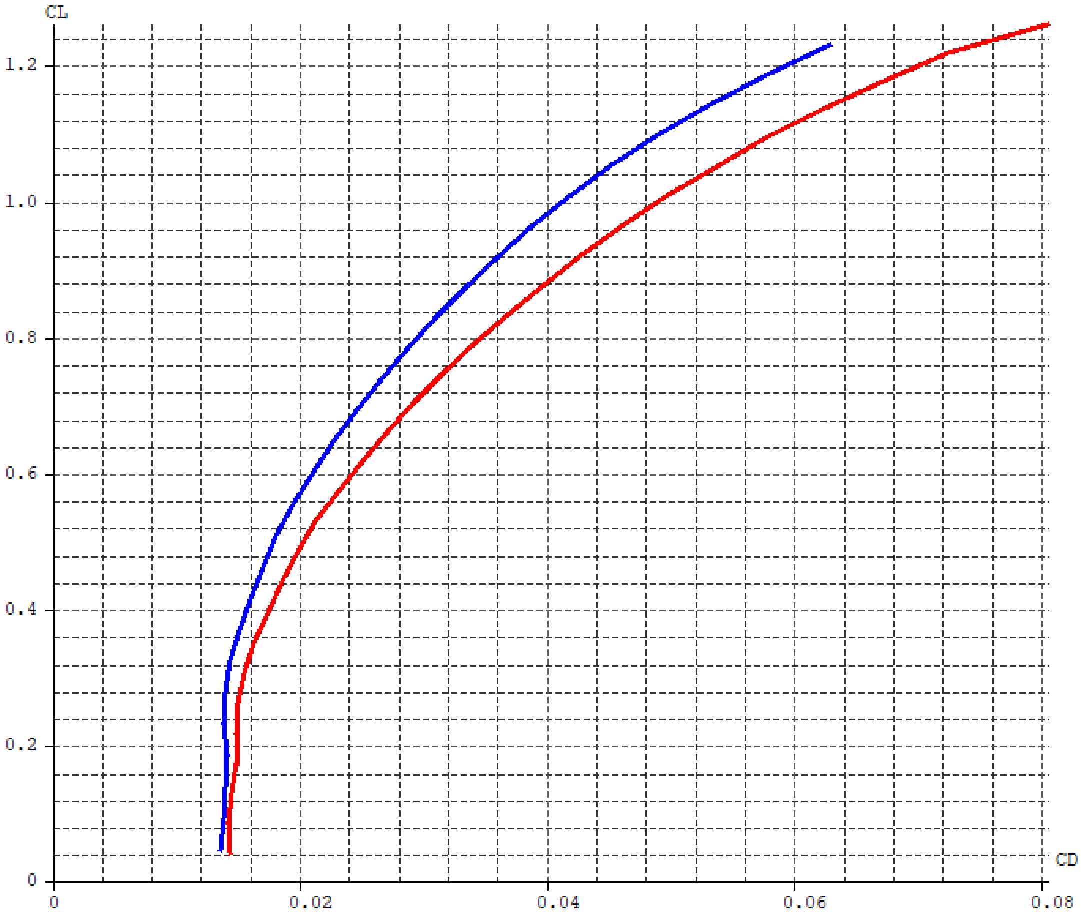

Figure A.5: Drag polar for the winter (blue) and summer (red) aircraft.

A.5 Dynamic stability

Here is presented the dynamic stability analysis graphs for the winter and summer prototype aircraft.

A.5.1 Winter aircraft

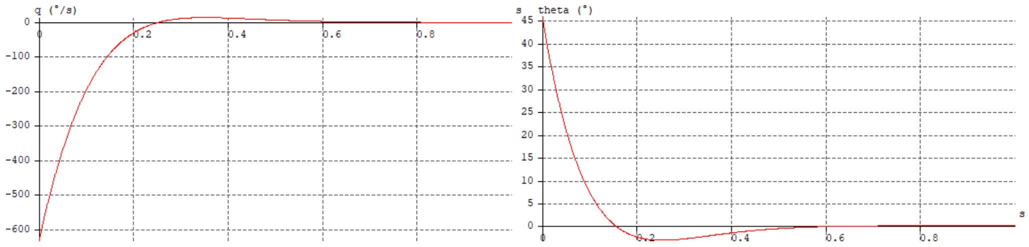

Figure A.6: Pitching response graph for the winter aircraft.

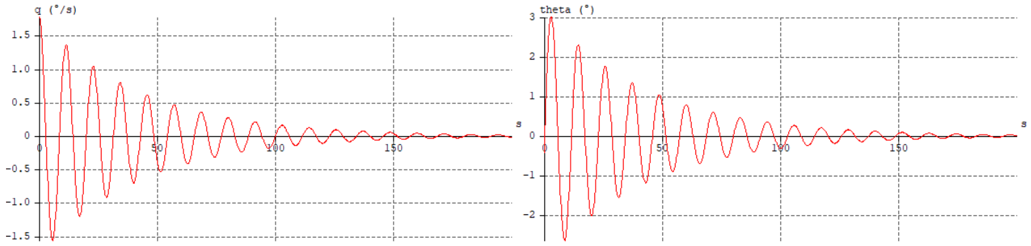

Figure A.7: Phugoid response graph for the winter aircraft.

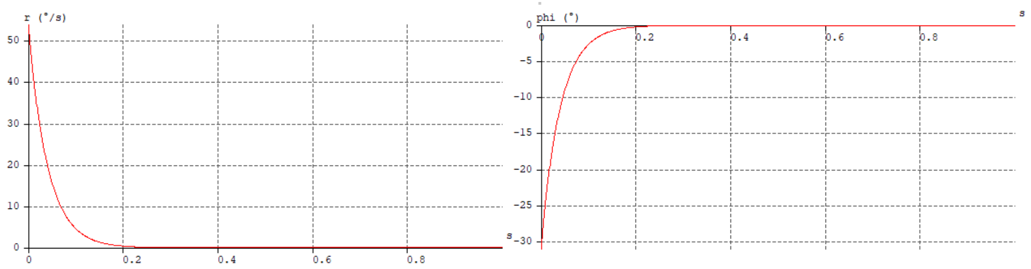

Figure A.8: Roll response graph for the winter aircraft.

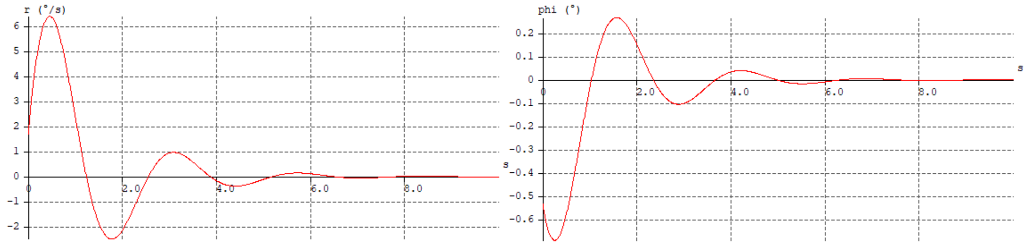

Figure A.9: Dutch-roll response graph for the winter aircraft.

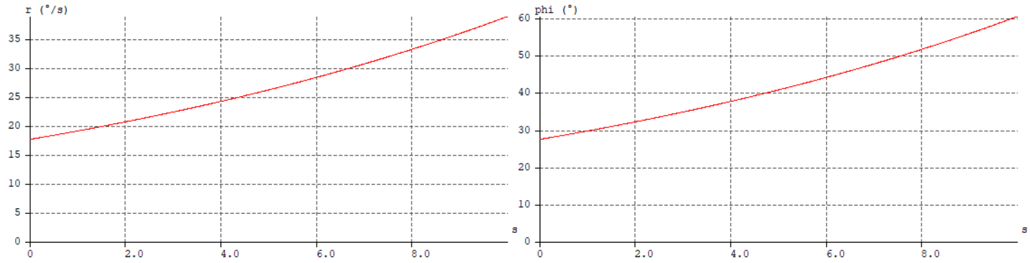

Figure A.10: Spiral response graph for the winter aircraft.

A.5.2 Summer aircraft

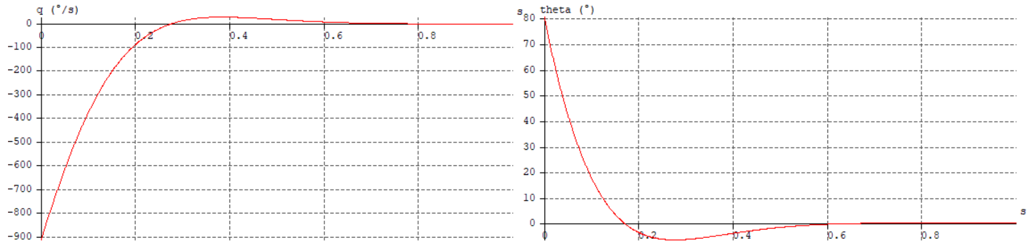

Figure A.11: Pitching response graph for the summer aircraft.

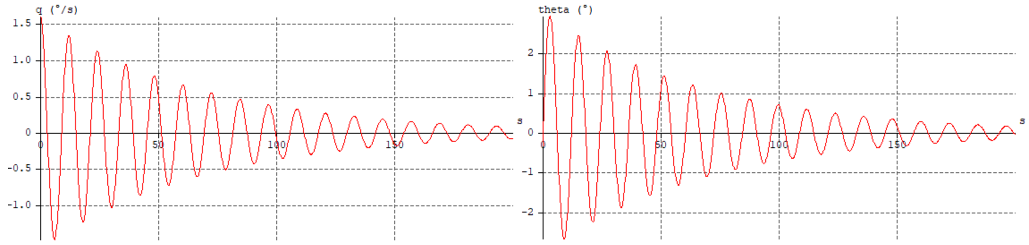

Figure A.12: Phugoid response graph for the summer aircraft.

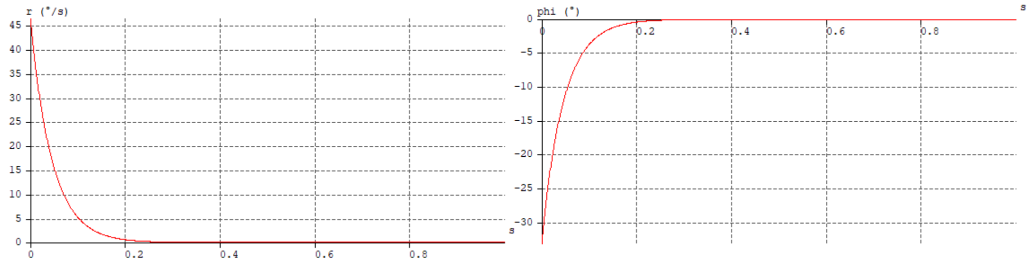

Figure A.13: Roll response graph for the summer aircraft.

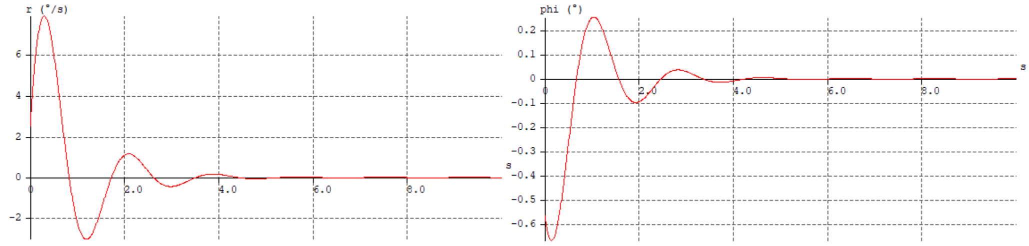

Figure A.14: Dutch-roll response graph for the summer aircraft.

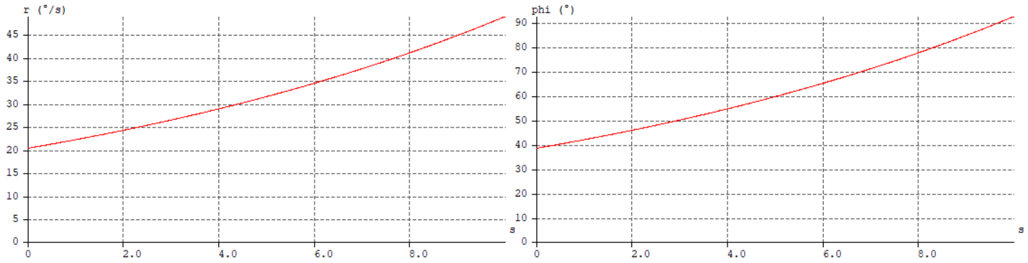

Figure A.15: Spiral response graph for the summer aircraft.

A.6 Detailed drawings of the prototype aircraft

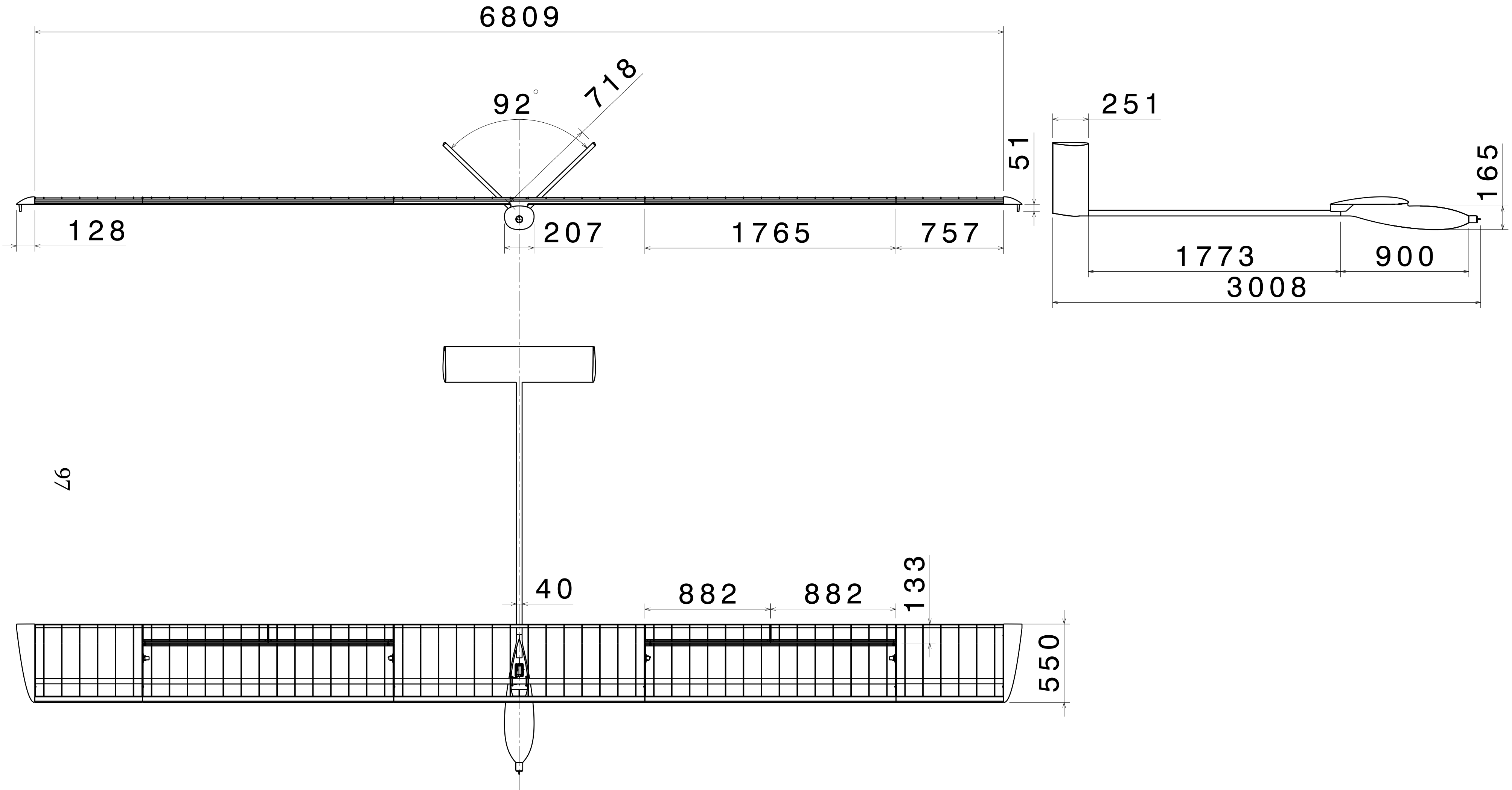

Aircraft Properties	Winter	Summer
Wingspan	6.809 m	5.295 m
Aspect ratio	12.38	9.63
Total mass	19.09 kg	20.02 kg
Lenght	3.008 m	
Propeller size	20 in x 10 in	
Wing Airfoil	WE3.55-9.3	
Tail Airfoil	E193 inverted	
Design latitude	30°N	
Design cruise altitude	3000 m	
Cruise speed	13.3 m/s	14.4 m/s

DESIGNED BY: Rúben Santos
DATE: 23/08/2021
CHECKED BY: XXX
DATE: XXX

Design of a solar UAV for persistent wildlife monitoring

SIZE: A2

Universidade da Beira Interior

SCALE: 1:20
WEIGHT (kg): 19.09
DRAWING NUMBER: Solar UAV
SHEET: 1/1

I	_
H	_
G	_
F	_
E	_
D	_
C	_
B	_
A	_